

Towards clinical speed-of-sound imaging based on pulse-echo ultrasound

Inauguraldissertation
der Philosophisch-naturwissenschaftlichen Fakultät
der Universität Bern

vorgelegt von

Patrick Stähli

von Schwanden bei Brienz

Leiter der Arbeit

Prof. Dr. Martin Frenz

PD Dr. Michael Jaeger

Institut für Angewandte Physik
Universität Bern

Towards clinical speed-of-sound imaging based on pulse-echo ultrasound

Inauguraldissertation
der Philosophisch-naturwissenschaftlichen Fakultät
der Universität Bern

vorgelegt von

Patrick Stähli

von Schwanden bei Brienz

Leiter der Arbeit
Prof. Dr. Martin Frenz
PD Dr. Michael Jaeger

Institut für Angewandte Physik
Universität Bern

Von der Philosophisch-naturwissenschaftlichen Fakultät angenommen.

Bern, 31.07.2020

Der Dekan



Prof. Dr. Zoltán Balogh

Thesis committee members:

- Prof. Dr. Martin Frenz
- PD Dr. Michael Jaeger
- Prof. Dr. Georg Schmitz
- Prof. Dr. Uwe-Jens Wiese

The work described in this thesis was performed at the research group: Biomedizinische Photonik (BP), Institut für Angewandte Physik, Philosophisch-naturwissenschaftliche Fakultät, Universität Bern, Hochschulstrasse 6, 3012 Bern, Schweiz

Under the supervision of:

- Prof. Dr. Martin Frenz
- PD Dr. Michael Jaeger

Contents

1	Introduction	1
2	Improved forward model for quantitative pulse-echo speed-of-sound imaging	19
2.1	Introduction	20
2.2	Theory	23
2.2.1	The old model	24
2.2.2	New model	26
2.3	Materials and Methods	31
2.3.1	Space domain forward and inverse model	31
2.3.2	Data acquisition and beamforming	35
2.3.3	Phase shift tracking	38
2.3.4	SoS reconstruction	38
2.3.5	Phantom design and materials	40
2.4	Results	42
2.4.1	Echo phase shift	42
2.4.2	SoS images	44
2.5	Discussion and Conclusion	48
3	Bayesian approach for a robust speed-of-sound reconstruction using pulse-echo ultrasound	61
3.1	Introduction	62
3.2	Materials and Methods	64
3.2.1	SoS reconstruction based on spatial gradient regularization	65
3.2.2	SoS reconstruction using <i>a priori</i> knowledge	65
3.2.3	Synthetic dataset	68
3.2.4	Phantom design	68
3.2.5	In-vivo data	69
3.2.6	Ultrasound system	69
3.3	Results	70
3.3.1	Simulation study	70
3.3.2	Phantom results	73
3.3.3	In-vivo results	74

3.4	Discussion and Conclusion	76
4	Receive beam steering and clutter reduction for imaging the speed-of-sound inside the carotid artery	85
4.1	Introduction	86
4.2	Materials and Methods	88
4.2.1	Conventional Tx CUTE	88
4.2.2	Full-Rx CUTE	89
4.2.3	Fast-Rx subtraction technique	89
4.2.4	Phantom description	90
4.2.5	Acquisition system	91
4.2.6	US image reconstruction and phase tracking	91
4.2.7	SoS image reconstruction	92
4.3	Results	92
4.3.1	Tx versus full-Rx CUTE	92
4.3.2	Fast-Rx subtraction technique	93
4.4	Discussion and conclusion	95
5	Conclusion and Outlook	101
	Author Contribution Statements	105
	Acknowledgements	106
	Erklärung	106
	Curriculum vitae	108

Chapter 1

Introduction

Medical imaging has its origin in November 1895 with the discovery of X-ray by Conrad Roentgen. He noticed that X-ray were being absorbed more by bone and metal than human flesh [1]. Roentgen used this insight to develop a technique that allows to reveal what is happening inside a patient's body non-invasively. The very first X-ray image in history – and probably the most famous one – is the one that Roentgen took of the left hand of his wife Bertha (see Fig. 1.1). For this milestone, he was honoured with the first Nobel Price in 1901.



Figure 1.1: The very first X-ray image in history. The image was taken by Conrad Roentgen in 1895 and shows the left hand of Roentgen's wife Bertha [2]. The black spot on the fourth finger is caused by the wedding and engagement rings.

X-ray imaging has quickly become essential for diagnostic purposes in medicine [3, 4]. In the following century, science was directed towards more advanced image modalities providing complementary information, such as computed tomography (CT), magnetic resonance imaging (MRI), positron emission tomography (PET) and ultrasound (US). Today, imaging is an integral part of medical practice and allows accurate diagnosis of a large variety of disease types in a non-invasive procedure. Without question, medical imaging is one of the most important advances in the history of medicine [5].

Out of the well-established imaging modalities, US has various distinct advantages. It provides real-time feedback that makes it possible to evaluate rapidly moving structures such as the heart or the moving fetus. Real-time imaging allows further to examine patients that are unable to suspend respiration or cooperate with the radiologist. The portability of modern US systems has become paramount, as it allows point-of-care use [6]. A further advantage of US is that it provides diagnostically useful information without the use of ionizing radiation. In obstetrics for example, this allows multiple sequential examination during pregnancy without causing significant health risk to the mother and fetus [7, 8]. Finally, in the era of medical cost containment, US is an attractive imaging modality since it has a low cost as compared to other techniques, being affordable for the point-of-care level. Conventional handheld US is based on insonifying the tissue with US pulses in the frequency range of about 1 to 15 MHz [9]. While propagating through the tissue, the US is (back) scattered due to reflections at microscopic spatial fluctuations of density and compressibility. These reflected echoes are typically detected using an array of piezoelectric transducer elements (array probe). The localization of the position where the echo was generated is based on the time-of-arrival of the echo at the array probe and on the relative timing of the detected signals at the different array elements. After performing various image processing steps, the tissue's internal "echo-generators" are then most commonly displayed in a spatially resolved way by encoding the intensity of a detected echo in brightness (B-mode). US is typically weakly scattered inside the tissue, resulting in minor distortions of the propagating waves. Therefore, coherent focusing is possible in both transmission and detection. Consequently, the lateral resolution is determined by the focal length, the transducer aperture and center frequency. The axial resolution of US is primarily determined by the probes frequency bandwidth. A typical axial and lateral resolution of US images lies in the range of the acoustic wavelength (≈ 0.3 mm for a 5 MHz center frequency probe assuming a uniform SoS distribution inside the tissue of 1540 ms^{-1}). An important application of medical US is the diagnosis of diseases in soft organs [10], as e.g in the field of cardiology [11], the detection of cancer [12, 13], emergency medicine [14], obstetric [15] and the diagnosis of various liver diseases [16–18], just to name a few. US, however, has proven its value not only in diagnostic applications, but also in the filed of US-guided interventions such as biopsies [19, 20], the observation of needle injection for local anaesthesia [21], tracking the tumor size for cancer therapy [22] and the real-time display of the anatomy to aid in a computer-assisted surgery [23]. Furthermore, US is also used for therapeutic purposes [24]. High intensity focused ultrasound (HIFU) is for example being studied for the treatment of prostate cancer [25].

Besides the many advantages of classical US, a main drawback is its limitation to the gray scale B-mode contrast. The natural variability of the echogenicity between

patients in comparison to the influence of various disease types on the echogenicity leads to B-mode US images that often suffer from non-specific contrast and low sensitivity for certain disease types [26–29]. Further, the interpretation of the B-mode image is not quantitative and the outcome very much depends on the operators experience [30, 31]. For example for diagnosing steatosis, this results in a low sensitivity and specificity for early stages in disease progression [32–34]. A meta-analysis [35] has concluded that the sensitivity and specificity of US for the diagnosis of hepatic steatosis are 73.3% and 84.4% for mild ($<10\%$) steatosis. For a more advanced disease progression ($>50\%$ steatosis), a sensitivity of 91.1% and specificity of 91.9% was concluded. This increase in the sensitivity and specificity can be explained by the increased influence of the disease on the echogenicity, in comparison to the natural variability of the echogenicity between patients.

To circumvent the sometimes low diagnostic accuracy of B-mode US, it can in principle be complemented with other imaging modalities such as CT or MRI to provide complementary diagnostic information. This has, however, the disadvantage of generating additional health care cost.

To overcome this shortcoming, research in recent decades was directed towards novel US based modalities implemented in a single multi-modal system. In this way, B-mode images can be complemented with additional functional and structural information while still maintaining the advantages of US systems. US Doppler flow imaging is an already state-of-the-art US based imaging modality that allows to assess the relative velocity of structures (usually blood) and their direction (towards or away from the probe). The velocity information can be displayed in various ways, e.g. as color flow image where a spatially resolved color-coded velocity map is overlaid onto the B-mode image. Today, Doppler flow imaging is well established and has many medical applications. Among them are Doppler echocardiography to examine blood flow inside the heart [36], the examination of the kidney to evaluate perfusion [37] and the examination of blood vessels to help determining vascular stenosis (narrowing) or occlusion (complete closure).

US imaging has, however, the potential to image much more than echogenicity and blood flow. Indeed, a family of approaches based on the quantification of the tissues mechanical properties using US have been proposed. Biomechanical properties have the advantages that they are altered by pathological processes and therefore can provide diagnostic information. The manual palpation for investigating the tissues elasticity as a diagnostic marker has been used for centuries, and is still commonly used for screening e.g. breast and prostate tumors. US elastographic techniques image the elasticity of the tissue while being distorted. Strain imaging is one of the earliest developed US based elastography techniques. It images the tissue's strain in a spatial resolved way when palpating the skin using the ultrasound probe [38]. This allows a more accurate diagnosis of disease types and margins compared to

classical B-mode US [39–41]. A limitation of strain imaging is, however, that organs that are not close to the surface are difficult to compress [42]. Contrary to strain imaging, in shear-wave elastography, the tissue is distorted "from inside" by using high intensity focused ultrasound pulses. The propagation of the shear-wave that is thereby generated is tracked using time-resolved phase tracking of the US echoes and gives a quantitative measurement of the spatial distribution of the elastic modulus [43–45].

Whereas in shear-wave elastography, longitudinal waves are used to track the propagation speed of shear-waves, another approach is to determine directly the velocity of the longitudinal waves themselves, i.e. the speed-of-sound (SoS) of US. Similar to the shear-wave speed, also the SoS of US is related to biomechanical properties of the imaged tissue. Therefore, SoS imaging is a further promising modality to provide complementary information about the tissues physical properties.

The state-of-the-art methods for imaging local SoS distribution (and the US attenuation coefficient) are those based on ultrasonic computed tomography (UCT) [46, 47]. UCT is a through-transmission technique that is conceptually similar to CT. The sample is suspended inside a water-filled bowl, surrounded by transducer elements. These elements can be arranged in an annular or spherical way, or by circularly scanning array probes. US is transmitted from various different angles by sequentially activating transducer elements. The US propagated through the sample is then recorded on the opposite side as a function of propagation path. The main advantage of UCT is that transmission data are available from a large variety of angles. This allows an accurate reconstruction of the spatial distribution of SoS and US attenuation. Breast-UCT has demonstrated impressively the diagnostic potential of SoS imaging in the example of breast cancer imaging [48–52]. However, the main disadvantage of UCT lies in it's bulky and stand-alone set-up and the clinical limitation to acoustically transparent parts of the body, i.e. mainly the female breast.

To fully unravel the potential of US based SoS imaging, it is desirable to implement it in conventional US devices that operate based on pulse-echo signals. This would allow to image the SoS not only in the female breast but on every part of the human body that is routinely examined with classical US. The main difficulty of SoS imaging in reflection mode is, in comparison to UCT, a reduction in data availability due to the limited set of transmission angles, and due to the limited frequency bandwidth.

Despite this difficulty, several authors have reported SoS reconstruction techniques that operate in reflection mode. A family of methods has been proposed that estimate a single average SoS value between the transducer and a focal depth [53–56]. One promising method that has already proven its diagnostic potential in a clinical pilot study of diagnosing liver steatosis is [57, 58]. This method relies on quantify-

ing the blurring of echoes caused by aberrations via a quality measure of the image resolution. The SoS is then deduced by iteratively adapting the SoS with the goal to increase image quality. This method is, however, only suitable for estimating the SoS in organs with a uniformly distributed SoS such as the liver.

As opposed to measuring an average SoS value, several methods have been investigated that are able to image the spatial distribution of SoS. In principle, this could be done in a way similar to diffraction tomography, by relating the spatial distribution of SoS to the detected signals via e.g. the 1st order Born approximation. Such an approach, however, would require the availability of low frequencies in the detected echoes [59, 60], e.g. down to ≈ 75 kHz corresponding to a spatial scale of SoS variations of ≈ 5 mm. Unfortunately, in practice, the band-limited US probes do not allow for the detection of such low temporal frequencies. Consequently, low spatial variations of SoS across different tissues that lead to echoes with correspondingly low temporal frequencies cannot be reconstructed. A reconstruction of SoS beyond the 1st Born approximation is in principle feasible when taking into account a multiple-scattering process in a non-linear full-wave inversion. Promising theoretical results were obtained with an approach taking into account multiple-scattering process via non-linear full-wave inversion [61]. However, an initial approximation of the acoustic tissue properties had to be made based on frequencies (0.1 MHz) far below the lower band-limit of US probes. Further, due to the algorithm's complexity and the large number of iterations required, real-time imaging is not feasible.

To circumvent these issues, several alternative approaches for measuring the spatial distribution of SoS based on the acquisition of multiple pulse-echo data-sets have been reported. Early attempts to measure the SoS distribution are based on a beam tracking technique [62, 63]. Two separated transducers (one for transmit, one for receive) or subapertures of the same array probe are arranged so that they intersect in a limited volume. The time of flight of an US pulse from the transmitting transducer to the intersection volume and back to the receiving transducer is then calculated. In combination with the total path length that is assumed from geometric consideration, the SoS in the tissue can be estimated. This approach, however, results in a very coarse spatial resolution in the range of about 10 mm for detecting an inclusion with 1% SoS contrast [64]. Another method is based on the co-registration of two isolated bright point reflectors [65]. By emitting a spherical wave, the SoS between these point reflectors is estimated by calculating the time-of-flight. Although SoS estimates with errors less than 1% are achieved in simulation and phantoms, this method relies on the presence of point reflectors such as wire targets, which are typically not available in real tissue textures. Another approach relates the average SoS between the transducer and focus to the local SoS values along the propagation path via a forward model [66]. Thereby, the average SoS is computed from arrival-time profiles using the method proposed in [53]. The spatial

distribution of SoS is then reconstructed by solving the forward problem using the method of gradient descent. This technique was verified only in phantoms without lateral SoS variations, where it provided an axial resolution of about 7 mm.

In our group, we developed a technique that allows real time imaging of the SoS with a high spatial and contrast resolution called computed ultrasound tomography in reflection mode (CUTE). As mentioned, reflection-mode SoS reconstruction based on the 1st Born approximation is not feasible due to the band-limited US probes. Therefore, in CUTE, the US wave propagation is thought of as a 3rd order scattering process: The aberration of the wave front when propagating from the transducer into the tissue is considered as the 1st (forward) scattering process. The echo generation, i.e. backscattering of the wave front, is the 2nd scattering process. The aberration of the backscattered wave front when propagating back to the transducer is finally the 3rd (forward) scattering process. To circumvent a time-consuming iterative full-wave inversion, CUTE is based on a two-step process: In the first step, only the 2nd scattering process is taken into account. Based on the Born approximation and assuming a uniform SoS \hat{c} , a set of conventional radio-frequency (RF) mode echo US images are reconstructed using various different transmit/receive steering settings. For the second step, the influence of the 1st and 3rd scattering process are modelled as a local echo-phase shift $\Delta\Theta$ between RF-mode images with different steering settings. By making a linear approximation for the influence of the 1st and 3rd scattering order, i.e. the straight ray approximation, the local distribution of SoS c can be related to the local distribution of echo-phase shift $\Delta\Theta$:

$$\Delta\Theta = \mathbf{M}(c - \hat{c}) \quad (1.1)$$

In the earliest implementation of this idea [67], the forward model \mathbf{M} was based on two main key assumptions:

1. The echo phase shift is entirely determined by the changing aberration delay along the changing Tx propagation directions
2. The echo phase shift is proportional to the difference in aberration delay along different round-trip paths.

In view of computational efficiency, this forward model was formulated in the frequency-domain (FD). In a proof-of-principle study [67], it has been demonstrated that CUTE can provide a contrast resolution in the range of about 10 ms^{-1} and a spatial resolution in the millimetre range. A volunteer study then confirmed that CUTE is able to differentiate different tissue types in-vivo, imaging the liver and neck of a healthy volunteer [68].

The FD approach, however, turned out to have a substantial drawback: it implicitly assumes the availability of phase shift data everywhere in the imaging plane.

Depending on the Tx angle, the Tx wave front, however, insonifies only part of the imaging plane, leaving areas of missing echoes toward the edge of the image. These regions of missing data consequently lead to SoS artifacts in the reconstructed SoS image. For that reason, the FD formulation can only provide quantitative results when examining a spatially confined SoS contrast region located within the 'view' of all Tx angles.

To solve this limited data problem, we proposed a space-domain (SD) approach [69], where the angle-dependent transmission shadows can be modelled explicitly as part of the forward model. This led to SoS images that suffer less from artifacts compared to the previously used FD approach. The advantage of the SD approach has been verified in a simulation study [70] and a clinical pilot study [71]. We found, however, in an extensive phantom study with a variety of sample geometries inconsistent results: First, the reconstructed SoS values strongly depended on the *a priori* SoS that was assumed for beamforming. Secondly, strong artifacts in the SoS images were observed when imaging samples with lateral SoS variations.

A comparison of the measured phase shift and the phase shift predicted by the forward model (based on the known SoS distribution) revealed a mismatch between the two. This mismatch strongly depended on the sample's geometry: In scenarios with cylindrical inclusions, the phase shift magnitude was roughly correctly predicted by the forward model, although the profile shape was wrongly predicted. In scenarios with layered structures, the correct profile shape was predicted but with a phase shift magnitude that was underestimated by about a factor of two. As a consequence of this mismatch, inconsistent SoS reconstructions were obtained, depending on the sample geometry and the initial SoS \hat{c} .

Detailed simulations of the data at the various steps involved in the signal processing pipeline revealed that the two key assumptions mentioned above do not hold and had to be modified as follows:

1. Even if the Rx aperture is held constant while changing the Tx angle, the echo phase shift contains the influence of a virtually changing Tx angle. To avoid ambiguities, we propose to switch from a pure Tx-steering approach to simultaneously steering both, the Tx and Rx- angle, around a variety of common mid-angles, in an approach similar to the common-mid-point gather that has been used in seismic imaging as well as US.
2. The *a priori* unknown SoS distribution leads to an offset of the reconstructed position of echoes. This offset not only depends on the aberration delay, but independently also on the values of the steering angles. As a result, the initially assumed simple proportionality between the aberration delay and phase shift is no longer valid.

These two new key assumptions then lead to the formulation of a new, more accurate forward model.

A big part of this thesis was to optimize the implementation and parameters of CUTE to achieve the best possible results with the two models. This allowed a rigorous comparison and evaluation of the two models in an extensive phantom study containing phantoms with various different geometries and SoS contrasts. These phantoms were designed in view of two specific target clinical applications: layered phantoms that mimic the abdominal wall and liver (hepatic imaging) and phantoms mimicking a circular lesion inside a layered background (cancer imaging). We demonstrated that the two modified key assumptions that lead to a new model are essential to accurately predict the echo phase shift among different phantom geometries. This consequently leads to substantially improved quantitative SoS images among all investigated phantoms.

Together with an extensive description of the theoretical principles of the two models, these results are presented in chapter 2 and published in:

- **P.Stähli**, M. Kuriakose, M. Frenz and M. Jaeger, Improved Forward Model for Quantitative Pulse-Echo Speed-of-Sound Imaging, *Ultrasonics*, doi:10.1016/j.ultras.2020.106168

As mentioned, the SoS is reconstructed by solving the inverse problem of Eq. 3.1. Due to the ill-posed nature of this forward problem, small variations in the measurement – as e.g. caused by the measurement noise – result in a large and unpredictable change in the solution. To suppress the influence of the measurement noise on the solution, some sort of regularization can be included in the the inverse problem formulation. Regularization gives preference to a particular solution with desirable properties. Thereby, the meaning of desirable properties is defined *a priori*. Based on the expectation that the distribution of SoS inside a tissue does not vary strongly on a short spatial scale, a Tikhonov-type regularization of the spatial gradient (SG) of SoS was used in the previous study. In contrast to phantom experiments, the phase shift maps that are determined in in-vivo scenarios often suffer from a high level of phase noise. This phase noise is potentially caused by clutter, aberration and SoS variations in the sub-resolution range. Using the SG regularization, this often results in SoS images that suffer from a high level of artifacts. Further, the SoS of an organ (e.g the liver) is not reproducible when being imaged from different scanning locations.

To solve this shortcoming, a second main part of this thesis focused on the investigation of a Bayesian framework for the inverse calculation, inspired by applications from the geophysical inverse theories [72–76]. In contrast to the purely algebraic framework that was used to derive the Tikhonov-type inversion, the Bayesian framework treats all variables as random variable. The aim of the Bayesian inverse calcu-

lation is then to determine the posterior probability density on the space of possible solution. The posterior probability is the re-allocated probability distribution of the parameters (in our case, the SoS) after taking into account the observations. The most likely solution to the inverse problem is then given by the argmax of the posterior distribution.

A main advantage of the Bayesian framework is that it provides an intuitive way to include an *a priori* statistical model of the spatial distribution of SoS, characterized by expectation values, probability density distribution, and spatial correlation function. This model can be based on the B-mode images that are reconstructed as part of CUTE. Including such statistical *a priori* information leads to SoS images that are less prone to phase noise and thus leads to more reproducible SoS images compared to the SG regularization. In combination with the new forward model that was presented in the first publication, the Bayesian approach is a key step towards quantitative SoS imaging in in-vivo for e.g. diagnostic purposes.

Chapter 3 presents a description of the Bayesian framework for SoS reconstruction in pulse-echo mode and an evaluation of the performance of both regularization techniques in an extensive simulation and phantom study. In preparation of a clinical application, the techniques were also compared in an exemplary in-vivo scenario of imaging the abdominal wall and liver tissue, where a reproducibility of the liver's SoS in the range of 10 ms^{-1} was achieved. The work that is presented in chapter 3 has been submitted to:

- **P.Stähli**, M. Frenz and M. Jaeger, Bayesian Approach for a Robust Speed-of-Sound Reconstruction Using Pulse-Echo Ultrasound, (Submitted to IEEE Transaction on Medical Imaging in March 2020, revision in process)

So far, tissue motion was assumed to be negligible when tracking the phase shift. This is reasonable when imaging organs as e.g the liver, since the imaged person can minimize its own motion (e.g by holding the breath) and acquisition can be synchronized with the heart beat. When imaging the lumen of large blood vessels, however, blood flow inhibits phase tracking of blood echoes. Moreover, the weak amplitude of the blood echoes is overlaid by tissue clutter and further complicates phase tracking. With the goal to enlarge the applicability of CUTE to enable the assessment of atherosclerotic plaque composition inside the carotid artery, a third part of this thesis focused on the investigation of two modifications to the CUTE methodology: a) receive beam-steering as opposed to transmit beam-steering to increase acquisition speed and reduce flow-related phase decorrelation, and (b) pairwise subtraction of data obtained from repetitions of the scan sequence to highlight blood echoes relative to static echo clutter. In chapter 4, the implementation of the two modifications to the CUTE methodology are described. In a phantom study, we demonstrated that these modifications results in SoS images of the same quality as

obtained with the previously used Tx-steering, which is a key step towards successful imaging of the SoS inside the carotid artery. These findings have been published in:

- M. Kuriakose, J. Muller, **P. Stähli**, M. Frenz and M.Jaeger, Receive Beam-Steering and Clutter Reduction for Imaging the Speed-of-Sound Inside the Carotid Artery, Journal of Imaging, 2018, doi:10.3390/jimaging4120145.

References

- [1] W. C. Röntgen, “On a new kind of rays,” *Science*, vol. 3, no. 59, pp. 227–231, 1896.
- [2] A. B. Reed, “The history of radiation use in medicine,” 2011.
- [3] R. F. Mould, “The early history of x-ray diagnosis with emphasis on the contributions of physics 1895-1915,” *Physics in Medicine & Biology*, vol. 40, no. 11, p. 1741, 1995.
- [4] J. H. Scatliff and P. J. Morris, “From röntgen to magnetic resonance imaging the history of medical imaging,” *North Carolina medical journal*, vol. 75, no. 2, pp. 111–113, 2014.
- [5] M. Angell, J. Kassirer, and A. Relman, “Looking back on the millennium in medicine [editorial],” *N Engl J Med*, vol. 342, no. 1, pp. 42–49, 2000.
- [6] S. Gummadi, J. Eisenbrey, J. Li, Z. Li, F. Forsberg, A. Lyshchik, and J.-B. Liu, “Advances in modern clinical ultrasound,” *Advanced Ultrasound in Diagnosis and Therapy*, vol. 2, no. 2, pp. 51–63, 2018.
- [7] J. Joy, I. Cooke, and M. Love, “Is ultrasound safe?,” *The Obstetrician & Gynaecologist*, vol. 8, no. 4, pp. 222–227, 2006.
- [8] D. L. Miller, “Safety assurance in obstetrical ultrasound,” in *Seminars in Ultrasound, CT and MRI*, vol. 29, pp. 156–164, Elsevier, 2008.
- [9] “Copyright,” in *Clinical Ultrasound (Third Edition)* (P. L. Allan, G. M. Baxter, and M. J. Weston, eds.), p. iv, Edinburgh: Churchill Livingstone, third edition ed., 2011.
- [10] B. S. Hertzberg and W. D. Middleton, *Ultrasound: The Requisites E-Book*. Elsevier Health Sciences, 2015.
- [11] J. Cleve and M. L. McCulloch, “Conducting a cardiac ultrasound examination,” in *Echocardiography*, pp. 33–42, Springer, 2018.
- [12] A. T. Stavros, D. Thickman, C. L. Rapp, M. A. Dennis, S. H. Parker, and G. A. Sisney, “Solid breast nodules: use of sonography to distinguish between benign and malignant lesions.,” *Radiology*, vol. 196, no. 1, pp. 123–134, 1995.
- [13] T. M. Kolb, J. Lichy, and J. H. Newhouse, “Comparison of the performance of screening mammography, physical examination, and breast us and evaluation of factors that influence them: an analysis of 27,825 patient evaluations,” *Radiology*, vol. 225, no. 1, pp. 165–175, 2002.

- [14] R. T Arntfield and S. J Millington, "Point of care cardiac ultrasound applications in the emergency department and intensive care unit-a review," *Current cardiology reviews*, vol. 8, no. 2, pp. 98–108, 2012.
- [15] R. Romero, "Routine obstetric ultrasound," *Ultrasound in Obstetrics and Gynecology: The Official Journal of the International Society of Ultrasound in Obstetrics and Gynecology*, vol. 3, no. 5, pp. 303–307, 1993.
- [16] H. Tchelepi, P. W. Ralls, R. Radin, and E. Grant, "Sonography of diffuse liver disease," *Journal of Ultrasound in Medicine*, vol. 21, no. 9, pp. 1023–1032, 2002.
- [17] T. Nishiura, H. Watanabe, M. Ito, Y. Matsuoka, K. Yano, M. Daikoku, H. Yatsushashi, K. Dohmen, and H. Ishibashi, "Ultrasound evaluation of the fibrosis stage in chronic liver disease by the simultaneous use of low and high frequency probes," *The British journal of radiology*, vol. 78, no. 927, pp. 189–197, 2005.
- [18] K. Dewbury and B. Clark, "The accuracy of ultrasound in the detection of cirrhosis of the liver," *The British journal of radiology*, vol. 52, no. 624, pp. 945–948, 1979.
- [19] R. Santambrogio, P. Bianchi, A. Pasta, A. Palmisano, and M. Montorsi, "Ultrasound-guided interventional procedures of the liver during laparoscopy," *Surgical Endoscopy And Other Interventional Techniques*, vol. 16, no. 2, pp. 349–354, 2002.
- [20] D. N. Smith, M. L. Rosenfield Darling, J. E. Meyer, C. M. Denison, D. I. Rose, S. Lester, A. Richardson, C. M. Kaelin, E. Rhei, and R. L. Christian, "The utility of ultrasonographically guided large-core needle biopsy: results from 500 consecutive breast biopsies.," *Journal of ultrasound in medicine*, vol. 20, no. 1, pp. 43–49, 2001.
- [21] A. T. Gray, "Ultrasound-guided regional anesthesia," *Anesthesiology*, vol. 104, no. 2, pp. 368–73, 2006.
- [22] P. Therasse, S. G. Arbuck, E. A. Eisenhauer, J. Wanders, R. S. Kaplan, L. Rubinstein, J. Verweij, M. Van Glabbeke, A. T. van Oosterom, M. C. Christian, *et al.*, "New guidelines to evaluate the response to treatment in solid tumors," *Journal of the National Cancer Institute*, vol. 92, no. 3, pp. 205–216, 2000.
- [23] J. Tonetti, L. Carrat, S. Blendea, P. Merloz, J. Troccaz, S. Lavallée, and J.-P. Chirossel, "Clinical results of percutaneous pelvic surgery. computer assisted surgery using ultrasound compared to standard fluoroscopy," *Computer Aided Surgery*, vol. 6, no. 4, pp. 204–211, 2001.

- [24] T. J. Mason, “Therapeutic ultrasound an overview,” *Ultrasonics sonochemistry*, vol. 18, no. 4, pp. 847–852, 2011.
- [25] F. Jácome-Pita, R. Sánchez-Salas, E. Barret, N. Amaruch, C. Gonzalez-Enguita, and X. Cathelineau, “Focal therapy in prostate cancer: the current situation,” *Ecancermedicalscience*, vol. 8, 2014.
- [26] B. Hamm, “Differential diagnosis of scrotal masses by ultrasound,” *European radiology*, vol. 7, no. 5, pp. 668–679, 1997.
- [27] J. Baker, P. J. Kornguth, M. S. Soo, R. Walsh, and P. Mengoni, “Sonography of solid breast lesions: observer variability of lesion description and assessment.,” *AJR. American journal of roentgenology*, vol. 172, no. 6, pp. 1621–1625, 1999.
- [28] G. Rahbar, A. C. Sie, G. C. Hansen, J. S. Prince, M. L. Melany, H. E. Reynolds, V. P. Jackson, J. W. Sayre, and L. W. Bassett, “Benign versus malignant solid breast masses: Us differentiation,” *Radiology*, vol. 213, no. 3, pp. 889–894, 1999.
- [29] K. Konno, H. Ishida, M. Sato, T. Komatsuda, J. Ishida, H. Naganuma, Y. Hamashima, and S. Watanabe, “Liver tumors in fatty liver: difficulty in ultrasonographic interpretation,” *Abdominal imaging*, vol. 26, no. 5, pp. 487–491, 2001.
- [30] E. M. Arribas, G. J. Whitman, and N. De Bruhl, “Screening breast ultrasound: where are we today?,” *Current Breast Cancer Reports*, vol. 8, no. 4, pp. 221–229, 2016.
- [31] S. Strauss, E. Gavish, P. Gottlieb, and L. Katsnelson, “Interobserver and intraobserver variability in the sonographic assessment of fatty liver,” *American Journal of Roentgenology*, vol. 189, no. 6, pp. W320–W323, 2007.
- [32] M. Fishbein, F. Castro, S. Cheruku, S. Jain, B. Webb, T. Gleason, and W. R. Stevens, “Hepatic mri for fat quantitation: its relationship to fat morphology, diagnosis, and ultrasound,” *Journal of clinical gastroenterology*, vol. 39, no. 7, pp. 619–625, 2005.
- [33] C. Stern and L. Castera, “Non-invasive diagnosis of hepatic steatosis,” *Hepatology international*, vol. 11, no. 1, pp. 70–78, 2017.
- [34] B. Palmentieri, I. De Sio, V. La Mura, M. Masarone, R. Vecchione, S. Bruno, R. Torella, and M. Persico, “The role of bright liver echo pattern on ultrasound b-mode examination in the diagnosis of liver steatosis,” *Digestive and Liver Disease*, vol. 38, no. 7, pp. 485–489, 2006.

- [35] A. E. Bohte, J. R. van Werven, S. Bipat, and J. Stoker, “The diagnostic accuracy of us, ct, mri and 1 h-mrs for the evaluation of hepatic steatosis compared with liver biopsy: a meta-analysis,” *European radiology*, vol. 21, no. 1, pp. 87–97, 2011.
- [36] N. S. Anavekar and J. K. Oh, “Doppler echocardiography: a contemporary review,” *Journal of Cardiology*, vol. 54, no. 3, pp. 347–358, 2009.
- [37] K. L. Hansen, M. B. Nielsen, and C. Ewertsen, “Ultrasonography of the kidney: a pictorial review,” *Diagnostics*, vol. 6, no. 1, p. 2, 2016.
- [38] M. M. Doyley, J. C. Bamber, F. Fuechsel, and N. L. Bush, “A freehand elastographic imaging approach for clinical breast imaging: system development and performance evaluation,” *Ultrasound in medicine & biology*, vol. 27, no. 10, pp. 1347–1357, 2001.
- [39] T. Shiina, N. Nitta, E. Ueno, and J. C. Bamber, “Real time tissue elasticity imaging using the combined autocorrelation method,” *Journal of Medical Ultrasonics*, vol. 29, no. 3, pp. 119–128, 2002.
- [40] T. J. Hall, Y. Zhu, and C. S. Spalding, “In vivo real-time freehand palpation imaging,” *Ultrasound in medicine & biology*, vol. 29, no. 3, pp. 427–435, 2003.
- [41] K. Kato, H. Sugimoto, N. Kanazumi, S. Nomoto, S. Takeda, and A. Nakao, “Intra-operative application of real-time tissue elastography for the diagnosis of liver tumours,” *Liver International*, vol. 28, no. 9, pp. 1264–1271, 2008.
- [42] K. J. Parker, M. M. Doyley, and D. J. Rubens, “Imaging the elastic properties of tissue: the 20 year perspective,” *Physics in medicine & biology*, vol. 56, no. 1, p. R1, 2010.
- [43] K. Nightingale, M. S. Soo, R. Nightingale, and G. Trahey, “Acoustic radiation force impulse imaging: in vivo demonstration of clinical feasibility,” *Ultrasound in medicine & biology*, vol. 28, no. 2, pp. 227–235, 2002.
- [44] J. Bercoff, M. Tanter, and M. Fink, “Supersonic shear imaging: a new technique for soft tissue elasticity mapping,” *IEEE transactions on ultrasonics, ferroelectrics, and frequency control*, vol. 51, no. 4, pp. 396–409, 2004.
- [45] D. Melodelima, J. C. Bamber, F. A. Duck, J. A. Shipley, and L. Xu, “Elastography for breast cancer diagnosis using radiation force: System development and performance evaluation,” *Ultrasound in medicine & biology*, vol. 32, no. 3, pp. 387–396, 2006.

- [46] J. F. Greenleaf, S. A. Johnson, W. F. Samayoa, and F. A. Duck, “Algebraic reconstruction of spatial distributions of acoustic velocities in tissue from their time-of-flight profiles,” in *Acoustical holography*, pp. 71–90, Springer, 1975.
- [47] G. Glover and J. Sharp, “Reconstruction of ultrasound propagation speed distributions in soft tissue: time-of-flight tomography,” *IEEE Transactions on sonics and ultrasonics*, vol. 24, no. 4, pp. 229–234, 1977.
- [48] N. Duric, P. Littrup, O. Rama, and E. Holsapple, “Computerized ultrasound risk evaluation (cure): First clinical results,” in *Acoustical Imaging*, pp. 173–181, Springer, 2007.
- [49] J. Wiskin, D. Borup, S. Johnson, and M. Berggren, “Non-linear inverse scattering: High resolution quantitative breast tissue tomography,” *The Journal of the Acoustical Society of America*, vol. 131, no. 5, pp. 3802–3813, 2012.
- [50] G. Sandhu, C. Li, O. Roy, S. Schmidt, and N. Duric, “Frequency domain ultrasound waveform tomography: breast imaging using a ring transducer,” *Physics in Medicine & Biology*, vol. 60, no. 14, p. 5381, 2015.
- [51] J. Wiskin, B. Malik, R. Natesan, and M. Lenox, “Quantitative assessment of breast density using transmission ultrasound tomography,” *Medical physics*, vol. 46, no. 6, pp. 2610–2620, 2019.
- [52] R. Natesan, J. Wiskin, S. Lee, and B. H. Malik, “Quantitative assessment of breast density: transmission ultrasound is comparable to mammography with tomosynthesis,” *Cancer Prevention Research*, vol. 12, no. 12, pp. 871–876, 2019.
- [53] M. E. Anderson and G. E. Trahey, “The direct estimation of sound speed using pulse–echo ultrasound,” *The Journal of the Acoustical Society of America*, vol. 104, no. 5, pp. 3099–3106, 1998.
- [54] F. R. Pereira, J. C. Machado, and W. C. Pereira, “Ultrasonic wave speed measurement using the time-delay profile of rf-backscattered signals: Simulation and experimental results,” *The Journal of the Acoustical Society of America*, vol. 111, no. 3, pp. 1445–1453, 2002.
- [55] J. Krucker, J. B. Fowlkes, and P. L. Carson, “Sound speed estimation using automatic ultrasound image registration,” *IEEE transactions on ultrasonics, ferroelectrics, and frequency control*, vol. 51, no. 9, pp. 1095–1106, 2004.
- [56] H.-C. Shin, R. Prager, H. Gomersall, N. Kingsbury, G. Treece, and A. Gee, “Estimation of average speed of sound using deconvolution of medical ultrasound data,” *Ultrasound in medicine & biology*, vol. 36, no. 4, pp. 623–636, 2010.

- [57] M. Imbault, A. Faccinnetto, B.-F. Osmanski, A. Tissier, T. Deffieux, J.-L. Gennisson, V. Vilgrain, and M. Tanter, “Robust sound speed estimation for ultrasound-based hepatic steatosis assessment,” *Physics in Medicine and Biology*, vol. 62, no. 9, p. 3582, 2017.
- [58] M. D. Burgio, M. Imbault, M. Ronot, A. Faccinnetto, B. E. Van Beers, P.-E. Rautou, L. Castera, J.-L. Gennisson, M. Tanter, and V. Vilgrain, “Ultrasonic adaptive sound speed estimation for the diagnosis and quantification of hepatic steatosis: a pilot study,” *Ultraschall in der Medizin-European Journal of Ultrasound*, vol. 40, no. 06, pp. 722–733, 2019.
- [59] F. Natterer, “Reflectors in wave equation imaging,” *Wave Motion*, vol. 45, no. 6, pp. 776–784, 2008.
- [60] F. Natterer, “Ultrasound mammography with a mirror,” *Physics in Medicine & Biology*, vol. 55, no. 10, p. N275, 2010.
- [61] M. C. Hesse, L. Salehi, and G. Schmitz, “Nonlinear simultaneous reconstruction of inhomogeneous compressibility and mass density distributions in unidirectional pulse-echo ultrasound imaging,” *Physics in Medicine and Biology*, vol. 58, no. 17, p. 6163, 2013.
- [62] M. Kondo, K. Takamizawa, M. Hirama, K. Okazaki, K. Iinuma, and Y. Takehara, “An evaluation of an in vivo local sound speed estimation technique by the crossed beam method,” *Ultrasound in Medicine and Biology*, vol. 16, no. 1, pp. 65–72, 1990.
- [63] J. Ophir, “Estimation of the speed of ultrasound propagation in biological tissues: A beam-tracking method,” *IEEE transactions on ultrasonics, ferroelectrics, and frequency control*, vol. 33, no. 4, pp. 359–368, 1986.
- [64] I. Céspedes, J. Ophir, and Y. Huang, “On the feasibility of pulse-echo speed of sound estimation in small regions: Simulation studies,” *Ultrasound in Medicine and Biology*, vol. 18, no. 3, pp. 283–291, 1992.
- [65] B. C. Byram, G. E. Trahey, and J. A. Jensen, “A method for direct localized sound speed estimates using registered virtual detectors,” *Ultrasonic imaging*, vol. 34, no. 3, pp. 159–180, 2012.
- [66] M. Jakovljevic, S. Hsieh, R. Ali, G. Chau Loo Kung, D. Hyun, and J. J. Dahl, “Local speed of sound estimation in tissue using pulse-echo ultrasound: Model-based approach,” *The Journal of the Acoustical Society of America*, vol. 144, no. 1, pp. 254–266, 2018.

- [67] M. Jaeger, G. Held, S. Peeters, S. Preisser, M. Grünig, and M. Frenz, “Computed ultrasound tomography in echo mode for imaging speed of sound using pulse-echo sonography: proof of principle,” *Ultrasound in medicine and biology*, vol. 41, no. 1, pp. 235–250, 2015.
- [68] M. Jaeger and M. Frenz, “Towards clinical computed ultrasound tomography in echo-mode: Dynamic range artefact reduction,” *Ultrasonics*, vol. 62, pp. 299–304, 2015.
- [69] M. Jaeger and M. Frenz, “Quantitative imaging of speed of sound in echo ultrasonography.” IEEE International Ultrasound Symposium, Taipei, 2015.
- [70] S. J. Sanabria, E. Ozkan, M. Rominger, and O. Goksel, “Spatial domain reconstruction for imaging speed-of-sound with pulse-echo ultrasound: simulation and in vivo study,” *Physics in Medicine & Biology*, vol. 63, no. 21, p. 215015, 2018.
- [71] L. Ruby, S. J. Sanabria, K. Martini, K. J. Dedes, D. Vorburger, E. Oezkan, T. Frauenfelder, O. Goksel, and M. B. Rominger, “Breast cancer assessment with pulse-echo speed of sound ultrasound from intrinsic tissue reflections: Proof-of-concept,” *Investigative radiology*, vol. 54, no. 7, pp. 419–427, 2019.
- [72] A. Tarantola and B. Valette, “Generalized nonlinear inverse problems solved using the least squares criterion,” *Reviews of Geophysics*, vol. 20, no. 2, pp. 219–232, 1982.
- [73] W. P. Gouveia and J. A. Scales, “Bayesian seismic waveform inversion: Parameter estimation and uncertainty analysis,” *Journal of Geophysical Research: Solid Earth*, vol. 103, no. B2, pp. 2759–2779, 1998.
- [74] A. Malinverno, “A bayesian criterion for simplicity in inverse problem parametrization,” *Geophysical Journal International*, vol. 140, no. 2, pp. 267–285, 2000.
- [75] K. Mosegaard and A. Tarantola, “Monte carlo sampling of solutions to inverse problems,” *Journal of Geophysical Research: Solid Earth*, vol. 100, no. B7, pp. 12431–12447, 1995.
- [76] A. P. Valentine and M. Sambridge, “Optimal regularization for a class of linear inverse problem,” *Geophysical Journal International*, vol. 215, no. 2, pp. 1003–1021, 2018.

Chapter 2

Improved forward model for quantitative pulse-echo speed-of-sound imaging

PATRICK STÄHLI¹, MAJU KURIAKOSE¹, MARTIN FRENZ¹, MICHAEL JAEGER¹

Abstract

Computed ultrasound tomography in echo mode (CUTE) allows determining the spatial distribution of speed-of-sound (SoS) inside tissue using handheld pulse-echo ultrasound (US). This technique is based on measuring the changing phase of beam-formed echoes obtained under varying transmit (Tx) and/or receive (Rx) steering angles. The SoS is reconstructed by inverting a forward model describing how the spatial distribution of SoS is related to the spatial distribution of the echo phase shift. Thanks to the straight-ray approximation, this forward model is linear and can be inverted in real-time when implemented in a state-of-the art system. Here we demonstrate that the forward model must contain two features that were not taken into account so far: a) the phase shift must be detected between pairs of Tx and Rx angles that are centred around a set of common mid-angles, and b) it must account for an additional phase shift induced by the offset of the reconstructed position of echoes. In a phantom study mimicking hepatic and cancer imaging, we show that both features are required to accurately predict echo phase shift among different phantom geometries, and that substantially improved quantitative SoS images are obtained compared to the model that has been used so far. The importance of the new model is corroborated by a preliminary volunteer result.

The work presented in this chapter has been published in the Ultrasonics journal. doi:10.1016/j.ultras.2020.106168.

¹Institute of Applied Physics, University of Bern, Sidlerstrasse 5, 3012 Bern, Switzerland

2.1 Introduction

Ultrasound (US) is an integral part of today's clinical diagnostic practice since it provides us with real time display and flexible free-hand probe guidance while using non-ionizing radiation. The compact, portable and comparably inexpensive US systems make their use favourable for general practitioners, emergency units and bed-side care. On the downside, classical gray-scale B-mode US often suffers from low sensitivity and non-specific contrast, resulting in difficulties in differential diagnosis for certain disease types [1–3]. To complement B-mode images with additional structural and functional information in a single multi-modal system, much effort has been placed in developing new ultra-sound-based modalities. Apart from Doppler flow imaging, which is already state-of-the-art, recent developments include ultrasound elastography [4–9] and optoacoustic imaging [10–13].

Based on the dependence of the SoS on the tissues mechanical properties, SoS imaging is another promising modality that can help identify disease-related changes of tissue composition and structure. Breast ultrasound computed tomography (UCT) showcases the potential of SoS imaging on the example of breast cancer diagnosis [14]. In UCT, US is through-transmitted through the breast from many angles, and the spatial distribution of SoS is reconstructed based on analysing the detected US signals. In the ray approximation of ultrasound propagation, the time-of-flight (ToF) of pulsed signals is assigned to integrals of slowness (inverse of SoS) along lines connecting sender and receiver locations [15–18]. This allows a fast linear reconstruction of the SoS, e.g. via the filtered backprojection, but with the disadvantage of a low spatial resolution due to diffraction and refraction. Refraction can be accounted for in an iterative bent-ray ToF approach. Diffraction, however, requires methods that use the full signal as opposed to the ToF. Diffraction tomography based on the 1st order Born approximation is linear and fast, but limited to low contrast SoS variations so that its application to the breast requires a SoS prior with "reasonable low resolution" [19]. The best in-vivo images were so far obtained using non-linear iterative full-wave inversion schemes, but with the disadvantage of a high numerical cost [20, 21].

Whereas UCT is able to achieve high resolution and quantitative SoS images of breast cancer, the big disadvantage is that it is a through-transmission technique, which limits its use to acoustically transparent parts of the human body. To provide SoS imaging with all the flexibility of conventional handheld US and without the need for specialized equipment, SoS imaging must be based on echo US for a one-sided access. This would allow to not only image the SoS in transparent parts of the body, but also in any other part that is routinely examined using echo US, e.g. for the diagnosis of cancer other than in the breast, of fatty liver disease, or for the assessment of plaque composition inside the carotid artery.

Reflection-mode SoS imaging is feasible when taking into account a multiple-scattering process beyond the 1st order Born approximation. This problem can in principle be solved as in UCT in a non-linear full-wave inversion. Even though promising theoretical results were obtained using this approach in 2D digital breast phantoms [22], no clinical results have been presented so far, potentially because it requires low frequencies outside the bandwidth of conventional clinical US probes. Various alternative approaches were investigated that reconstruct the SoS based on pulse-echo signals. Techniques that estimate the average SoS between the transducer and the focal depth reported accurate SoS measurements of uniform tissue [23–25]. These methods, however, have low accuracy in the presence of SoS inhomogeneities. The crossed-beam tracking method is based on measuring the round-trip time through the intersection of two scanning beams (one for transmit, one for receive), and provides a spatial resolution on the order of 10 mm [26, 27]. Recently, an approach was proposed that reconstructs the local SoS based on axial variations of the average SoS determined by optimizing the transmit and receive focusing. The technique was verified in phantoms without lateral SoS variations, where it provided an axial resolution of about 7 mm [28].

We have recently developed a reflection-mode technique, named computed ultrasound tomography in echo-mode (CUTE), which allows a real time determination of the SoS with promising spatial and contrast resolution [29, 30]. CUTE is based on analysing the spatial distribution of the echo phase in beamformed (using e.g. conventional delay-and-sum algorithm) radio-frequency (rf) mode US images. A deviation of the true SoS from the value assumed for beamforming results in a mismatch between the anticipated and the actual round-trip time of US propagation (henceforth termed ‘aberration delay’). A changing value of the aberration delay when detecting echoes under varying angles of ultrasound transmission and/or reception consequently results in a phase shift of these echoes, which is quantified in a spatially resolved way by e.g. Loupas type phase correlation[31]. This concept is closely related to approaches that analyze the differential echo phase as function of transducer element position, to correct for aberrations caused by superficial SoS variations that act like a phase screen directly in front of the transducer aperture [32–37]. CUTE goes, however, beyond these approaches: by determining the phase shift in the beamformed images as opposed to the channel data, lateral resolution of phase shift data is achieved also away from the aperture. Based on a model of how the spatial distribution of SoS relates to the spatially resolved phase shift, the former can thus be reconstructed by solving the inverse problem. Under the straight-ray approximation, the inverse problem can be linearised via a pseudo-inverse matrix, enabling real-time SoS imaging with a spatial resolution of a couple of mm. Apart from serving as a source of diagnostic information, knowledge of the spatial distribution of SoS allows for aberration correction

beyond the phase screen assumption [38, 39].

The core of CUTE is the forward model that relates the SoS to echo phase shift, and this forward model is closely linked to the data acquisition scheme. Previously, we proposed an implementation of CUTE where the rf-mode images were acquired under a variety of transmit (Tx) angles, whereas the echoes were detected with a constant receive (Rx) aperture [29]. The model (henceforth termed 'old model') was based on following key assumptions:

1. Because the Rx aperture is constant, the echo phase shift is entirely determined by the changing aberration delay along the changing Tx propagation directions.
2. The echo phase shift is proportional to the difference in aberration delay along different round-trip paths.

In [29, 30, 38], this forward model was formulated in the frequency-domain (FD). The FD formulation, however, cannot account for the absence of phase shift data in regions of low echo intensity, which leads to artefacts in the SoS image. Therefore we proposed that quantitative imaging requires a space-domain (SD) approach [40]. Sanabria et al. consequently described a methodology for SD reconstruction from theory to implementation, and verified in a simulation study the advantage of using an SD instead of an FD approach[41], including a preliminary clinical result. A more extensive clinical pilot was presented in [42]. In spite of promising results when using both the FD and the SD approach, we realized that - for known SoS distributions - the prediction of the phase shift that is made by the old model deviates from the measured phase shift. This disagreement is shown in Fig. 2.1 for two exemplary scenarios, a phantom with a cylindrical inclusion inside a uniform background and a four-layer phantom. In the case of a cylindrical inclusion, the old model roughly predicts the correct phase shift magnitude, which explains that a reasonably accurate SoS contrast could be reconstructed in similar phantoms in past studies. The profile shape, however, is wrongly predicted. In case of a layered phantom, the phase shift magnitude itself is underestimated by a factor of two. In both scenarios, the old model thus fails in accurately predicting the measured phase shift. As a consequence of this mismatch between forward model and reality, using the old model for SoS reconstruction leads to inconsistent SoS results depending on phantom geometry.

Here we present a new model that solves this shortcoming by modifying the two key assumptions of the old model as follows:

1. Even if the Rx aperture is held constant while changing the Tx angle, the echo phase shift contains the influence of a virtually changing Rx angle. To avoid ambiguities, we propose to switch from a pure Tx-steering approach to simultaneously steering both, the Tx- and the Rx- angle, around a variety of

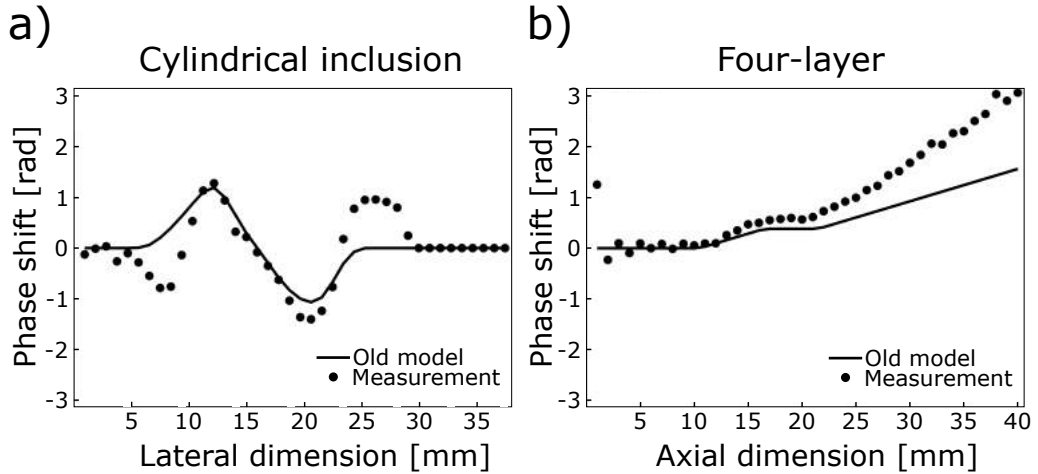


Figure 2.1: Comparison of the measured phase-shift to the prediction made by the old model, for a Tx angle step of $\phi_n \rightarrow \phi_{n'} = 5^\circ \rightarrow 15^\circ$, using the system described in Materials and Methods. (a) Phantom containing a cylindrical inclusion with a SoS contrast of $+30 \text{ ms}^{-1}$ in a uniform background (description in Materials and Methods), lateral profile. (b) Four-Layer phantom with a SoS contrast of 135 ms^{-1} (description in Materials and Methods), axial profile.

common mid-angles, in an approach similar to the common mid-point gather that has been used in seismic imaging [43] as well as in US [35–37].

2. The *a priori* unknown SoS distribution leads to an offset of the reconstructed position of echoes. This offset not only depends on the aberration delay, but independently also on the values of the steering angles. As a result, the initially assumed simple proportionality between the aberration delay and phase shift is no longer valid.

In the theory section, we revise the assumptions that led to the old model and then proceed to the development of the new model. In a phantom study, we then compare the old and the new model in various different phantoms that were designed in view of two specific target clinical applications, i.e. layered phantoms mimicking the abdominal wall and liver (hepatic imaging) and phantoms mimicking a circular lesion inside a layered background (cancer imaging, e.g. breast). The presented results reveal that the two features of the new model are required to accurately predict the echo phase shift among different phantom geometries, and that substantially improved quantitative SoS images are obtained among all investigated phantoms.

2.2 Theory

The theory is developed assuming a linear array probe for 2D imaging, but can be readily adapted to curved arrays, as well as to matrix arrays for 3D imaging. Fig. 2.2(a) illustrates the measurement geometry. The linear array probe (parallel to coordinate x) is placed on top of the tissue (at coordinate $z = 0$), and acquires echoes using a variety of different transmit and receive settings, indexed by n and m .

For the sake of visual and conceptual clarity, transmission and detection on single elements is considered in a first step in Fig. 2.2(a). Two different elements (indexed by el_n and $el_{n'}$) transmit an US pulse, one at a time. The two (in this case divergent) wave fronts reach a point $\mathbf{r}' = (x', z')$ inside the tissue under two different angles ϕ_n and $\phi_{n'}$. Intrinsic ultrasound reflectors located in a vicinity around \mathbf{r}' lead to echoes that propagate back to the surface, where they are detected by the different sensor elements (indexed el_m) under angles ψ_m resulting in radio frequency (rf) signals $s(t, n, m)$ with the time indexed by t . Note that the important point here is not the specific type of transmit and receive beamforming: independent of the type of beamforming, ultrasound arriving at and detected from a reflector under specific angles ϕ_n and ψ_m is assumed to have propagated along paths defined by these angles. Apart from transmitting on single elements (as used in [44]), alternative types are a scanning group of elements transmitting diverging waves, plane wave transmissions having different Tx angles [29, 30], or weakly focused or collimated scanning beams (as in a classical line-by-line scan). Similarly, alternatives to using single elements for reception are e.g. defocused groups of elements, steered collimated or focused groups of elements, steered receiving plane waves (or frequency-domain filtering of rx angles, as used in this study, see later on), etc.

2.2.1 The old model

Given a combination of transmit and receive setting (n, m) , the complex (analytic) rf-signal (crf-signal) generated by a single point reflector located at \mathbf{r}' can be modelled as a product of a complex exponential carrier modulated with a complex-valued envelope G :

$$s(t, n, m) = G(t - t_0(\mathbf{r}', n, m)) \exp [2\pi i f_0 (t - t_0(\mathbf{r}', n, m))] \quad (2.1)$$

where f_0 is the centre frequency, t_0 is the actual round-trip time of the echo, and the function G describes the complex envelope of the signal. We thereby assume that G is determined by the spatio-temporal impulse response of the US system alone (i.e. not influenced by the tissue's acoustic properties) and that any dependence on n or m has been removed by calibration. The old model was based on the following rationale: the delay-and-sum (DAS) beamformed crf-amplitude in a point \mathbf{r} at the true position of the point reflector \mathbf{r}' is:

$$\begin{aligned} u(\mathbf{r} = \mathbf{r}', n) &= \sum_m [s(\hat{t}_0(\mathbf{r}, n, m), n, m)] = \sum_m [s(\hat{t}_0(\mathbf{r}', n, m), n, m)] \\ &= \sum_m \{G((\hat{t}_0 - t_0)(\mathbf{r}', n, m)) \exp [2\pi i f_0 (\hat{t}_0 - t_0)(\mathbf{r}', n, m)]\} \end{aligned} \quad (2.2)$$

where \hat{t}_0 is the anticipated round-trip time for point \mathbf{r} , calculated based on an *a priori* SoS \hat{c} . Deviations of the true SoS $c(\mathbf{r})$ from the anticipated value $\hat{c}(\mathbf{r})$ lead to

a deviation of the actual round-trip time from the anticipated value. This deviation, termed aberration delay, consists of two parts: one is the delay $\tau_{tx}(\mathbf{r}', n)$ of the n -th transmitted wave front when propagating towards \mathbf{r}' , and the other one is the delay $\tau_{rx}(\mathbf{r}', m)$ of echoes propagating from \mathbf{r}' to the m -th receiving element, so that $t_0(\mathbf{r}', n, m) = \hat{t}_0(\mathbf{r}', n, m) + \tau_{tx}(\mathbf{r}', n) + \tau_{rx}(\mathbf{r}', m)$. With these aberration delays, Eq. 2.2 becomes (\mathbf{r}' is omitted for notational simplicity):

$$u(n) = \sum_m \{G(-\tau_{tx}(n) - \tau_{rx}(m)) \exp [2\pi i f_0 (-\tau_{tx}(n) - \tau_{rx}(m))]\} \quad (2.3)$$

Phase shift tracking is based on the following assumption: G varies ‘slowly’ compared to the oscillations of the exponential carrier, either implicitly due to the bandlimited frequency response of typical clinical US probes, or explicitly by bandpass filtering. For a sufficiently small difference between Tx angles ϕ_n and $\phi_{n'}$, the change in τ_{tx} will be small compared to the temporal variation of G , so that the value of G can be assumed constant and τ_{tx} can be replaced by its average $\overline{\tau_{tx}}$ in the envelope. Eq. 2.3 is then simplified to:

$$u(n) \simeq \exp(-2\pi i f_0 \tau_{tx}(n)) \sum_m [G(-\overline{\tau_{tx}} - \tau_{rx}(m)) \cdot \exp(-2\pi i f_0 \tau_{rx}(m))] \quad (2.4)$$

On the right-hand side of Eq. 2.4, only the complex pre-factor depends on n . The first processing step of CUTE when using the old model is the experimental determination of the change in this pre-factor as a function of n . This is achieved by determining a map of local echo phase shift $\Delta\Theta(\mathbf{r}, n, n')$, defined as the phase angle of the (locally averaged) point-wise Hermitian product between the crf-mode images obtained with Tx settings n and n' . At point $\mathbf{r} = \mathbf{r}'$:

$$\Delta\Theta(\mathbf{r}', n, n') := \arg \left[\int_{x'-0.5\Delta x}^{x'+0.5\Delta x} \int_{z'-0.5\Delta z}^{z'+0.5\Delta z} d\mathbf{r} \{u(\mathbf{r}, n) \cdot u^*(\mathbf{r}, n')\} \right] \quad (2.5)$$

The averaging over a limited area around \mathbf{r}' (‘tracking kernel’), with size Δx by Δz , improves the robustness of the phase determination. The size of the tracking kernel defines the trade-off between spatial and contrast resolution of CUTE. The old model is based on the assumption that the experimentally measured phase shift of an echo is determined by the phase shift at the true location \mathbf{r}' of the echo-generating reflector. Under this assumption and provided that the change in τ_{tx} , $\Delta\tau_{tx}$, is smaller than half the oscillation period $1/f_0$ (to avoid phase aliasing), the measured echo phase shift is – according to Eq. 2.4 – related to the Tx aberration delay $\tau_{tx}(\mathbf{r}', n)$, as:

$$\begin{aligned}
\Delta\Theta(\mathbf{r}', n, n') &\simeq 2\pi f_0 \Delta\tau_{tx}(\mathbf{r}', n, n') \\
&= 2\pi f_0 \{ \tau_{tx}(\mathbf{r}', n') - \tau_{tx}(\mathbf{r}', n) \}
\end{aligned} \tag{2.6}$$

Note that a $\Delta\tau_{tx}$ that fulfils the aliasing condition automatically also fulfils the condition for Eq. 2.4. A simple formula for the prediction of the aliasing limit given the angle step between ϕ_n and ϕ'_n does not exist, as it depends on the aberration delays and thus on the *a priori* unknown spatial distribution of the SoS. In practice, one can base such a prediction on simulating the τ_{tx} for an expected variety of possible SoS distributions, or directly on observing the presence/absence of aliasing in the experimental phase shift data.

To complete the forward model, the aberration delays need to be related to the spatial distribution of SoS. Similar to UCT, including US diffraction and refraction in the forward model is in principle feasible, but would result in a time-consuming iterative reconstruction. In view of real time SoS imaging, we thus adhere to the straight-ray approximation and relate $\tau_{tx}(\mathbf{r}', n)$ to line integrals of slowness deviation $\Delta\sigma(\mathbf{r}, n)$, along propagation angles ϕ_n – determined by the transmit setting n – from the transducer surface to point \mathbf{r}' :

$$\tau_{tx}(\mathbf{r}', n) = \int_{\phi_n}^{\mathbf{r}'} dl \left\{ \frac{1}{c(\mathbf{r})} - \frac{1}{\hat{c}(\mathbf{r})} \right\} \equiv \int_{\phi_n}^{\mathbf{r}'} dl \Delta\sigma(\mathbf{r}) \tag{2.7}$$

Given the abundance of point reflectors in tissue, the function $\Delta\Theta(\mathbf{r}', n, n')$ can be measured not only at one point but (ideally) throughout the imaging plane. The old model is based on the assumption that the phase shift measured from any echo corresponding to a point reflector is independent from the absence/presence of nearby reflectors. By inverting the forward model consisting of Eq. 2.6 and Eq. 2.7, an estimated spatial distribution of SoS $c'(\mathbf{r})$ can then be reconstructed from $\Delta\Theta$.

2.2.2 New model

As mentioned in the Introduction, the new model involves two fundamental changes to the CUTE methodology: in a first step, the common mid-angle (CMA) approach is motivated. In a second step, we take into account the position offset of the reconstructed echoes.

Common mid-angle tracking

A first important prerequisite for the old model expressed in Eq. 2.6 was the assumption that G did not depend on n nor m , and thus the signal depended on n and m only via the aberration delays. In reality, however, G itself can depend on

n and m : a) lateral gradients of the distribution of SoS result in wave front aberrations that distort the shape of G in a spatially non-uniform way. We continue assuming that SoS variations are moderate enough so that this part is negligible. b) The spatial distribution of the tissue’s reflectivity function leads to coherently interfering echoes. The influence of the tissue’s reflectivity function can by no means be neglected, as it is precisely the echoes generated by this function that CUTE is based on. The effect this can have is illustrated for two extreme (but commonly found) cases:

- Specular reflector: the echo from a reflector intersecting with \mathbf{r}' propagates back to the probe along a direction ψ – determined by the mirror law – that varies opposite to a varying ϕ_n .
- Uniform diffuse scattering: The echoes from a dense (below spatial resolution cell) and random distribution of ‘point’ reflectors interfere at the aperture. The signal detected at the aperture decorrelates with changing n , because the relative round-trip times of the different echoes change.

In both cases, and in a more general scenario, the spatial distribution of the tissue’s reflectivity function leads to a dependence of G itself on n and m , and the relation between the aberration delay and the measured echo phase shift becomes ambiguous. To avoid such ambiguities, we introduce a fundamental change to the CUTE methodology: common mid-angle (CMA) tracking. In this technique, crf-mode images are reconstructed for pairs of Tx angles ϕ_n and Rx angles ψ_m that have the same mid-angle. Similar to the common mid-point approach that was previously used in aberration correction [38], the CMA approach makes use of the following fact: signals obtained under angle pairs $(\phi_n | \psi_m)$ grouped around the same mid-angle $\gamma = 0.5(\phi_n + \psi_m)$ are well correlated, independent of the spatial distribution of US reflectors. For illustration, Fig. 2.2(b) shows a scale-up of a small region around point \mathbf{r}' , containing a number of point reflectors. Each reflector is the pivot of an isochrone, a line that connects all points that would lead — for a specific pair $(\phi_n | \psi_m)$ — to the detection of an echo at an identical time. We assume that the curvature of the isochrones (which may result from the beamforming and/or from wave front distortions due to a non-uniform SoS) is negligible over the size of the observed region, so that the isochrones can be approximated as straight lines. When changing ϕ_n to $\phi_{n'}$ without changing ψ_m (Fig. 2.2(c)), the distances between the isochrones change, leading to a changing interference of the reflected echoes and thus to decorrelation of the signal that is detected from direction ψ_m . When changing ψ_m in opposite direction to $\psi_{m'}$ (Fig. 2.2(d)) such that the mid-angle in the pairs $(\phi_n | \psi_m)$ and $(\phi_{n'} | \psi_{m'})$ is fixed (so that $\gamma = 0.5(\phi_n + \psi_m) = \gamma' = 0.5(\phi_{n'} + \psi_{m'})$), then the relative distances between isochrones are not altered, and thus the signal

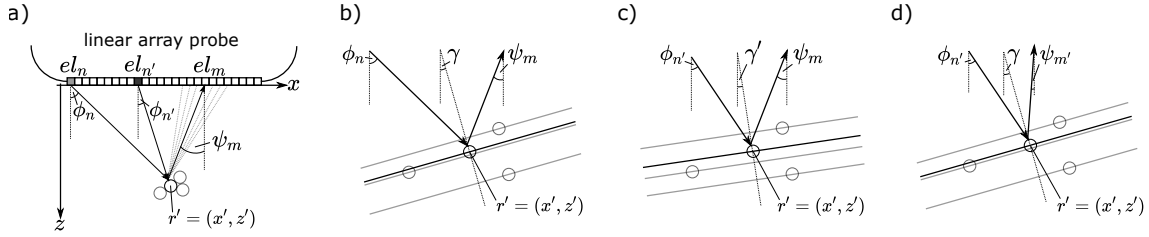


Figure 2.2: a) Sketch of a pulse-echo detection geometry. Ultrasound propagation paths are indicated, leading from different elements el_n towards a point reflector at \mathbf{r}' (circles) and back to an element el_m . b-d) Zoom-up of the region around \mathbf{r}' , showing the isochrones through various point reflectors when detected under different pairs of Tx and Rx angles. Only when angles are grouped around the same mid-angle (b and d) the relative position of isochrones is unchanged, thus avoiding echo decorrelation during phase tracking.

is well correlated. Note that the isochrones do not need to be constructed as part of the theoretical derivations, but are merely used as a didactic concept to illustrate why CMA tracking leads to correlated echoes independent of tissue reflectivity. The CMA approach can also be understood along the perspective of the k-space representation of the pulse-echo system response [45]: the system response corresponding to an angle pair $(\phi | \psi)$ detects a line in the 2D spatial Fourier transform of (an area of) the tissue's reflectivity function, along k-vectors pointing into the direction given by the mid-angle $0.5(\phi + \psi)$. Crf images (or an area thereof) acquired with angle pairs resulting in the same mid-angle thus sample the same line of the k-space representation of the reflectivity function, resulting in correlated echoes. Angle pairs corresponding to different mid-angles sample different lines in k-space resulting in uncorrelated echoes (unless the reflectivity function itself is correlated in k-space such as in the case of a single point reflector).

To employ the CMA approach, we reconstruct crf-mode images $u(\mathbf{r}, n, g)$ where n indexes the Tx setting resulting in a Tx angle ϕ_n as before, and the new index g indexes the mid-angle γ_g out of a set of mid-angles. Both together define the receive angle $\psi_{n,g} := \psi_{m(n,g)} = 2\gamma_g - \phi_n$. This way of indexing the Rx angle takes into account that – for a given mid-angle – the Rx angle cannot be freely chosen, but is determined by the Tx angle. Accordingly, the phase correlation is adapted from Eq. 2.5 to:

$$\Delta\Theta(\mathbf{r}', n, n', g) := \arg \left[\int_{x-0.5\Delta x}^{x+0.5\Delta x} \int_{z-0.5\Delta z}^{z+0.5\Delta z} d\mathbf{r} (u(\mathbf{r}, n, g) \cdot u^*(\mathbf{r}, n', g)) \right] \quad (2.8)$$

CUTE is based on evaluating echo phase shifts in crf-mode images as opposed to channel data because this better allows to spatially resolve the influence of the SoS on the echo phase shift of different echoes. In the old model, the lateral resolution of the crf-mode images was achieved via Rx focusing (weak synthetic Tx focusing was

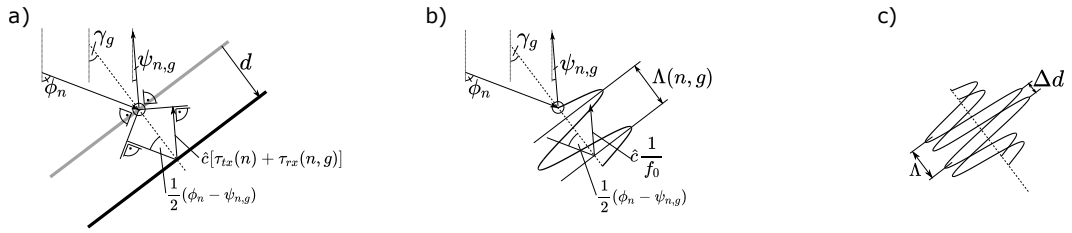


Figure 2.3: a) Geometrical sketch showing the relation between a Tx/Rx angle pair $(\phi_n | \psi_{n,g})$, the aberration delays $(\tau_{tx}(n), \tau_{rx}(n, g))$, and the spatial offset d of an isochrone. b) Similar sketch showing the relation between the centre frequency f_0 and the echo's spatial oscillation period $\Lambda(n, g)$. c) The measured phase shift is determined by the ratio between the shift $\Delta d(n, n', g)$ of the offset of the echo and Λ .

added mainly to reduce clutter noise). In the CMA approach, when reconstructing images with sharp ϕ_n and ψ_m , no lateral resolution would be obtained. Therefore, to achieve lateral resolution, a non-zero Rx angular aperture must be used together with a non-zero Tx angular aperture for combined Tx- and Rx beamforming. In comparison to the old model where the Rx angular aperture could in principle make use of the full transducer aperture, it must be chosen substantially smaller in the CMA approach so as to resolve different Rx steering angles. One has to keep in mind that reducing the Rx angular aperture goes hand-in-hand with a reduced lateral resolution of the crf-mode images, limiting in turn the lateral resolution of the final SoS image. We consider this an acceptable drawback of CMA tracking, compared to the big advantage of enabling improved SoS accuracy.

Echo position offset model

A second important assumption of the old model was the evaluation of the echo phase shift at the true location of the ultrasound reflector ($\mathbf{r} = \mathbf{r}'$). It is, however, not the phase shift at the true location of the reflector that determines the value of the measured phase shift, but the phase shift due to the spatial shift of the reconstructed position of the echo. As a second fundamental modification to the CUTE methodology, this is taken into account by the new model.

To derive the new model of how aberration delays relate to the echo phase shift, we again use the concept of the isochrones (Fig. 2.3). We assume a reflector (point or plane) that is detected with a specific angle pair $(\phi_n | \psi_{m,n})$. The total aberration delay (in Fig. 2.3(a) assumed larger than zero) leads to an offset of the reconstructed position of the echo, away from the true location of the reflector, to the isochrone for which the anticipated round-trip time agrees with the actual round-trip time. The offset d between the location of the reflector and the isochrone is – according to the geometric considerations depicted in Fig. 2.3(a) – given by:

$$d(n, g) = \frac{\hat{c}[\tau_{tx}(n) + \tau_{rx}(n, g)]}{2 \cos\left[\frac{1}{2}(\phi_n - \psi_{n,g})\right]} \quad (2.9)$$

The phase shift is determined by the spatial shift of the offset. Formally, when changing ϕ_n by $\Delta\phi$ to $\phi_{n'}$ (so that $\psi_{n,g}$ changes by $-\Delta\phi$ to $\psi_{n',g}$), d changes accordingly by:

$$\Delta d = \frac{\hat{c} [\tau_{tx}(n') + \tau_{rx}(n', g)]}{2 \cos \left[\frac{1}{2} (\phi_{n'} - \psi_{n',g}) \right]} - \frac{\hat{c} [\tau_{tx}(n) + \tau_{rx}(n, g)]}{2 \cos \left[\frac{1}{2} (\phi_n - \psi_{n,g}) \right]} \quad (2.10)$$

To derive the relation between Δd and the phase shift, the spatial oscillation period of the reconstructed echo is required. This can follow the same argumentation as for d (see Fig. 2.3(b)): the spatial period Λ is given by the distance between two isochrones that are separated by one temporal period $1/f_0$:

$$\Lambda(n, g) = \frac{\hat{c}/f_0}{2 \cos \left[\frac{1}{2} (\phi_n - \psi_{n,g}) \right]} \quad (2.11)$$

The fact that Λ varies with varying angles implies that (i) the phase shift varies along the envelope of an echo and (ii) the interference of overlapping echoes partially decorrelates, both resulting in phase noise. To avoid this potential source of errors (and to simplify maths), we assume that the signals are bandpass filtered in a way that the spatial period Λ does not change between n and n' (for one way how this can be achieved, see Materials and Methods) and takes, for example, the value:

$$\Lambda = \frac{\hat{c}/f_0}{2} \quad (2.12)$$

With this convention, the new model for the phase shift is:

$$\begin{aligned} \Delta\Theta(\mathbf{r}', n, n', g) &\simeq \frac{2\pi\Delta d}{\Lambda} \\ &= 2\pi f_0 \left\{ \frac{\tau_{tx}(n') + \tau_{rx}(n', g)}{\cos \left[\frac{1}{2} (\phi_{n'} - \psi_{n',g}) \right]} - \frac{\tau_{tx}(n) + \tau_{rx}(n, g)}{\cos \left[\frac{1}{2} (\phi_n - \psi_{n,g}) \right]} \right\} \end{aligned} \quad (2.13)$$

In comparison to the old model, the new model (Eq. 2.13) not only includes CMA tracking, but also an inverse-cosine law that accounts for the influence of the angles on the echo position offset. Note that the inverse-cosine law in Eq. 2.13 does not depend on the assumption made in Eq. 2.12: even if Λ is allowed to change together with d , a very similar expression is obtained where Λ is replaced by the average value of the Λ for the different angle pairs (maths not shown to avoid distraction). The only disadvantage of allowing Λ to vary could be, as said, an increase in phase noise.

Similar to the old model, the equality in Eq.2.13 only holds if the angle step is chosen so as to avoid phase aliasing. Note that a prediction of the aliasing limit can no more be based on the aberration delays directly in the way this was suggested for the old model, but must take into account the effect of the inverse-cosine law. It is thus ideally based on the complete right-hand side of Eq. 2.13.

2.3 Materials and Methods

2.3.1 Space domain forward and inverse model

The theory section has been formulated with the intention to be general without restriction to specific ways of Tx/Rx beamforming (plane wave, diverging wave, focused line-by-line, etc.). For the experimental study, however, we narrow our focus down to a plane wave Tx approach. In comparison to a diverging wave approach (as, for example, used in [44]), this has the advantage of an improved SNR and that - for a specific Tx setting n - all points inside the tissue (apart from the Tx shadows explained later on) are insonified with an identical Tx angle. In the theory section, we did also not limit ourselves to specific Tx/Rx angle pairs. We only mentioned that the Tx/Rx angle steps need to be sufficiently small so as to avoid phase aliasing. This criterion depends on the specific SoS contrast, and for the phantoms used in our study, it was fulfilled with a 2° angle step (see further below). One could base the SoS reconstruction on phase shift maps acquired with the same angle resolution, but - at the same time - tracking over a maximum possible angle range is desired as this reduces ill-posedness of the SoS reconstruction and thus improves robustness and spatial resolution of the SoS image. The SoS reconstruction would thus have to be based on a large number of phase shift maps resulting in an unnecessarily high computational cost. To reduce the number of phase shift maps and thus the computational cost, we accumulate the phase shift to a coarser angle resolution. Because the final Tx/Rx/mid angles used for SoS reconstruction determine the whole processing chain, we start by outlining these parameters before presenting the different data acquisition and processing steps.

To further simplify the numerics, we choose an equidistantly spaced Tx angle set $\{\phi_n\}$. For CMA tracking, the equidistant spacing of ϕ_n allows choosing a set $\{\gamma_g\}$ of common mid-angles in a way that - for each ϕ_n - the set of Rx angles $\{\psi_{n,g}\}$ can be made identical to the set $\{\phi_n\}$ (this would not be possible with non-equidistant spacing). For clarity, we say that we choose ϕ_n and $\psi_{n,g}$ so that they share the same angle set $\{\Phi_l\}$, i.e. $\phi_n \in \{\Phi_l\}$ and $\psi_{n,g} \in \{\Phi_l\}$. This choice allows to make use of data redundancies as explained further below, but it also simplifies the indexing: given that the Rx angle sets $\psi_{n,g}$ are identical, independent of ϕ_n , it is now practical to index the Rx angle as ψ_m (instead of $\psi_{n,g}$), and corresponding mid-angle as $\gamma_{n,m}$. The reader can convince her/himself that the sets of mid-angles $\{\gamma_{n,m} = 0.5(\phi_n + \psi_m)\}_n$ corresponding to the different ϕ_n are intersecting subsets of one set $\{\gamma_g\}$ of common mid-angles.

For this study, $\{\Phi_l\}$ is $\{-25^\circ, -15^\circ, -5^\circ, 5^\circ, 15^\circ, 25^\circ\}$ for $l = [1 \dots 6]$. Thereby, the 10° step was empirically chosen as a good compromise between computational cost and SoS contrast resolution, and the $\pm 25^\circ$ are limited by grating lobes that become

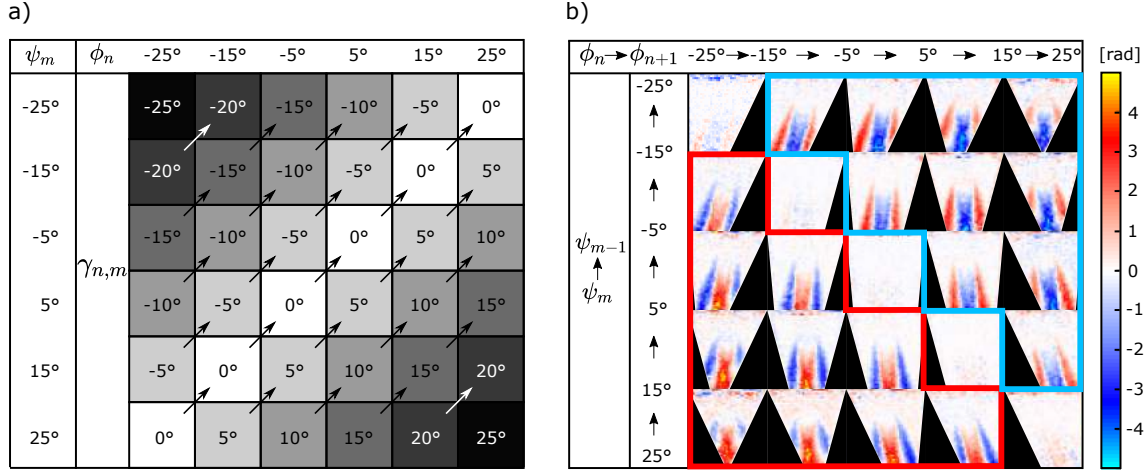


Figure 2.4: a) Combinations of Tx (ϕ_n), Rx (ψ_m) and common mid-angles ($\gamma_{n,m}$) used in this study. Tracking is performed between angle pairs having an identical mid-angle $\gamma_{n,m}$, indicated by arrows pointing along fields having the same gray value. No tracking was performed for $\gamma_{n,m} = \pm 25^\circ$. b) Exemplary phase shift maps from CMA tracking of the simple cylindrical inclusion phantom described in Materials and Methods.

dominant at larger angles (determined by the array probe's element pitch in relation to center frequency). As the goal of the experimental part is to compare the old and the new model, both Tx-only tracking (old model) and CMA tracking (new model) are used in this study. For Tx-only tracking, phase shift is accumulated between successive Tx angles ϕ_n and ϕ_{n+1} , leading to phase shift maps $\Delta\Theta(\mathbf{r}', n)$ for $n = [1 \dots 5]$. For CMA tracking, Fig. 2.4 (a) summarizes the resulting combinations of ϕ_n , ψ_m and $\gamma_{n,m}$. As one can see, the $\gamma_{n,m}$ are all part of a set $\{\gamma_g\}$ equal to $\{-25^\circ:5^\circ:25^\circ\}$. Phase shift is accumulated between angle pairs with common mid-angles $\gamma_{n,m}$, indicated in Fig. 2.4 (a) by arrows pointing along fields having the same gray value. Since only one pair ($\phi_n | \psi_m$) exists for mid angles $\gamma_{n,m} = \pm 25^\circ$, no tracking is performed for these $\gamma_{n,m}$. The tracking procedure results in phase shift maps $\Delta\Theta(\mathbf{r}', n, m)$, for $n, m \in [1 \dots 5]$, between angle pairs ($\phi_n | \psi_m$) and ($\phi_{n+1} | \psi_{m-1}$). Fig. 2.4 (b) exemplarily shows the phase shift maps from CMA tracking of a cylindrical inclusion phantom (see description of phantom later on). These maps are intuitively arranged in a 2D matrix, according to the different angle combinations shown in Fig 2.4 (a). As mentioned above, choosing identical sets of Tx and Rx angles for CMA tracking allows making use of data redundancy: in an ideal case, the crf-mode images resulting from interchangeable ($\phi_n | \psi_m$) angle pairs ($\Phi_l | \Phi_{l'}$) and ($\Phi_{l'} | \Phi_l$) are identical by time reversal symmetry. As a consequence, the phase shift maps between ($\Phi_l | \Phi_{l'}$) and ($\Phi_{l+1} | \Phi_{l'-1}$) and the ones between ($\Phi_l | \Phi_{l'}$) and ($\Phi_{l'-1} | \Phi_{l+1}$) provide redundant data. This is illustrated by the experimental data in Fig 2.4 (b), where the phase shift maps corresponding to interchanged angle pairs, i.e. the maps located symmetrically about the diagonal, are indeed very similar apart from a sign change due to the change in tracking direction. The observed differences in the spatial distribution of the phase shift between redundant maps hint at a residual

asymmetry, which is expected in practice for slight differences in the implementation of Tx and Rx beamforming (as in our study, see later). Residual asymmetry is best observed in the phase shift maps corresponding to identical angle combinations, i.e. the maps in the diagonal of Fig. 2.4 (b): with perfect symmetry, these maps would ideally be zero, and - conversely - they can serve as a measure of symmetry of Tx/Rx beamforming. Due to the redundancy described above, only either the maps below (framed in Fig 2.4 (b) by a red border) or above the diagonal (framed in Fig 2.4 (b) by a blue border) are in principle needed for SoS reconstruction. To reduce the observed deviations from symmetry, however, it is advantageous to generate all possible maps and then average the redundant maps after sign inversion (as it is done in this study).

With a specific set of beamforming parameters (e.g. Tx angle and angular aperture, Rx angle and angular aperture) only part of the imaging plane can be detected due to the limited aperture size of the probe. This leads to areas of missing data ('shadows') towards the lateral edges of the image. In Tx-only tracking (old model) where the full Rx aperture is used, the shadows are determined by the Tx angle alone. In CMA tracking, the combined Tx- and Rx-shadows have to be taken into account. In both cases, when tracking between angles, valid phase shift data is only available in the area where echoes are available before and after the angle step. For CMA tracking (where both Tx and Rx are steered), the combined Tx/Rx shadows are indicated in 2.4 (b) as black areas. As mentioned in the Introduction, the previously proposed FD formulation cannot account for such missing data regions, which complicates a quantitative SoS reconstruction. To avoid this drawback, the forward models in this study were implemented in space domain (SD). For this purpose, the measured spatial distribution of echo phase shift as well as the distribution of the to-be-reconstructed slowness are discretised on the same 2D Cartesian grid, as

$$\Delta\sigma(\mathbf{r}') \rightarrow \Delta\sigma_{j,k} \quad (2.14)$$

$$\Delta\Theta(\mathbf{r}', n) \rightarrow \Delta\Theta_{j,k}(n) \quad (\text{classical tracking}) \quad (2.15)$$

$$\Delta\Theta(\mathbf{r}', n, m) \rightarrow \Delta\Theta_{j,k}(n, m) \quad (\text{CMA tracking}) \quad (2.16)$$

Thereby, the number of nodes (j, k) in x - and z - direction is N_j and N_k , respectively. The nodes sample the chosen dimensions (X, Z) of the rectangular grid with a spatial resolution of $(\Delta x, \Delta z)$. Details are given further below.

The goal of the experimental part is to compare the old and the new model in a phantom study. Thus, both models are implemented as described by Eq. 2.17 and 2.19, respectively, derived from Eq. 2.6 and 2.13. In addition, we want to investigate whether taking into account the echo position offset is required for accurate phase

shift predictions and SoS reconstruction, or whether CMA alone is already sufficient. For this purpose, we also implement an intermediate forward model where only CMA tracking - but not the echo position offset - is taken into account. This intermediate model is henceforth termed 'old CMA model' (Eq. 2.18).

- **Old model**

$$\begin{aligned} \Delta\Theta_{j,k}(n) = & \\ 2\pi f_0 \left[\sum_{j',k'} w_{j,k,j',k'}^{n+1} \Delta\sigma_{j',k'} - \sum_{j',k'} w_{j,k,j',k'}^n \Delta\sigma_{j',k'} \right] & \end{aligned} \quad (2.17)$$

- **Old CMA model**

$$\begin{aligned} \Delta\Theta_{j,k}(n, m) = & \\ 2\pi f_0 \left[\left(\sum_{j',k'} w_{j,k,j',k'}^{n+1} \Delta\sigma_{j',k'} + \sum_{j',k'} w_{j,k,j',k'}^{m-1} \Delta\sigma_{j',k'} \right) \right. & \quad (2.18) \\ \left. - \left(\sum_{j',k'} w_{j,k,j',k'}^n \sigma_{j',k'} + \sum_{j',k'} w_{j,k,j',k'}^m \sigma_{j',k'} \right) \right] & \end{aligned}$$

- **New model**

$$\begin{aligned} \Delta\Theta_{j,k}(n, m) = & \\ \frac{2\pi f_0}{\Omega'} \left(\sum_{j',k'} w_{j,k,j',k'}^{n+1} \Delta\sigma_{j',k'} + \sum_{j',k'} w_{j,k,j',k'}^{m-1} \Delta\sigma_{j',k'} \right) & \quad (2.19) \\ - \frac{2\pi f_0}{\Omega} \left(\sum_{j',k'} w_{j,k,j',k'}^n \Delta\sigma_{j',k'} + \sum_{j',k'} w_{j,k,j',k'}^m \Delta\sigma_{j',k'} \right) & \end{aligned}$$

with,

$$\begin{aligned} \Omega' &= \cos \left[\frac{1}{2} (\phi_{n+1} - \psi_{m-1}) \right] \\ \Omega &= \cos \left[\frac{1}{2} (\phi_n - \psi_m) \right] \end{aligned} \quad (2.20)$$

Thereby the $w_{j,k,j',k'}^l$ are the integration weights defining the discrete line integrals along the US propagation paths defined by the angles Φ_l .

Any of the forward models in Eq. 2.17 to 2.19 can be written in matrix notation, by vectorizing $\Delta\sigma$ and $\Delta\Theta$:

$$\Delta\theta = \mathbf{M}\Delta\sigma \quad (2.21)$$

The system matrix \mathbf{M} also takes into account the missing data regions (shadows) mentioned before, by rows containing zeros that project to zero values in the data vector $\Delta\theta$. Note that, even though all phase shift maps have areas of missing data, these areas are different for different angle steps so that each pixel of the chosen image area is covered by at least one of the phase shift maps. Therefore the SoS can be reconstructed in any pixel of the chosen image area. To reconstruct the values $\Delta\sigma'_{j',k'}$ from the measurements $\Delta\theta_{j,k}$, a Tikhonov pseudo-inverse of \mathbf{M} is used:

$$\Delta\sigma' = \mathbf{M}^{\text{inv}}\Delta\theta \quad (2.22)$$

$$\mathbf{M}^{\text{inv}} = (\mathbf{M}^T\mathbf{M} + \gamma_x\mathbf{D}_x^T\mathbf{D}_x + \gamma_z\mathbf{D}_z^T\mathbf{D}_z)^{\text{inv}}\mathbf{M}^T \quad (2.23)$$

which minimizes the expression

$$C(\Delta\sigma') = \|\Delta\theta - \mathbf{M}\Delta\sigma'\|_2^2 + \|\gamma_x\mathbf{D}_x\Delta\sigma' + \gamma_z\mathbf{D}_z\Delta\sigma'\|_2^2$$

Thereby, \mathbf{D}_x and \mathbf{D}_z are finite difference operators in x and z , respectively, and γ_x and γ_z are regularisation parameters. Regularisation of the spatial gradient of the slowness deviation enforces a smooth slowness profile without imposing a constraint on the mean SoS. The reconstructed SoS $c'_{j',k'}$ is finally recovered from the reconstructed slowness deviation $\Delta\sigma'_{j',k'}$ according to:

$$c'_{j',k'} = \left(\Delta\sigma'_{j',k'} + \frac{1}{\bar{c}} \right)^{-1} \quad (2.24)$$

2.3.2 Data acquisition and beamforming

Fig. 2.5 displays a flow chart that illustrates the various steps that finally lead to the SoS images. We used an L7-4 linear vascular probe (ATL Philips, WA, USA) for pulse-echo signal acquisition. This probe features 128 elements at a 0.29 mm pitch (resulting in 38.4 mm aperture length), and a bandwidth from 4 to 7 MHz with 5 MHz centre frequency. It was connected to a Vantage 64 LE (Verasonics Inc., WA, USA) for data acquisition. This research ultrasound system allows simultaneous ultrasound transmission on 128 elements and parallel digitisation of signals on 64 elements at a time, with real time data transfer via a PCI Express link to a host computer (Intel Core I7-4790 CPU and 16 GB RAM) for further processing. We implemented a dedicated scan sequence for the acquisition of plane wave pulse-echo data. As mentioned in the theory section, Tx focusing is required to achieve

a lateral resolution of the phase shift maps. In this study, this was achieved via coherent plane-wave compounding [46, 47] of plane wave acquisitions with closely spaced Tx angles, for which we chose a 0.5° angle resolution. To use the available angular aperture of the probe (grating lobes were inhibitive outside $\pm 30^\circ$), plane wave data was thus acquired with Tx angles ranging from -27.5° to 27.5° in 0.5° steps. To use all 128 elements on receive, echoes were recorded twice for each Tx angle, once on each of two 64-element sub-arrays, and then combined to a single data frame per angle. The 3D data set resulting from combining the 2D frames of all Tx angles is indicated in Fig. 2.5 (a).

Complex radio frequency (crf)-mode images (see definition in Theory section) were reconstructed off-line for each Tx angle from the raw crf data, using a delay-and-sum (DAS) algorithm:

$$u(x, z, \phi) = \sum_{el} [\alpha(x, z, el) \cdot s(\hat{t}_0(x, z, \phi, el))] \quad (2.25)$$

At each grid node with coordinates (x, z) , the anticipated round-trip times $\hat{t}_0(x, z, \phi, el)$ to each receiving element el were calculated based on the anticipated SoS \hat{c} .

$$\hat{t}_0(x, z, \phi, el) = \frac{1}{\hat{c}} \left[\sin(\phi) (x - \tan(\phi)z) + \cos(\phi)z + \sqrt{(x_{el} - x)^2 + z^2} \right] \quad (2.26)$$

The apodization weights $\alpha(x, z, el)$ define the receive angular aperture within the limits of the aperture length. They were chosen so as to use a receive angular aperture of $\pm 30^\circ$ (limited by the grating lobes outside these angles), by setting them to 1 inside this aperture and to 0 outside. Crf-mode amplitudes were calculated on a rectangular grid, with dimensions 38.4 mm in x (aperture length) by 40 mm in z direction and with spatial resolution $dx = 0.29$ mm in x (pitch) by $dz = 0.037$ mm in z . The DAS step is indicated in Fig. 2.5 (a) ("delay and sum"), where each data frame is transferred to the corresponding crf-mode image.

As mentioned, the target Tx and Rx angle step size chosen for SoS reconstruction was 10° . Given the SoS contrast of the phantoms used in this study, however, the magnitude of the aberration delay change $\Delta\theta$ obtained with this step size resulted in phase shifts above π and thus in phase aliasing when quantifying the phase shift according to Eq. 2.5 and 2.8. By inspecting the phase shift maps, we empirically determined that a tracking angle step size of 2° was just sufficiently small to avoid phase aliasing in all phantoms. Therefore, from the previously reconstructed crf-mode images, we generated images for tracking Tx angles $\phi \in \{-25^\circ : 2^\circ : 25^\circ\}$. For synthetically focused Tx steering along any of these tracking angles ϕ , the 0.5° -

spaced crf-mode images were coherently compounded using a Gaussian weighting function centered at the respective tracking angle with a Gaussian radius of 2.5° . This step is indicated in Fig. 2.5 (a) ("coherent compounding"), where a multitude of crf-images (e.g. for ϕ ranging from -27.5° to -22.5°) is transferred to a single coherently compounded crf ("c-crf") image (e.g. at -25°).

For the old (non-CMA) model, these c-crf images were directly used for tracking. For the CMA tracking, beamformed images are required for different Rx steering angles per each Tx steering angle. This could in principle be implemented via the apodization weights in Eq. 2.25, but we instead used the following approach, which was implemented directly as part of the tracking algorithm: for one tracking Tx angle $\phi \in \{-25^\circ : 2^\circ : 25^\circ\}$ at a time, the full-Rx-aperture c-crf mode image was transformed to a sequence of synthetically Rx-steered images via spatial filtering, for Rx steering angles corresponding to the different mid-angles $\gamma_{n,m} \in \{-20^\circ : 5^\circ : 20^\circ\}$. For the spatial filtering, the respective c-crf-mode image was transferred to k-space by calculating the 2D discrete Fourier transform. In k-space, a specific pair ($\phi | \psi$) of Tx and Rx angles detects a line of the tissue's reflectivity function along the mid-angle $0.5(\phi + \psi)$. Conversely, given the Tx angle ϕ and a target mid-angle $\gamma_{n,m}$, filtering the k-space for a line along $\gamma_{n,m}$ automatically results in the k-space representation of a c-crf-image as if acquired with a tracking Rx angle $\psi = 2\gamma_{n,m} - \phi$. Filtering for a sharply defined $\gamma_{n,m}$ would result in an image as if acquired with zero angular aperture that would provide no spatial resolution perpendicular to $\gamma_{n,m}$. Rather than filtering for only one angle, an angle-dependent Gaussian weighting function was thus used with a radius of $\pm 1.25^\circ$ to synthesise an Rx angular aperture radius of 2.5° . The spatial frequency spectrum was multiplied with a set of such weighting functions centered at the different mid-angles $\gamma_{n,m}$, and then inverse Fourier transformed, to obtain a set of synthetically Rx-filtered c-crf images corresponding to the different $\gamma_{n,m}$. In comparison to a space-domain Rx apodization approach, the k-space approach has the advantage that the Rx beamforming is more similar to the Tx beamforming: k-space filtering is conceptually similar to using "receiving plane waves" for echo detection, and synthesising an Rx angular aperture in k-space is similar to coherent plane-wave compounding in receive, thus improving the Tx/Rx reciprocity in comparison to an element-based Rx beamforming. The spatial frequency filtering step is indicated in Fig. 2.5 (b) ("Rx-filtering"), exemplarily for mid-angle -15° , where an Rx-filtered c-crf image is generated from each full-Rx-aperture c-crf-image that is used for tracking around this mid-angle.

The bandpass to enforce a constant Λ according to Eq. 2.12 was also implemented as part of the spatial frequency filtering: for each $\gamma_{n,m}$, the already Rx-filtered spectrum was multiplied with a k -dependent Gaussian weighting function (where k is the modulus of the spatial frequency vectors) with empirically determined (ψ , $\gamma_{n,m}$)-dependent center point and radius, to enforce a constant center k of the final

filtered spectrum.

As mentioned earlier, it is the beamforming that provides the spatial resolution to CUTE. More precisely, the lower resolution limit is determined by the resolution of the c-crf images (whereas the final resolution is determined also by phase tracking kernel size and SoS regularization). We have performed simulations (not shown) to determine the spatial resolution of the c-crf (Tx-only tracking) and the Rx-filtered c-crf images (CMA tracking), given the chosen beamforming parameters: in Tx-only tracking where the full available Rx angular aperture is used, the resolution limit is determined by the Rx angular aperture to 0.3 mm (FWHM). In CMA tracking, the resolution limit results from the combination of the 2.5° Tx and Rx angular aperture radii, to 2.3 mm (FWHM).

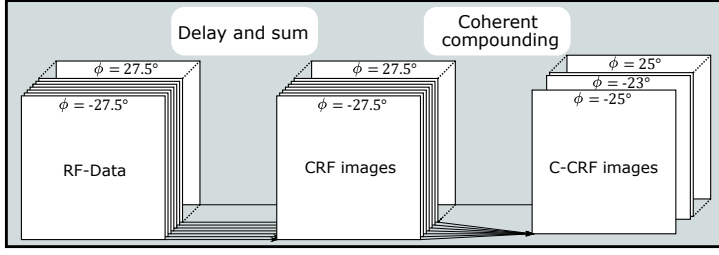
2.3.3 Phase shift tracking

Based on the c-crf images, the echo phase shift was finally determined according to Eq. 2.5 (Tx-only tracking) and Eq. 2.8 (CMA tracking). For Tx-only tracking, phase shift maps were calculated between the full-Rx-aperture c-crf images of successive Tx angles that were spaced by the 2° Tx angle spacing. CMA tracking was performed as follows: looping through successive Tx angles, the Rx filtering was applied to the full-Rx-aperture c-crf image of a respective actual Tx angle at a time. For each $\gamma_{n,m}$, a phase shift map was calculated between the respective previous Rx-filtered c-crf image and the respective actual Rx-filtered c-crf image corresponding to that $\gamma_{n,m}$. The resulting phase shift maps were stored for accumulation (see further below), and the actual Rx-filtered c-crf images were stored to serve as the previous Rx-filtered c-crf images in the next tracking step. For both Tx-only and CMA tracking, the tracking kernel size was chosen $\Delta x = 2$ mm and $\Delta z = 2$ mm. For CMA tracking, this processing step is indicated in Fig. 2.5 (b) ("phase shift tracking"), where two successive Rx-filtered c-crf images (e.g. from angle pair $(-25^\circ | -23^\circ)$ to angle pair $(-5^\circ | -7^\circ)$) are transferred to one phase shift map. Phase shift maps were then summed over successive 2° angle steps to obtain the echo phase shift over 10° steps between Tx angles ϕ_n and ϕ_{n+1} (Tx-only tracking) and Tx/Rx angle pairs $(\phi_n | \psi_m)$ and $(\phi_{n+1} | \psi_{m-1})$ (CMA tracking). For CMA tracking, this is exemplarily shown in Fig. 2.5 (b) ("summation") for mid-angle -15° , where phase shift maps from angle pair $(-25^\circ | -5^\circ)$ to angle pair $(-15^\circ | -15^\circ)$ are summed to a single final phase shift map.

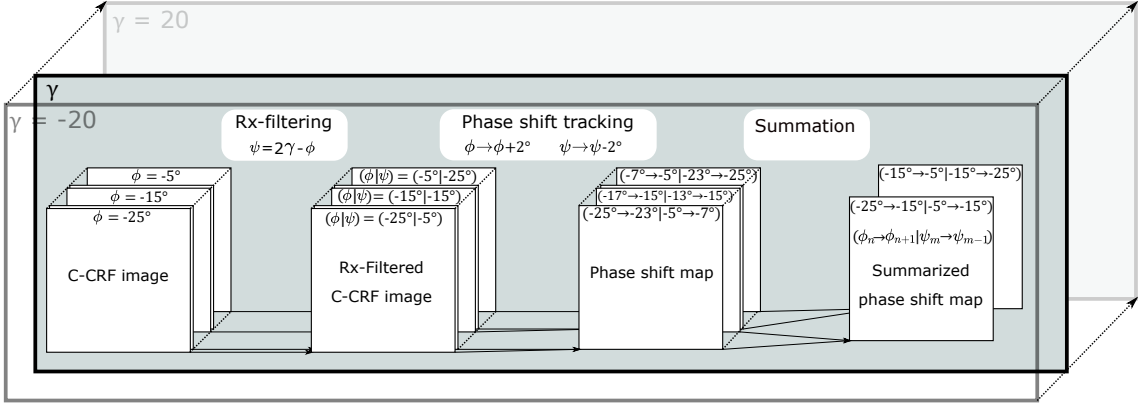
2.3.4 SoS reconstruction

For SoS reconstruction, redundant phase shift maps were averaged ("averaging redundant phase shift maps" in Fig. 2.5 (c)), and the result downsampled onto a Cartesian grid with $N_x = 40$ by $N_z = 40$ grid nodes covering $X = 38.4$ mm by

a) Data acquisition and beamforming



b) Phase shift tracking



c) SoS reconstruction

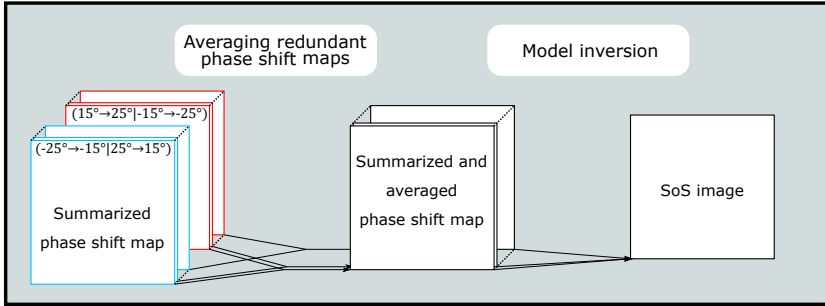


Figure 2.5: Flow chart describing the working principle of CUTE, divided into three main parts.

$Z = 40$ mm with a resolution of $\Delta x = 0.96$ mm by $\Delta z = 1$ mm. The forward models according to Eq. 2.21 and 2.22 were correspondingly formulated for the same grid resolution, resulting in a system matrix with $(40 \cdot 40)$ by $(40 \cdot 40)$ elements per 10° angle step, totalling 8000 by 1600 elements for Tx-only tracking (5 Tx angle steps) and 16000 by 1600 elements for CMA tracking (10 combined Tx/Rx angle steps). For line integration, bi-linear interpolation weights were chosen.

The regularization parameters γ_x and γ_z are subject to a trade-off between reducing artefacts (by enforcing a smooth slowness profile) and maximising spatial resolution. For this study, they were chosen so as to clearly distinguish the different phantom compartments (Old model: $\gamma_x = 2.33$, $\gamma_z = 0.23$; old CMA model: $\gamma_x = 5.68$, $\gamma_z = 0.11$; New model: $\gamma_x = 9.09$, $\gamma_z = 0.18$).

The pseudo-inverses were pre-calculated according to eq. 2.23 and stored. The pre-calculated pseudo-inverses were then applied to the vectorized phase shift data for reconstructing the slowness distribution, and – in turn – the SoS. This step (appli-

cation of pseudo-inverse, calculation of SoS from slowness) is indicated in Fig. 2.5 (c), "model inversion". With the chosen grid resolution, the matrix multiplication takes a fraction of a second (e.g. 0.04 s on the used Intel Core I7-4790 CPU and 16 GB RAM) when implemented in Matlab[®].

2.3.5 Phantom design and materials

For this study, two different sets of phantoms were designed and investigated. The first set of phantoms was designed with the goal to represent particular geometries of the anatomical structure of the abdominal wall and liver, since liver imaging is one of our envisaged clinical applications. To mimic focal lesions (as e.g. for the diagnosis of breast cancer) the phantoms of the second set contain cylindrical inclusions. The geometries of the spatial distribution of SoS in the different phantoms are shown in Fig. 2.6. Note that, in the following, even though the absolute SoS values of the different phantom compartments may deviate from real tissue depending on literature references, we have taken care to chose realistic SoS contrasts between the different compartments.

- Liver mimicking phantoms

- a) *Two-layer phantom*: This phantom contained two horizontal (parallel to x) layers, mimicking a single fat layer (F1: 1420 ms^{-1}) on top of liver tissue (L: 1555 ms^{-1}). The special feature of this type is the complete absence of lateral SoS variations but a pronounced axial variation. This geometry occurs when imaging the liver sagittally through the linea alba.
- b) *Four-layer phantom*: In comparison to the two-layer phantom, two additional layers were added, mimicking the rectus abdominis muscle (M: 1555 ms^{-1}) and the post-peritoneal fat layer (F2: 1555 ms^{-1}), representative e.g. for a sagittal section lateral to the linea alba. The purpose of this phantom was to compare the different models in a layer structure with axial variations near the axial resolution limit.
- c) *Laterally varying muscle diameter (LVMD) phantom*: In contrast to the four-layer phantom, the rectus abdominis (M: 1555 ms^{-1}) layer deviates in this phantom from the parallel layer structure and consists of two wedge-shaped areas, as when imaging the liver in a transverse section through the linea alba. This phantom thus provides a moderate lateral variation of SoS in addition to the axial variation.

- Cylindrical inclusion phantoms

- d) *Simple inclusion phantom*: This phantom was composed of a uniform background compartment (C1: 1540 ms^{-1}) containing a cylindrical inclusion (I: 1570 ms^{-1}).
- e) *Two-layer phantom with inclusion*: In comparison to the simple inclusion phantom, the background compartment of this phantom contained an additional layer (C2: 1570 ms^{-1}) below the inclusion.

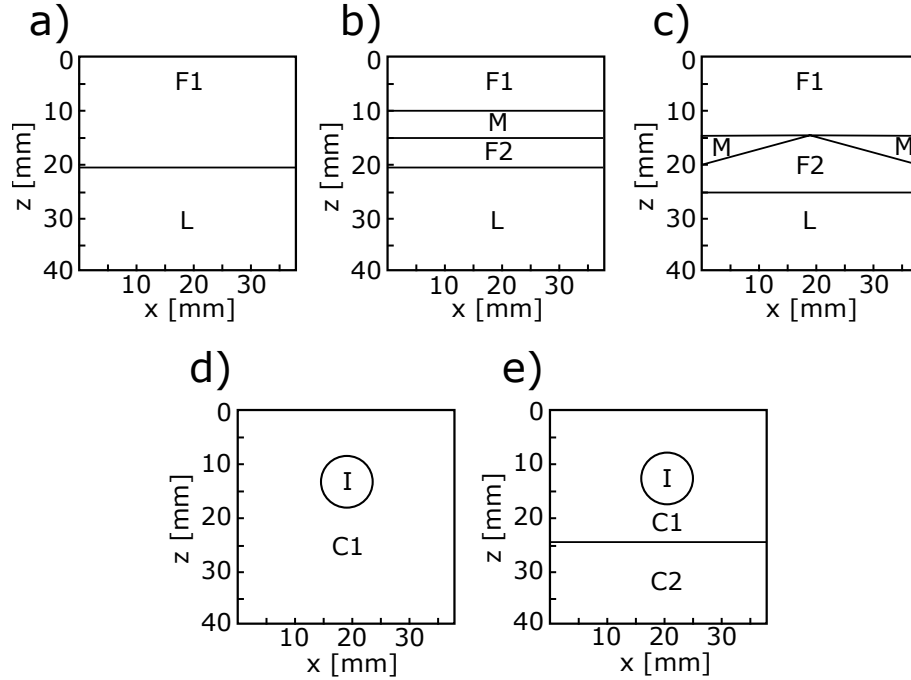


Figure 2.6: Sketch of the phantom geometries. The reference SoS were determined using a through transmission time-of-flight set-up with an accuracy of $\pm 5 \text{ ms}^{-1}$, to F1: 1420 ms^{-1} , F2: 1420 ms^{-1} , M: 1555 ms^{-1} , L: 1555 ms^{-1} , C1: 1540 ms^{-1} , C2: 1570 ms^{-1} , I: 1570 ms^{-1}

The phantom components were produced based on porcine gelatine (Geistlich Spezial Gelatine, health and life AG, Switzerland). In a first step, gelatine was dissolved in 75°C H_2O with various weight contents for the different phantom compartments (C1: 15 wt%, M, L: 20 wt%, C2, I: 25 wt%). To provide a uniform diffuse echogenicity, various weight contents of cellulose (Sigmacell Cellulose Type 20, Sigma Aldrich, Switzerland) were added (C1: 1 wt%, M,L, C2: 2 wt%, I: 0.5 wt%). The resulting SoS of the different gelatin solutions after gelling were: C1: 1540 ms^{-1} , M, L: 1555 ms^{-1} , C2, I: 1570 ms^{-1} . For the fat mimicking compartments (F1, F2) in the liver mimicking phantoms, oil-in-gelatin emulsions were produced [48–51]. For this purpose, medium-chain triglycerides oil (Ceres-MCT Oil, Puravita, Switzerland) (SoS = 1350 ms^{-1}) was slowly blended under continuous stirring into the still hot aqueous gelatine base solution (20 wt% gelatine and 2 wt% cellulose) using a Visco Jet cone-stirrer (VISCO JET Agitation Systems, Germany). During this process, small oil droplets were formed and captured via hydrophobic interaction by the lipophilic

part of the gelatine strings. After cooling the emulsion, the oil droplets were trapped within the gelatine matrix. The resulting SoS was determined by the emulsion's relative MCT oil weight content, in this study 0.65 wt%, resulting in a SoS of 1420 ms⁻¹. The mentioned SoS values were determined using a through-transmission time-of-flight set-up (accuracy ± 5 ms⁻¹) and will serve in the following as reference for comparing the accuracy of phase shift predictions and reconstructed SoS values.

2.4 Results

2.4.1 Echo phase shift

Similar to what has already been done for the old model (see. Fig. 2.1), Fig. 2.7 shows profiles of the measured phase shifts and of the predictions made by the old CMA (Eq. 2.18) and the new model (Eq. 2.19) in the same two phantoms, for the Tx-Rx tracking combination of $\phi_n \rightarrow \phi_{n+1} = 5^\circ \rightarrow 15^\circ$ and $\psi_m \rightarrow \psi_{m-1} = -5^\circ \rightarrow -15^\circ$. In case of the four-layer phantom, the axial profile at $x = 19.2$ mm is shown. For the simple cylindrical inclusion phantom, the lateral profile at $z = 30$ mm is shown. For a more quantitative comparison, table 2.1 summarizes the root-mean-square error (RMSE) of the complete phase shift datasets for all models according to:

$$\text{RMSE}_{\Delta\Theta} = \left(\frac{\sum_{n=1}^5 \sum_{m=1}^5 \sum_{j=1, k=1}^{N_j, N_k} [\Delta\Theta_{j,k}^*(n, m) - \Delta\Theta_{j,k}(n, m)]^2}{N_j \cdot N_k \cdot 5 \cdot 5} \right)^{-1/2} \quad (2.27)$$

where $\Delta\Theta^*$ denotes the measured phase shift and $\Delta\Theta$ the phase shift predicted by the forward model at grid node (j, k) for all combinations of Tx/Rx pairs $(\phi_n | \psi_m)$ that are outlined in Fig. 2.4(b).

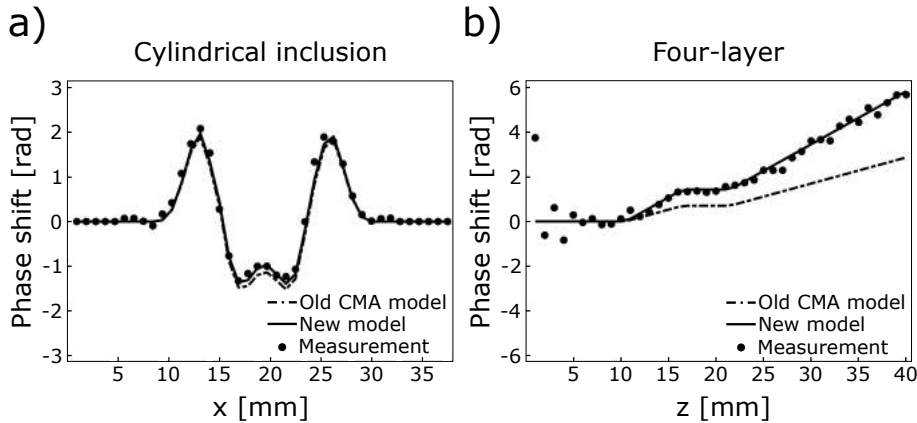


Figure 2.7: Comparison of the measured phase shift to the predictions made by the old CMA model and by the new model, for Tx-Rx angle steps of $\phi_n \rightarrow \phi_{n+1} = 5^\circ \rightarrow 15^\circ$ and $\psi_m \rightarrow \psi_{m-1} = -5^\circ \rightarrow -15^\circ$, around the mid-angle $\gamma_{n,m} = 0^\circ$. (a) Lateral profile ($z = 30$ mm) of the simple cylindrical inclusion phantom. (b) Axial profile ($x = 19.2$ mm) of the four-layer phantom.

	RMSE $_{\Delta\Theta}$ [rad]	
	Four-layer	Cylindrical inclusion
Old Model	0.738	0.423
CMA Model	0.852	0.339
New Model	0.384	0.320

Table 2.1: RMSE $_{\Delta\Theta}$ of the measure phase shift in comparison to the different forward models in two exemplary phantoms.

In case of the simple cylindrical inclusion phantom (Fig. 2.7 a), the phase shift that is predicted by the old CMA model matches the measured data already well. Note especially that it not only predicts the correct phase shift amplitude but also the spatial profile, whereas the latter was wrongly predicted with the old model (compare to Fig. 2.1). The improved accuracy is confirmed by the RMSE $_{\Delta\Theta}$. These observations indicate that the wrong prediction of the profile by the old model was due to an implicit Rx-angle dependence of the real data that was not accounted for. By explicitly modelling this dependence in the CMA approach, a much more accurate prediction was obtained.

In comparison to the old CMA model, the new model gives only a slight improvement for the cylindrical inclusion (seen both in Fig. 2.7 and in the RMSE $_{\Delta\Theta}$). This changes, however, completely for the four-layer phantom (Fig. 2.7 b): here the old CMA model underestimates the measured phase shift by a factor two similar to what was already observed for the old model in Fig. 2.1, demonstrating that the CMA approach alone cannot describe the reality well. When, however, accounting also for the echo position offset (new model), the predicted phase shift matches the measured data very well. The RMSE $_{\Delta\Theta}$ again confirms that the new model describes the reality best.

Note that, in both phantoms, the differences in the RMSE $_{\Delta\Theta}$ between the models appear less extreme than one could expect based on the comparison of the phase shift profiles: the RMSE $_{\Delta\Theta}$ is reduced by roughly a factor two for the four-layer phantom and 1.3 for the cylindrical inclusion phantom between the old and the new model, whereas the profiles show perfect agreement for the new model. The reason is following: profiles are shown for angle combinations where the phase shift magnitude is large to provide a good SNR. For many other angle combinations, the phase shift magnitude is smaller, and over all the RMSE $_{\Delta\Theta}$ is to a large part determined by phase noise. It therefore also comes at no surprise that the RMSE $_{\Delta\Theta}$ of the new model are very similar for both phantoms, as they represent the phase noise level rather than an actual deviation between prediction and experiment.

Fig. 2.7 together with the RMSE $_{\Delta\Theta}$ thus demonstrate that both features, the CMA approach and the modelling of the echo position error, are a minimum requirement for an accurate forward model and thus for achieving quantitative SoS imaging in CUTE.

2.4.2 SoS images

The comparison between the measured phase shifts and the predictions made by the forward models on its own already clearly falsifies the general applicability of the old and of the old CMA model, since both fail in predicting the correct phase shift in the four-layer phantom.

In a next step, we want to investigate whether the two proposed changes to the CUTE forward model together are not only a minimum requirement, but also sufficient for achieving quantitative SoS results. This investigation has to be performed based on SoS images as opposed to phase shift predictions for following reason: subtle differences in phase shift predictions of a forward model can unpredictably affect the reconstructed SoS, given the ill-posed nature of the inverse problem. In case of focal lesions, for example, one might argue that the CMA approach alone is sufficiently accurate, but we will see that this is not true for the SoS images. Similarly, small errors in the proposed new model could lead to unexpected large errors in the reconstructed SoS that obliterate the usefulness of the new model.

Therefore, to further compare the different models and evaluate their performance, the reconstructed SoS images are shown for all five phantoms in Fig. 2.8 to Fig. 2.12. The color scale was chosen in a trade-off between covering a large SoS range and allowing to perceive small SoS variations (e.g artifacts). As a consequence, image regions in which the SoS deviates by $\gtrsim 70 \text{ ms}^{-1}$ from the true upper and lower SoS of the liver mimicking phantom appear saturated. To allow a fair comparison between the images of the two phantom sets (e.g. the level of artifacts), the same color scale was also used for the cylindrical inclusion phantoms.

Note that SoS reconstruction results are shown for various different choices of the *a priori* SoS \hat{c} . As described in Materials and Methods, \hat{c} is used for the reconstruction of the crf-mode images. In an ideal scenario, the deviation of the actual SoS from this value results in an echo phase shift and a reconstructed slowness deviation that – together with \hat{c} – finally leads to the correct SoS independent of \hat{c} according to Eq. 3.4. In reality, however, errors can be introduced via the influence of \hat{c} on the beamforming (i.e. distortions of the spatial pulse shape as well as propagation angle) and/or via errors of the SoS reconstruction model. While being a potential source of errors, \hat{c} is also a parameter that would be conveniently accessible to manipulation by a radiologist. For this reason, we examine the sensitivity of the SoS results towards variations of \hat{c} , by comparing results for different \hat{c} covering a range of 1420 ms^{-1} to 1555 ms^{-1} for the liver mimicking phantoms and 1480 ms^{-1} to 1570 ms^{-1} for the inclusion phantoms.

To aid a quantitative evaluation and the comparison of the different models, we provide several metrics of the SoS values: the rightmost columns of Fig. 2.8 - 2.12 show the mean and standard deviation of the reconstructed SoS within each

individual compartment over the full respective compartment area. In addition, Fig. 2.13 shows the root-mean-square errors (RMSE) of all phantoms according to:

$$\text{RMSE} = \sqrt{\frac{\sum_{j,k} (c_{j,k}' - c_{j,k})^2}{N_j \cdot N_k}} \quad (2.28)$$

where $c'_{j,k}$ is the reconstructed SoS and $c_{j,k}$ the ground-truth SoS at the grid nodes (j, k) . Note that, independent of the phantom geometry, the *a priori* SoS \hat{c} or the forward model, all SoS images show artifacts in the top few millimetres (see Fig. 2.8 to Fig. 2.12). These artifacts originate from erroneous values (outliers) in the top few millimetres of the phase shift maps (see e.g Fig. 2.1, 2.4 and 2.7). We hypothesize that these errors result from element cross-talk during the plane wave transmission: whenever an element is activated, all other elements instantaneously detect an electric interference. The larger the Tx angle, the more the interferences from all transmitting elements are stretched over time and obscure superficial echoes. As cross-talk related artifacts are not related to the forward model, the top 5 mm of the SoS images were excluded from the calculation of the SoS metrics.

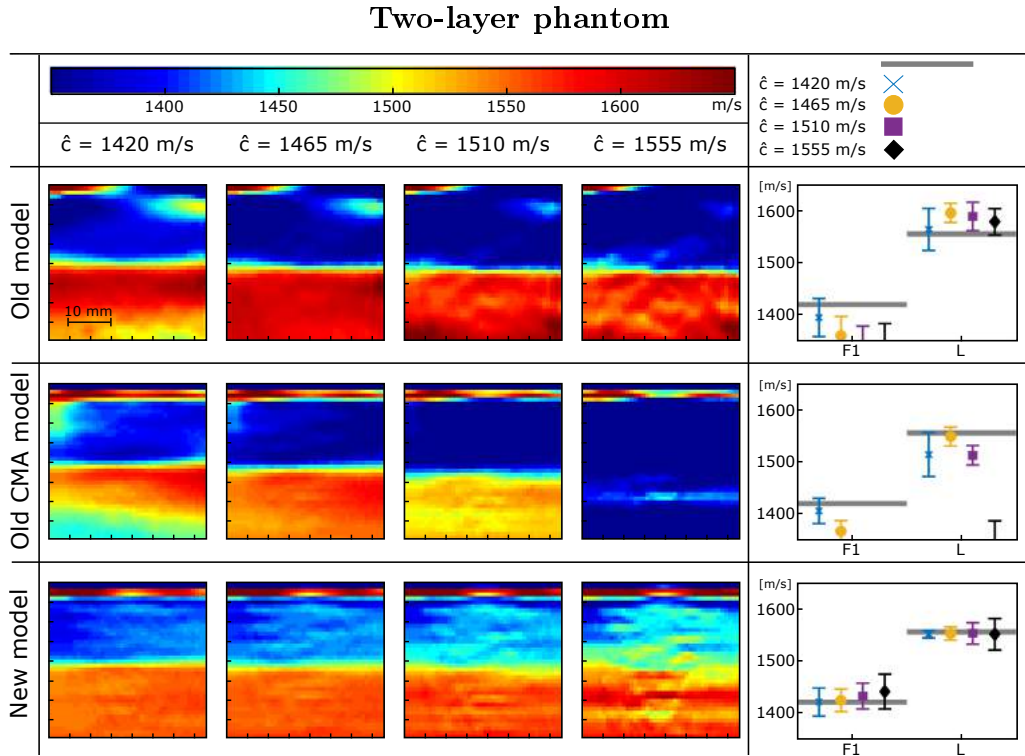


Figure 2.8: SoS images of the two-layer phantom mimicking the liver (SoS = 1555 m/s) and a single fat layer (SoS = 1420 m/s) (from posterior to anterior). The SoS images were reconstructed based on the different forward models (rows) and for different *a priori* SoS values \hat{c} (columns). The SoS images are sampled on 40 (x) by 40 (z) grid nodes covering 38.4 mm (x) by 40 mm (z).

Four-layer phantom

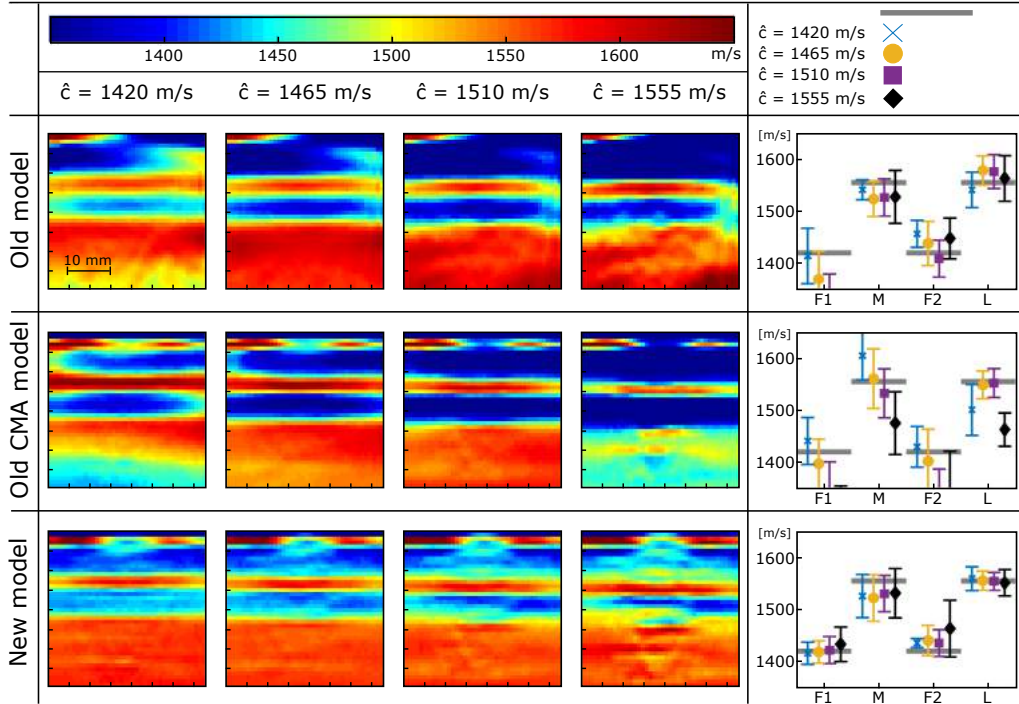


Figure 2.9: SoS images of the four-layer phantom mimicking the liver (SoS = 1555 m/s), a post-peritoneal layer (SoS = 1420 m/s), the rectus abdominis (SoS = 1555 m/s) and the subcutaneous fat layer (SoS = 1420 m/s) (from posterior to anterior). The SoS images were reconstructed based on the different forward models (rows) and for different *a priori* SoS values \hat{c} (columns). The SoS images are sampled on 40 (x) by 40 (z) grid nodes covering 38.4 mm (x) by 40 mm (z).

Old model

For intermediate \hat{c} , the old model leads to SoS images of the two- and four-layer phantoms (see Fig. 2.8 to 2.9 - top rows) that seem reasonable in terms of a uniform spatial distribution of SoS in the liver-mimicking compartment L. At the lower limit of the chosen range of \hat{c} , however, the SoS inside L becomes less uniform, and the contrast between the compartments varies with \hat{c} . In spite of these shortcomings, one could argue, the images of these two phantoms look quite reasonable. This changes, however, dramatically for the LVDM phantom (Fig. 2.10 - top row): here the SoS in compartments L is substantially overestimated, and heavily non-uniform. The SoS in compartments M is underestimated, and the spatial distribution wrongly reconstructed, i.e. an artifactual high-SoS area appears between the wedge-shaped parts of M. Note that, in all phantoms, low spatial frequency variations of SoS appear in at least part of the image area. These variations are most clearly seen in the SoS images of the cylindrical inclusion phantoms (Fig. 2.11 to 2.12 - top rows), where they make it difficult – if not impossible – to distinguish the cylindrical inclusions from the background, and impossible to perceive the absence or presence of compartment C2.

LVMD phantom

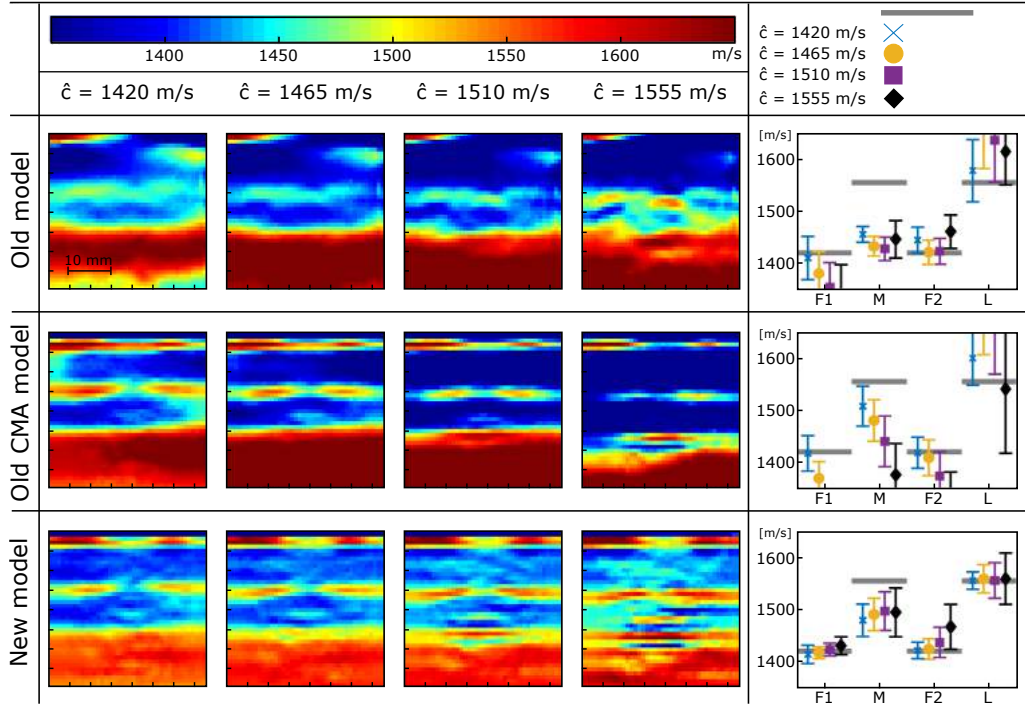


Figure 2.10: SoS images of the LVMD phantom mimicking the liver (SoS = 1555 m/s) covered by a triangular postperitoneal fat layer (SoS = 1420 m/s), the rectus abdominis (SoS = 1555 m/s) and the subcutaneous fat layer (SoS = 1420 m/s) (from posterior to anterior). The SoS images were reconstructed based on the different forward models (rows) and for different *a priori* SoS values \hat{c} (columns). The SoS images are sampled on 40 (x) by 40 (z) grid nodes covering 38.4 mm (x) by 40 mm (z).

Old CMA model

In all phantoms (see Fig. 2.8 to 2.12 - middle rows), the old CMA model leads to even stronger low spatial frequency variations and a stronger dependence of the different compartments' SoS on \hat{c} . On the upside, it is better at reconstructing the true spatial profile of the SoS of the compartments M in the LVMD phantom. In the cylindrical inclusion phantoms (Fig. 2.11 to 2.12 - middle rows), the low spatial frequency variations are more symmetric than with the old model, and less dependent on \hat{c} , allowing a better perceptibility of the inclusions. Apart from that, the presence/absence of compartment C2 can still not be perceived well: due to the gradient of SoS in supposedly uniform areas, it is difficult to judge whether the apparent boundary at the depth of the surface of compartment C2 is an actual boundary or simply an artifact of the color scale.

New model

In comparison to the old and the old CMA model, the new model leads to strongly improved SoS images in the liver phantoms (Fig. 2.8 to 2.10 - bottom rows). Apart from some high-frequency artifacts for certain values of \hat{c} (on which we comment further below) they show a much more uniform distribution of SoS in the different

compartments, and this largely independent of \hat{c} . As already with the old CMA model, the compartments M in the LVMD phantom are well delineated. The average SoS values agree well with the references, this again independent of \hat{c} . The only exception is seen in the M and F2 compartments of the four-layer and the LVMD phantom, where the SoS is biased most probably due to the partial volume effect. In all liver phantoms, the uniformity of the L compartment and the resolution of its surface is best for \hat{c} near the SoS of the overlaying F layers. With increasing \hat{c} , high spatial frequency artifacts appear and gradually increase at and inside the L compartment, and the resolution of the surface becomes worse. We suggest that these findings are caused by a decreasing beamforming quality at the depth of the L compartment – resulting in phase shift noise – due to the increasing deviation of the \hat{c} from the actual SoS of the top compartments. Note that the high spatial frequency artifacts lead to fluctuations of SoS around a reasonable constant value rather than skewing the spatial profile of SoS within uniform layers.

Also in the cylindrical inclusion phantoms (Fig. 2.11 to 2.12 - bottom rows), the new model leads to SoS images that show the expected uniform distribution inside the different as well as the expected quantitative SoS values nearly independent of \hat{c} . The cylindrical inclusion as well as the absence or presence of the C2 compartment can now be clearly identified. High spatial frequency artifacts are seen to a lesser extent than in the liver phantoms. This can be explained by the fact that – on one hand – the chosen range of \hat{c} is smaller than for the liver phantoms, and – on the other hand – the SoS of the first (C1) compartment is far from both extremes of the \hat{c} range, so that beamforming is less affected for any of the \hat{c} values. Note that, even though the old CMA model and the new model led to nearly identical phase shift profiles in Fig. 2.7, the resulting SoS images are very different. This demonstrates how – due to the ill-posedness of the inverse problem – small differences in phase shift predictions can cause unforeseen large differences in the final SoS images.

The superiority of the new model over the old and the old CMA model is further confirmed by the RMSE that are shown in Fig. 2.13: whereas the RMSE strongly depends on \hat{c} with the old and the old CMA model, it is much more stable with the new model, and in all phantoms and for all \hat{c} , the new model clearly outperforms the old as well as the old CMA model.

2.5 Discussion and Conclusion

Departing from the observation of wrong predictions of experimental echo phase shift by the old model, we proposed in this study two fundamental changes to the CUTE methodology: the CMA approach with an explicit formulation of the dependence of echo phase shift on both Tx and Rx angle, and the explicit consideration of

Simple inclusion phantom

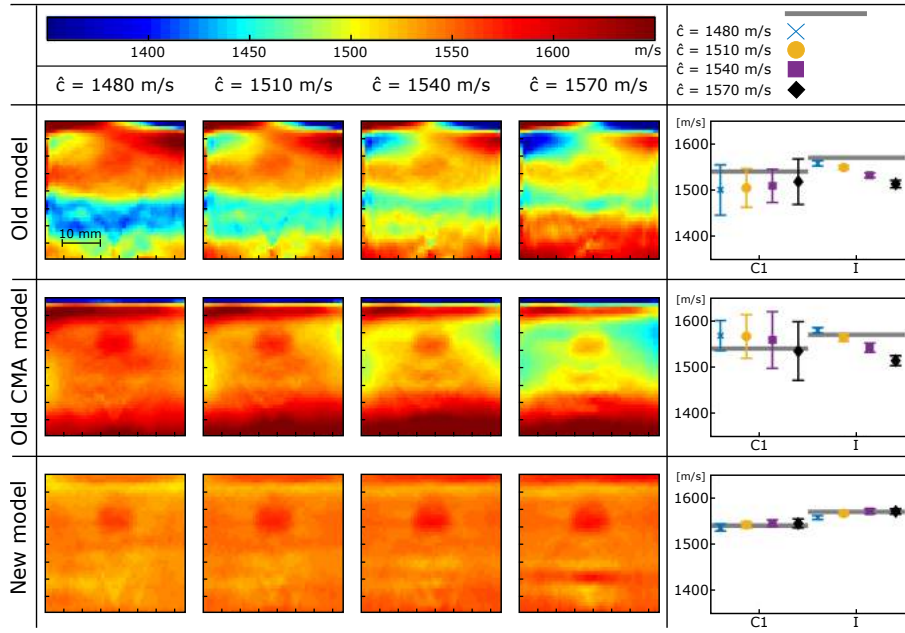


Figure 2.11: SoS images of the simple cylindrical inclusion phantom. The SoS images were reconstructed based on the different forward models (rows) and for different *a priori* SoS values \hat{c} (columns). The SoS images are sampled on 40 (x) by 40 (z) grid nodes covering 38.4 mm (x) by 40 mm (z).

Two-layer phantom with with cylindrical inclusion

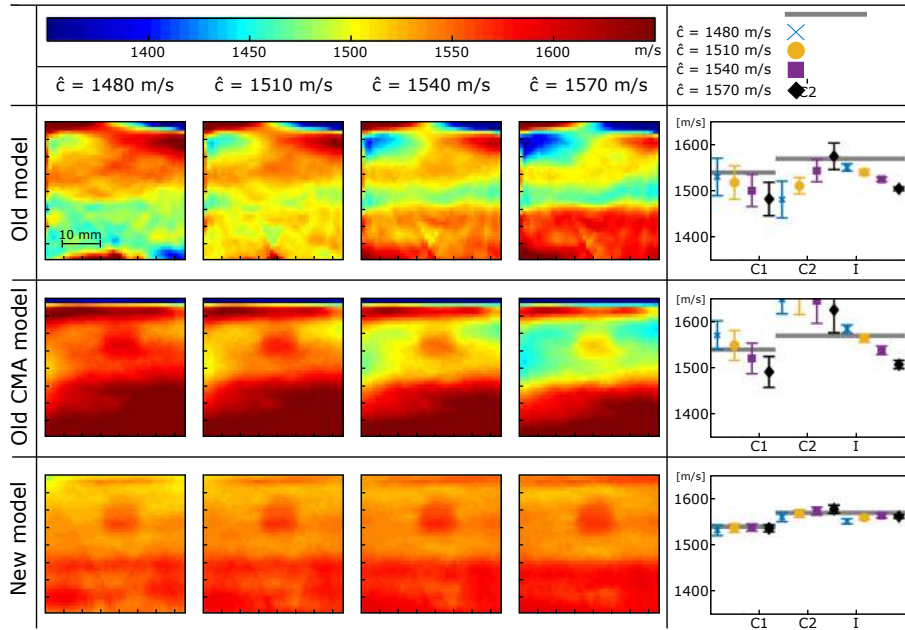


Figure 2.12: SoS images of the two-layer cylindrical inclusion phantom. The SoS images were reconstructed based on the different forward models (rows) and for different *a priori* SoS values \hat{c} (columns). The SoS images are sampled on 40 (x) by 40 (z) grid nodes covering 38.4 mm (x) by 40 mm (z).

Root-mean-square errors

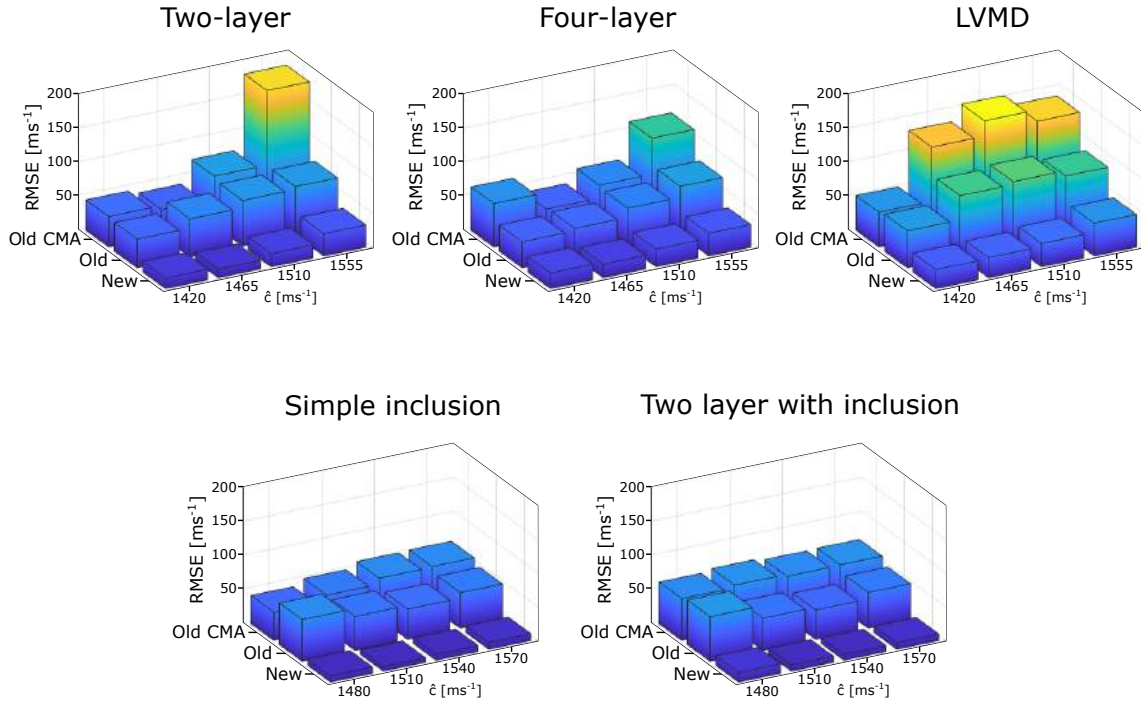


Figure 2.13: Root-mean-square errors (RMSE) of all five phantoms, calculated according to Eq. 2.28. For each phantom, the RMSE of the old CMA, the old and the new model at the various *a priori* SoS \hat{c} are shown.

the echo position offset in the forward model. The comparison of the measured and predicted phase shifts clearly demonstrates that only the new model leads to remarkable accuracy in all investigated phantom geometries. Both novel features together are thus a necessary prerequisite for an accurate forward model.

Due to the ill-posed nature of the inverse problem, however, it is difficult to predict how the differences in the forward models affect the final SoS images. Consequently, SoS images are needed to determine whether the new model is not only a necessary prerequisite for quantitative imaging but also – within the approximations made – a sufficient one. The SoS images have shown that the new model outperforms the old and old CMA model in all phantoms in view of RMSE, level of artifacts as well as the stability against variations of the *a priori* assumed SoS \hat{c} . A slight positive dependence of reconstructed SoS on \hat{c} is observed in all phantoms, which may be explained by an imperfect calibration of the beamforming or other factors not accounted for, such as the curvature in elevation of the probe’s acoustic lens, but – given the small magnitude of the \hat{c} -influence compared to the standard deviations – this was considered beyond the scope of this study.

Given the ill-posed nature of the inverse problem, one may doubt whether the hyperparameters involved in the model implementations can have a similarly unpredictable influence as differences in phase shift predictions, and whether one may thus want to take conclusions based on SoS images with care. To avoid – as far as possi-

ble – the influence of hyperparameters on the results, we have explicitly restrained from optimizing hyperparameters for the different models separately but have chosen identical parameters wherever possible. More specifically, we have chosen: identical Tx angles and Tx angular apertures in all models, Rx angles and angular apertures identical to Tx angles and angular apertures in the CMA-based models, and an Rx angular aperture in the old model that is (nearly) identical to the Rx angle range in the CMA-based models. Only the regularisation parameters were chosen differently. They were, however, not optimized for the different models independently, but with the goal to provide SoS images of the chosen phantoms that are – to the eye – similar in terms of axial resolution for a fair comparison of artifact level. For this reason, we argue, the SoS images provide a fair comparison of model performance, and we conclude that the new model is not only the only one capable of correctly predicting echo phase shift among the investigated phantom geometries, but it is even able to correctly predict the small nuances that are needed to obtain a good SoS image, and this even given the limitations of the quite coarse approximations made (i.e. straight-ray propagation, negligible wave front distortion ...).

A key assumption made in this study was the straight-ray approximation of US propagation, neglecting diffraction and refraction. Given the lateral resolution of the final SoS image (few mm) in relation to the wavelength (0.2 mm at 5 MHz), diffraction will have played a minor role. With the realistically high SoS contrast between the liver-mimicking phantoms' layers (135 m/s), one would expect that refraction had an important influence. In horizontally layered media, the effect of refraction is mainly a change of propagation angle which can bias the phase shift measurements. Based on the fact that correct quantitative results were obtained using the new model, one can conclude that such biases were negligible even for the LVMD phantom with the continuously varying diameter of the wedge-shaped compartments M. More influence of refraction would be expected for the cylindrical inclusion phantoms, where the inclusion poses a abrupt lateral variation of SoS. Our results suggest that also here, the straight-ray approximation was reasonable in the sense that correct quantitative results could be obtained, but given a substantially smaller SoS contrast (30 m/s) than in the LVMD phantom (135 m/s). Independent experiments have shown that – for the same size of the inclusion – an increasing SoS contrast leads to an increasing level of artifacts below the inclusion, as well as to an underestimation of the SoS inside the inclusion. Such artifacts can on one hand be explained by an increasingly non-linear relation between slowness distribution and echo phase shift due to deviations from straight-ray propagation, but also by beamforming errors due to caustics (i.e. US propagating towards and from the same reflectors along multiple intersecting paths). We foresee that refraction can be compensated for, e.g. employing a more accurate forward model of sound propagation. Note that the key features of the new model, i.e. the CMA approach and

the inverse-cosine law describing the relation between aberration delay and echo phase shift, are independent of the straight-ray approximation of how aberration delay is related to SoS (the latter was only proposed to enable real-time imaging). We therefore envisage that the new model of how aberration delays are reflected in echo phase shift is more generally applicable, e.g. with a bent-ray model of sound propagation. The influence of refraction on the final SoS image as well as potential remedies is an interesting topic, it is, however, beyond the scope of this study.

Another fundamental assumption was that of sharply defined Tx/Rx angles, but finite angular apertures are needed and were used in the experiments to enable a laterally resolved echo phase shift measurement (and thus SoS image). One may argue that the round-trip times of echoes thus correspond to average slowness integrals over wedge-shaped areas rather than along thin lines. Wave field simulations (not shown) indicate, however, that the angular aperture radius used for Tx/Rx focusing (2.5°) together with the wavelength (0.2 mm at 5 MHz) result in a collimated beam rather than a focused one, with a roughly constant beam diameter of 2.5 mm. Within this resolution, the rays can therefore be approximated as lines. The good accuracy of our results demonstrates that the simplification to line integrals had only minor influence. The influence of Tx and Rx angular apertures on the SoS results is an interesting topic, but was beyond the scope of this study.

The focus of the present study was to validate the new model. This was done in phantom experiments, and – so far – we did not attempt to investigate the clinical accuracy of CUTE. As a preliminary confirmation of the phantom results in an *in-vivo* case, however, Fig. 2.14 shows the B-mode and SoS images reconstructed with the old and the new model, of a healthy volunteer’s liver (male, age 40, in compliance with the ethical principles of the Declaration of Helsinki 2018). As opposed to the old model, the new model reconstructs a spatial distribution of SoS that correctly delineates the spatial distribution of the different tissue types, and shows the expected uniform distribution of SoS inside the liver. Moreover, the reconstructed mean SoS of the liver (1564 ± 4 m/s) is reasonable for healthy liver tissue [52], making the new model a promising step towards quantitative hepatic imaging. Imbault et al. [25] reported that the average SoS of the liver of healthy patients is ≈ 1570 m/s. For patients having steatosis of grade 1 (according to the Brunt scale), the average SoS decreases by about 40 m/s. Thus, CUTE (with the proposed new model) has potential for a quantitative diagnosis of fatty liver disease. To allow real time SoS imaging, the regularized pseudo-inverse matrix according to Eq. 2.23 can be pre-calculated and stored in a lookup table as described in the Materials and Methods section. As an example: applying the pre-calculated pseudo-inverse to the phase shift data takes only 0.04 s when implemented in Matlab[®] on the system with Intel Core I7-4790 CPU and 16 GB RAM. The bottle neck is the data transfer and beamforming (0.6 s when implemented with the Verasonics

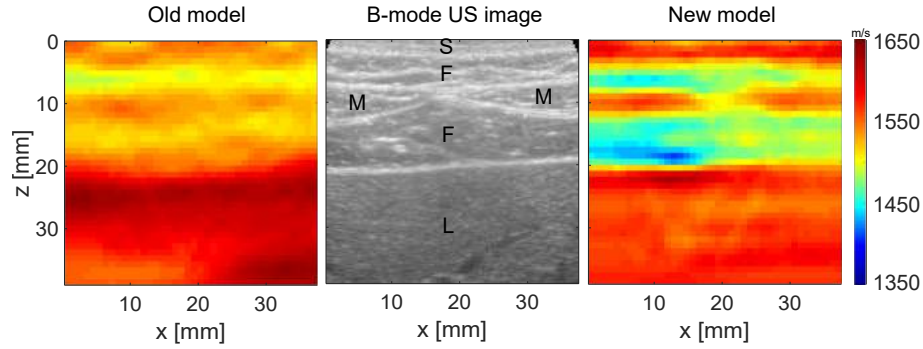


Figure 2.14: Side-by-side display of conventional B-mode US of a healthy volunteer’s abdominal wall with subjacent liver tissue (S: skin, F: fat, M: rectus abdominis muscle, L: liver parenchyma) and SoS images reconstructed with the old and the new model. In the new model, the SoS values of different tissues are well distinguished.

Vantage 64 LE and on the same PC, using the Verasonics DAS software) whereas the tracking takes 0.2 s on the same PC in Matlab®, totalling 0.8 s. Progress in hardware development (e.g. implementation on GPU) can thus easily allow several SoS images per second frame rate, making CUTE promising as an addition to real-time handheld US.

In summary, the new model is an important step towards quantitative clinical handheld reflection-mode SoS imaging. Thanks to the fast angle scanning of US systems and the low computational cost of CUTE, quantitative SoS images can be routinely displayed in parallel to conventional B-mode US. CUTE therefore can be used to image the SoS in any organ that can be examined using echo US. Furthermore, a more accurate estimation of the spatial distribution of SoS using the proposed new model will benefit an improved correction of conventional B-mode US images for SoS-related aberrations [38, 39]. Apart from hepatic imaging for diagnosing steatosis, another promising target is the female breast with the goal to improve breast cancer diagnostics. Whereas using a linear probe is suitable for e.g. breast imaging, transabdominal hepatic imaging is conventionally performed using curvilinear probes operating at lower frequencies. The presented methodology can readily be adapted to such probes, however, the disadvantage of a curvilinear probe compared to a linear one is the smaller angle range that can be used for Tx/Rx beamsteering, as the same grid node is within the acceptance angle of a smaller number of elements when these elements are pointing into diverging directions. Also, the ratio between the probe aperture length and the required depth range for full liver imaging limits the available angle range, resulting in reduced axial resolution in comparison to superficial tissue. In situations where one is interested in a local average quantitative reading rather than a spatially resolved distribution of SoS, the low axial resolution may not be important. In situations where the lack of spatial resolution becomes a problem, using a very large aperture linear array probe instead of a curved one could be a viable solution for hepatic imaging.

CUTE is based on phase tracking and thus sensitive to motion artifacts. Our in

vivo experience though shows that robust SoS images can be easily obtained when following a conventional breath hold procedure. When imaging near or inside a large blood vessel, however, blood flow and tissue clutter inhibit phase tracking and may cause SoS artefacts in the reconstruction. To overcome this limitation, we have already proposed a technique [53] where the first order echoes from the moving blood cells are separated from the static echo clutter via a clutter wall filter as in Doppler flow imaging. This technique extends the application of CUTE also to arteries, e.g. for the assessment of plaque inside the carotid artery and may also further improve liver imaging, since it can reduce SoS artefacts which may occur around hepatic veins.

Acknowledgement

This research was funded in part by the Swiss National Science Foundation (project number 205320_178038) and the European Union’s Horizon 2020 research and innovation programme under grant agreement No 732411, Photonics Private Public Partnership, and is supported by the Swiss State Secretariat for Education, Research and Innovation (SERI) under contract number 16.0162. The opinions expressed and arguments employed herein do not necessarily reflect the official view of the Swiss Government. The authors thank René Nyffenegger for his technical assistance.

Data availability

The experimental data used in this study are available on request from the corresponding Author.

References

- [1] J. Baker, P. J. Kornguth, M. S. Soo, R. Walsh, and P. Mengoni, “Sonography of solid breast lesions: observer variability of lesion description and assessment,” *AJR. American journal of roentgenology*, vol. 172, no. 6, pp. 1621–1625, 1999.
- [2] K. Konno, H. Ishida, M. Sato, T. Komatsuda, J. Ishida, H. Naganuma, Y. Hamashima, and S. Watanabe, “Liver tumors in fatty liver: difficulty in ultrasonographic interpretation,” *Abdominal imaging*, vol. 26, no. 5, pp. 487–491, 2001.
- [3] G. Rahbar, A. C. Sie, G. C. Hansen, J. S. Prince, M. L. Melany, H. E. Reynolds, V. P. Jackson, J. W. Sayre, and L. W. Bassett, “Benign versus malignant solid breast masses: Us differentiation,” *Radiology*, vol. 213, no. 3, pp. 889–894, 1999.

- [4] A. Athanasiou, A. Tardivon, M. Tanter, B. Sigal-Zafrani, J. Bercoff, T. Defieux, J.-L. Gennisson, M. Fink, and S. Neuenschwander, “Breast lesions: quantitative elastography with supersonic shear imaging—preliminary results,” *Radiology*, vol. 256, no. 1, pp. 297–303, 2010.
- [5] J. Bamber, D. Cosgrove, C. Dietrich, J. Fromageau, J. Bojunga, F. Calliada, V. Cantisani, J.-M. Correas, M. D’onofrio, E. Drakonaki, *et al.*, “EfsUMB guidelines and recommendations on the clinical use of ultrasound elastography. part 1: Basic principles and technology,” *Ultraschall in der Medizin-European Journal of Ultrasound*, vol. 34, no. 02, pp. 169–184, 2013.
- [6] R. G. Barr, “Real-time ultrasound elasticity of the breast: initial clinical results,” *Ultrasound quarterly*, vol. 26, no. 2, pp. 61–66, 2010.
- [7] D. Cosgrove, F. Piscaglia, J. Bamber, J. Bojunga, J.-M. Correas, O. Gilja, A. Klauser, I. Sporea, F. Calliada, V. Cantisani, *et al.*, “EfsUMB guidelines and recommendations on the clinical use of ultrasound elastography. part 2: Clinical applications,” *Ultraschall in der Medizin-European Journal of Ultrasound*, vol. 34, no. 03, pp. 238–253, 2013.
- [8] C. F. Dietrich, J. Bamber, A. Berzigotti, S. Bota, V. Cantisani, L. Castera, D. Cosgrove, G. Ferraioli, M. Friedrich-Rust, O. H. Gilja, *et al.*, “EfsUMB guidelines and recommendations on the clinical use of liver ultrasound elastography, update 2017 (long version),” *Ultraschall in der Medizin-European Journal of Ultrasound*, vol. 38, no. 04, pp. e16–e47, 2017.
- [9] R. M. Sigrist, J. Liao, A. El Kaffas, M. C. Chammas, and J. K. Willmann, “Ultrasound elastography: review of techniques and clinical applications,” *Theranostics*, vol. 7, no. 5, p. 1303, 2017.
- [10] S. Hu and L. V. Wang, “Photoacoustic imaging and characterization of the microvasculature,” *Journal of biomedical optics*, vol. 15, no. 1, p. 011101, 2010.
- [11] M. Jaeger, D. C. Harris-Birtill, A. G. Gertsch-Grover, E. O’Flynn, and J. C. Bamber, “Deformation-compensated averaging for clutter reduction in epiphotoacoustic imaging in vivo,” *Journal of biomedical Optics*, vol. 17, no. 6, p. 066007, 2012.
- [12] K. G. Held, M. Jaeger, J. Rička, M. Frenz, and H. G. Akarçay, “Multiple irradiation sensing of the optical effective attenuation coefficient for spectral correction in handheld oa imaging,” *Photoacoustics*, vol. 4, no. 2, pp. 70–80, 2016.
- [13] L. Ulrich, L. Ahnen, H. Akarçay, S. Sanchez, M. Jaeger, G. Held, M. Wolf, and M. Frenz, “Spectral correction for handheld optoacoustic imaging by means of near-infrared optical tomography in reflection mode,” 08 2018.

- [14] N. Ruiter, M. Zapf, R. Dapp, T. Hopp, W. Kaiser, and H. Gemmeke, “First results of a clinical study with 3d ultrasound computer tomography,” in *2013 IEEE International Ultrasonics Symposium (IUS)*, pp. 651–654, IEEE, 2013.
- [15] J. F. Greenleaf and R. C. Bahn, “Clinical imaging with transmissive ultrasonic computerized tomography,” *IEEE Transactions on Biomedical Engineering*, no. 2, pp. 177–185, 1981.
- [16] J. Jago and T. Whittingham, “Experimental studies in transmission ultrasound computed tomography,” *Physics in Medicine & Biology*, vol. 36, no. 11, p. 1515, 1991.
- [17] G. Zografos, D. Koulocheri, P. Liakou, M. Sofras, S. Hadjiagapis, M. Orme, and V. Marmarelis, “Novel technology of multimodal ultrasound tomography detects breast lesions,” *European radiology*, vol. 23, no. 3, pp. 673–683, 2013.
- [18] P. L. Carson, C. R. Meyer, A. L. Scherzinger, and T. V. Oughton, “Breast imaging in coronal planes with simultaneous pulse echo and transmission ultrasound,” *Science*, vol. 214, no. 4525, pp. 1141–1143, 1981.
- [19] P. Huthwaite and F. Simonetti, “High-resolution imaging without iteration: A fast and robust method for breast ultrasound tomography,” *The Journal of the Acoustical Society of America*, vol. 130, no. 3, pp. 1721–1734, 2011.
- [20] J. Wiskin, D. Borup, S. Johnson, and M. Berggren, “Non-linear inverse scattering: High resolution quantitative breast tissue tomography,” *The Journal of the Acoustical Society of America*, vol. 131, no. 5, pp. 3802–3813, 2012.
- [21] G. Sandhu, C. Li, O. Roy, S. Schmidt, and N. Duric, “Frequency domain ultrasound waveform tomography: breast imaging using a ring transducer,” *Physics in Medicine & Biology*, vol. 60, no. 14, p. 5381, 2015.
- [22] M. C. Hesse, L. Salehi, and G. Schmitz, “Nonlinear simultaneous reconstruction of inhomogeneous compressibility and mass density distributions in unidirectional pulse-echo ultrasound imaging,” *Physics in Medicine and Biology*, vol. 58, no. 17, p. 6163, 2013.
- [23] H.-C. Shin, R. Prager, H. Gomersall, N. Kingsbury, G. Treece, and A. Gee, “Estimation of average speed of sound using deconvolution of medical ultrasound data,” *Ultrasound in medicine & biology*, vol. 36, no. 4, pp. 623–636, 2010.
- [24] J. Krucker, J. B. Fowlkes, and P. L. Carson, “Sound speed estimation using automatic ultrasound image registration,” *IEEE transactions on ultrasonics, ferroelectrics, and frequency control*, vol. 51, no. 9, pp. 1095–1106, 2004.

- [25] M. Imbault, A. Faccinetto, B.-F. Osmanski, A. Tissier, T. Deffieux, J.-L. Gennisson, V. Vilgrain, and M. Tanter, “Robust sound speed estimation for ultrasound-based hepatic steatosis assessment,” *Physics in Medicine and Biology*, vol. 62, no. 9, p. 3582, 2017.
- [26] M. Kondo, K. Takamizawa, M. Hirama, K. Okazaki, K. Iinuma, and Y. Takehara, “An evaluation of an in vivo local sound speed estimation technique by the crossed beam method,” *Ultrasound in Medicine and Biology*, vol. 16, no. 1, pp. 65–72, 1990.
- [27] I. Céspedes, J. Ophir, and Y. Huang, “On the feasibility of pulse-echo speed of sound estimation in small regions: Simulation studies,” *Ultrasound in Medicine and Biology*, vol. 18, no. 3, pp. 283–291, 1992.
- [28] M. Jakovljevic, S. Hsieh, R. Ali, G. Chau Loo Kung, D. Hyun, and J. J. Dahl, “Local speed of sound estimation in tissue using pulse-echo ultrasound: Model-based approach,” *The Journal of the Acoustical Society of America*, vol. 144, no. 1, pp. 254–266, 2018.
- [29] M. Jaeger, G. Held, S. Peeters, S. Preisser, M. Grünig, and M. Frenz, “Computed ultrasound tomography in echo mode for imaging speed of sound using pulse-echo sonography: proof of principle,” *Ultrasound in medicine and biology*, vol. 41, no. 1, pp. 235–250, 2015.
- [30] M. Jaeger and M. Frenz, “Towards clinical computed ultrasound tomography in echo-mode: Dynamic range artefact reduction,” *Ultrasonics*, vol. 62, pp. 299–304, 2015.
- [31] T. Loupas, J. Powers, and R. W. Gill, “An axial velocity estimator for ultrasound blood flow imaging, based on a full evaluation of the doppler equation by means of a two-dimensional autocorrelation approach,” *IEEE transactions on ultrasonics, ferroelectrics, and frequency control*, vol. 42, no. 4, pp. 672–688, 1995.
- [32] S. Flax and M. O’Donnell, “Phase-aberration correction using signals from point reflectors and diffuse scatterers: Basic principles,” *IEEE transactions on ultrasonics, ferroelectrics, and frequency control*, vol. 35, no. 6, pp. 758–767, 1988.
- [33] L. Nock, G. E. Trahey, and S. W. Smith, “Phase aberration correction in medical ultrasound using speckle brightness as a quality factor,” *The Journal of the Acoustical Society of America*, vol. 85, no. 5, pp. 1819–1833, 1989.
- [34] D. Rachlin, “Direct estimation of aberrating delays in pulse-echo imaging systems,” *The Journal of the Acoustical Society of America*, vol. 88, no. 1, pp. 191–198, 1990.

- [35] Y. Li, “Phase aberration correction using near-field signal redundancy. i. principles [ultrasound medical imaging],” *IEEE transactions on ultrasonics, ferroelectrics, and frequency control*, vol. 44, no. 2, pp. 355–371, 1997.
- [36] Y. Li, D. Robinson, and D. Carpenter, “Phase aberration correction using near-field signal redundancy. ii. experimental results,” *IEEE transactions on ultrasonics, ferroelectrics, and frequency control*, vol. 44, no. 2, pp. 372–379, 1997.
- [37] M. A. Haun, D. L. Jones, and W. Oz, “Overdetermined least-squares aberration estimates using common-midpoint signals,” *IEEE transactions on medical imaging*, vol. 23, no. 10, pp. 1205–1220, 2004.
- [38] M. Jaeger, E. Robinson, H. G. Akarçay, and M. Frenz, “Full correction for spatially distributed speed-of-sound in echo ultrasound based on measuring aberration delays via transmit beam steering,” *Physics in medicine & biology*, vol. 60, no. 11, p. 4497, 2015.
- [39] H.-M. Schwab, A. Ihrig, D. Depke, S. Hermann, M. Schäfers, and G. Schmitz, “Aberration correction in photoacoustic imaging using paraxial backpropagation,” in *2017 IEEE International Ultrasonics Symposium (IUS)*, pp. 1–4, IEEE, 2017.
- [40] M. Jaeger and M. Frenz, “Quantitative imaging of speed of sound in echo ultrasonography.” *IEEE International Ultrasound Symposium*, Taipei, 2015.
- [41] S. J. Sanabria, E. Ozkan, M. Rominger, and O. Goksel, “Spatial domain reconstruction for imaging speed-of-sound with pulse-echo ultrasound: simulation and in vivo study,” *Physics in Medicine & Biology*, vol. 63, no. 21, p. 215015, 2018.
- [42] L. Ruby, S. J. Sanabria, K. Martini, K. J. Dedes, D. Vorburger, E. Oezkan, T. Frauenfelder, O. Goksel, and M. B. Rominger, “Breast cancer assessment with pulse-echo speed of sound ultrasound from intrinsic tissue reflections: Proof-of-concept,” *Investigative radiology*, vol. 54, no. 7, pp. 419–427, 2019.
- [43] J. B. Bednar, “Modeling, migration and velocity analysis in simple and complex structure,” *by Panorama Technologies, Inc*, 2009.
- [44] R. Rau, D. Schweizer, V. Vishnevskiy, and O. Goksel, “Speed-of-sound imaging using diverging waves,” *arXiv preprint arXiv:1910.05935*, 2019.
- [45] W. F. Walker and G. E. Trahey, “The application of k-space in pulse echo ultrasound,” *IEEE transactions on ultrasonics, ferroelectrics, and frequency control*, vol. 45, no. 3, pp. 541–558, 1998.

- [46] J. Bercoff, “Ultrafast ultrasound imaging,” in *Ultrasound imaging-Medical applications*, IntechOpen, 2011.
- [47] G. Montaldo, M. Tanter, J. Bercoff, N. Benech, and M. Fink, “Coherent plane-wave compounding for very high frame rate ultrasonography and transient elastography,” *IEEE transactions on ultrasonics, ferroelectrics, and frequency control*, vol. 56, no. 3, pp. 489–506, 2009.
- [48] E. L. Madsen, J. A. Zagzebski, and G. R. Frank, “An anthropomorphic ultrasound breast phantom containing intermediate-sized scatterers,” *Ultrasound in Medicine and Biology*, vol. 8, no. 4, pp. 381–392, 1982.
- [49] E. Madsen, G. Frank, T. Krouskop, T. Varghese, F. Kallel, and J. Ophir, “Tissue-mimicking oil-in-gelatin dispersions for use in heterogeneous elastography phantoms,” *Ultrasonic imaging*, vol. 25, no. 1, pp. 17–38, 2003.
- [50] E. L. Madsen, M. A. Hobson, G. R. Frank, H. Shi, J. Jiang, T. J. Hall, T. Varghese, M. M. Doyley, and J. B. Weaver, “Anthropomorphic breast phantoms for testing elastography systems,” *Ultrasound in medicine and biology*, vol. 32, no. 6, pp. 857–874, 2006.
- [51] M. M. Nguyen, S. Zhou, J.-l. Robert, V. Shamdasani, and H. Xie, “Development of oil-in-gelatin phantoms for viscoelasticity measurement in ultrasound shear wave elastography,” *Ultrasound in medicine and biology*, vol. 40, no. 1, pp. 168–176, 2014.
- [52] T. Lin, J. Ophir, and G. Potter, “Correlations of sound speed with tissue constituents in normal and diffuse liver disease,” *Ultrasonic imaging*, vol. 9, no. 1, pp. 29–40, 1987.
- [53] M. Kuriakose, J.-W. Muller, P. Stähli, M. Frenz, and M. Jaeger, “Receive beam-steering and clutter reduction for imaging the speed-of-sound inside the carotid artery,” *Journal of Imaging*, vol. 4, no. 12, p. 145, 2018.

Chapter 3

Bayesian approach for a robust speed-of-sound reconstruction using pulse-echo ultrasound

PATRICK STÄHLI¹, MARTIN FRENZ¹, MICHAEL JAEGER¹

Abstract

Computed ultrasound tomography in echo mode (CUTE) is a promising ultrasound (US) based multi-modal technique that allows to image the spatial distribution of speed of sound (SoS) inside tissue using hand-held pulse-echo US. It is based on measuring the phase shift of echoes when detected under varying steering angles. The SoS is then reconstructed using a regularized inversion of a forward model that describes the relation between the SoS and echo phase shift. Promising results were obtained in phantoms when using a Tikhonov-type regularization of the spatial gradient (SG) of SoS. In-vivo, however, clutter and aberration lead to an increased phase noise. In many subjects, this phase noise causes strong artifacts in the SoS image when using the SG regularization. To solve this shortcoming, we propose to use a Bayesian framework for the inverse calculation, which includes *a priori* statistical properties of the spatial distribution of the SoS to avoid noise-related artifacts in the SoS images. In this study, the *a priori* model is based on segmenting the B-Mode image. We show in a simulation and phantom study that this approach leads to SoS images that are much more stable against phase noise compared to the SG regularization. In a preliminary in-vivo study, a reproducibility in the range of 10 ms^{-1} was achieved when imaging the SoS of a volunteer's liver from different scanning locations. These results demonstrate the diagnostic potential of CUTE for example for the staging of fatty liver disease.

The work presented in this chapter has been submitted to IEEE Transaction on Medical Imaging in March 2020. The revision is currently in process.

¹Institute of Applied Physics, University of Bern, Sidlerstrasse 5, 3012 Bern, Switzerland

3.1 Introduction

Classical gray scale B-Mode ultrasound (US) determines the tissue's echogenicity and displays it in a spatially resolved way. In that way, it allows the evaluation of various traumatic and pathologic conditions and is therefore routinely used in today's clinical diagnostic practice. However, US often suffers from non-specific contrast and low sensitivity for certain disease types [1–3]. To improve its diagnostic accuracy, much effort has been placed in recent years in developing new ultrasound-based multi-modal approaches that complement classical gray scale B-Mode images with additional functional and structural information [4–13].

Speed-of-sound (SoS) imaging is a promising candidate to further improve US based diagnosis. It allows the identification of disease-related alterations of tissue composition and structure, based on their influence on the speed at which US propagates through tissue. SoS imaging can be divided into two categories: through-transmission and reflection mode imaging. Through-transmission techniques reconstruct the spatial distribution of SoS by analysing US transmitted through the tissue from various different angles. Breast ultrasound tomography demonstrates impressively the diagnostic potential of through transmission SoS imaging on the example of breast cancer diagnosis [14–16]. Although breast UCT yields quantitative SoS images with high spatial and contrast resolution, it requires a bulky stand-alone system and an acoustically transparent target, which limits its application mainly to the female breast.

In contrast, SoS imaging in reflection mode has the advantage that it provides all the flexibility of conventional US. Thus, implementation in a state-of-the art equipment would allow to image the SoS distribution in any part of the human body. Therefore, it could extend the applicability of SoS imaging to e.g the diagnosis of cancer other than in the breast, the assessment of fatty liver disease, or the characterization of plaque composition inside large blood vessels. Various approaches that estimate the spatial distribution of SoS based on pulse-echo signals have been investigated so far [17–23]. Quantitative reflection mode determination of average SoS (as opposed to imaging) has been demonstrated in the liver in vivo [24], proving the diagnostic value of SoS in the example of fatty liver disease [25].

Recently, we have developed a reflection-mode technique called computed ultrasound tomography in echo mode (CUTE) that allows handheld imaging of the spatial distribution of SoS in real time[26]. The working principle of CUTE is as follows: radio-frequency (rf) mode US images are beamformed (using e.g. conventional delay-and-sum algorithm) under a set of various different transmit (Tx) and receive (Rx) angles. The deviation of the true SoS from the SoS that is assumed for beamforming results in a mismatch between the actual and anticipated round trip time of US propagation (henceforth termed 'aberration delay'). Detecting echoes

under varying angles of US transmission and reception leads to a changing value of the aberration delay which is in turn reflected in a phase shift of the detected echos. This phase shift can be quantified in a spatially resolved way by using e.g. Loupas or Kasai type phase correlation [27, 28]. A forward model [29] relates these measured echo-phase shifts to the spatial distribution of local SoS, which can be derived by solving the inverse problem. One of the difficulties that arises when solving such inverse problems is that small variations in the inputs (e.g. caused by measurement noise) can cause large changes in the solution [30]. To stabilize the solution, some sort of regularization must be included in the inverse problem formulation to give preference to a particular solution with desirable properties, where the meaning of desirable properties is defined *a priori*. A Tikhonov type regularization of the spatial gradient (SG) of SoS was used in previous studies [29, 31], based on the expectation that the distribution of SoS inside a tissue is smooth and does not vary strongly on a short spatial scale. Promising results were achieved in phantom studies using this technique [29]. In-vivo, however, clutter and aberration often lead to an increased phase noise compared to phantoms, resulting in detrimental artifacts. Even worse, since the spatial distribution of this phase noise changes when changing the transducer position, the SoS images not only suffer from a high level of artifacts but are also not reproducible when imaging an organ (e.g. the liver) from different scanning locations.

To solve this shortcoming, we propose to use a Bayesian framework for the inverse calculation, as frequently applied in geophysical inverse theories [30, 32–35]. One of the advantages of the Bayesian framework is that it provides an intuitive and practical way to include a physically motivated *a priori* statistical model about the distribution of SoS into the formulation of the inverse calculation. Promising results have been reported using this approach in US through-transmission tomography, where it improves axial resolution when only a limited set of angles are available [36].

In this study, the *a priori* information is derived from the B-Mode images and encoded in a covariance matrix that gives a statistical description of the range and spatial correlation of the expected spatial distribution of SoS. This covariance matrix then acts as a regularization term to stabilize the solution of the inverse problem. It turns out that this approach makes the SoS reconstruction less prone to noise and thus leads to more reproducible SoS images compared to the SG regularization.

Building on [37], this study evaluates and compares the performance of both regularization approaches in simulation as well as phantom experiments. In preparation of one of our target clinical applications, and to demonstrate the benefit of the Bayesian approach also in-vivo, the regularization techniques are also compared in an exemplary in-vivo scenario, imaging the abdominal wall and liver tissue of a healthy volunteer.

3.2 Materials and Methods

As in previous studies, CUTE was implemented using plane-wave pulse-echo rf-data that are acquired and beamformed (using delay-and-sum together with coherent plane-wave compounding) for a set of various different transmit (Tx) and receive (Rx) angles. Applying the common-mid-angle approach with the same experimental parameters as outlined in [29], maps of local echo-phase shift are then determined between angle combinations (Tx: $\phi_n \rightarrow \phi_{n+1}$, Rx: $\psi_m \rightarrow \psi_{m-1}$) for angles (ϕ, ψ) ranging from -25° to 25° in 10° steps.

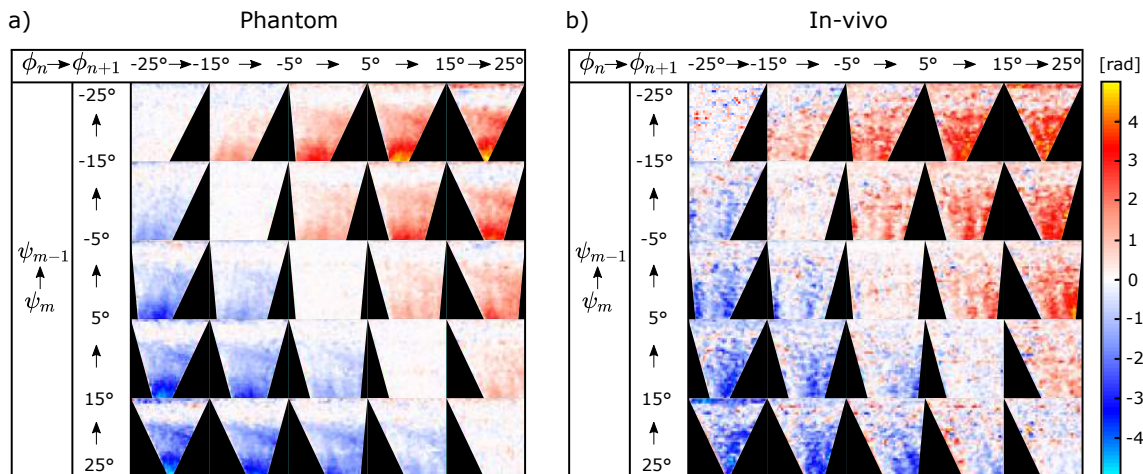


Figure 3.1: Exemplary echo-phase shift maps determined between angle combinations (Tx: $\phi_n \rightarrow \phi_{n+1}$, Rx: $\psi_m \rightarrow \psi_{m-1}$) for angles (ϕ, ψ) ranging from -25° to 25° in 10° steps for a) a phantom mimicking the abdominal wall and liver tissue (see Fig. 3.3a) and b) imaging the liver through the abdominal wall for a healthy volunteer (scanning location A, see Fig. 3.3b)

Fig. 3.1 shows exemplary the echo-phase shift maps determined in a phantom mimicking the abdominal wall and liver tissue (see section 3.2.4, Phantom C) and when imaging the liver of a healthy volunteer through the abdominal wall (see section 3.3.3, scanning location A). Due to the similarity of the spatial distribution of SoS between the phantom and the in-vivo scenario, also the phase shift maps look similar. However, the phase shift maps determined in-vivo are contaminated by a higher level of phase noise.

The SoS is reconstructed by relating – via a forward model \mathbf{M} [29] – the vectorized echo phase shift maps $\Delta\Theta$ to the vectorized distribution of slowness deviation Δs , i.e. the difference between the actual slowness (inverse SoS) and the reference slowness that is used for beamforming. Assuming that sound propagation follows the straight-ray approximation, this forward model is linear and can thus be formulated in matrix notation:

$$\Delta\Theta = \mathbf{M}\Delta s + \epsilon \quad (3.1)$$

ϵ describes the measurement noise that contaminates the echo-phase shift maps as indicated in Fig. 3.1. In the following, two different approaches are described and

investigated that estimate Δs based on Eq. 3.1.

3.2.1 SoS reconstruction based on spatial gradient regularization

Since \mathbf{M} is poorly-conditioned and $\Delta\Theta$ steadily contaminated by noise, Eq. 3.1 is not expected to have an exact solution. Instead, an objective function $L(\Delta s)$ via the squared L2 norm of the residuals is formulated:

$$L(\Delta s) = \|\Delta\Theta - \mathbf{M}\Delta s\|_2^2 + \|\mathbf{T}\Delta s\|_2^2 \quad (3.2)$$

The second term on the right-hand side of the Eq. 3.2 denotes the regularization term that prevents the estimated slowness deviation to be unduly sensitive to noise-related variations in the measurement data vector $\Delta\Theta$. By minimizing the objective function $L(\Delta s)$, it follows that the estimated slowness deviation $\widehat{\Delta s}$ is given by:

$$\widehat{\Delta s} = (\mathbf{M}^T\mathbf{M} + \mathbf{T})^{\text{inv}} \mathbf{M}^T \Delta\Theta \quad (3.3)$$

The estimated SoS \hat{c} is finally recovered from the estimated slowness deviation $\widehat{\Delta s}$ according to:

$$\hat{c} = \left(\widehat{\Delta s} + \frac{1}{c_0} \right)^{-1} \cong c_0 - c_0^2 \widehat{\Delta s} \quad (3.4)$$

where c_0 designates the anticipated SoS that is used for beamforming.

In line with previous studies[29, 31], the regularization matrix \mathbf{T} is based on finite difference operators in x and z direction with independent regularization parameters γ_x and γ_z :

$$\mathbf{T} = \gamma_x^2 \mathbf{D}_x^T \mathbf{D}_x + \gamma_z^2 \mathbf{D}_z^T \mathbf{D}_z \quad (3.5)$$

The finite difference regularization enforces a smooth slowness profile of the to-be reconstructed slowness without imposing a constraint on the mean slowness.

3.2.2 SoS reconstruction using *a priori* knowledge

Whereas the previously described parameter estimation of Δs was based on a purely algebraic framework, it can also be derived based on a Bayesian interpretation of the forward problem, as has been thoroughly developed in [30] and described in great detail in [38]. Based on Bayes' theorem, the posterior probability density $P(\Delta s|\Delta\Theta)$ is the probability of the parameters Δs given the evidence $\Delta\Theta$:

$$P(\Delta s|\Delta\Theta) \propto P(\Delta s)P(\Delta\Theta|\Delta s) \quad (3.6)$$

In this study, a Gaussian *a priori* probability distribution $P(\Delta s)$ that is centred upon a mean value Δs_p with a covariance matrix \mathbf{C}_M is assumed.

$$P(\Delta s) \propto \exp \left[-\frac{1}{2}(\Delta s - \Delta s_p)^T \mathbf{C}_M^{-1}(\Delta s - \Delta s_p) \right] \quad (3.7)$$

Further, it is assumed that the noise ϵ is also Gaussian in form with a covariance matrix \mathbf{C}_N , centred upon the prediction of the forward model.

$$P(\Delta \Theta | \Delta s) \propto \exp \left[-\frac{1}{2}(\Delta \Theta - \mathbf{M}\Delta s)^T \mathbf{C}_N^{-1}(\Delta \Theta - \mathbf{M}\Delta s) \right] \quad (3.8)$$

It is then possible to show that the posterior probability distribution for the model parameters Δs is [38]:

$$P(\Delta s | \Delta \Theta) \propto \exp \left[-\frac{1}{2}(\Delta s - \widehat{\Delta s})^T \widehat{\mathbf{C}}^{-1}(\Delta s - \widehat{\Delta s}) \right] \quad (3.9)$$

where $\widehat{\mathbf{C}}$ denotes the posterior covariance matrix.

$$\widehat{\mathbf{C}} = (\mathbf{M}^T \mathbf{C}_N^{-1} \mathbf{M} + \mathbf{C}_M^{-1})^{-1} \quad (3.10)$$

Since the posterior distribution is Gaussian, the most likely solution to the inverse problem is given by the mean of the posterior distribution $\widehat{\Delta s}$:

$$\widehat{\Delta s} = \Delta s_p + \widehat{\mathbf{C}} \mathbf{M}^T \mathbf{C}_N^{-1}(\Delta \Theta - \mathbf{M}\Delta s_p) \quad (3.11)$$

The estimation of the slowness deviation in Eq. 3.11 allows to conveniently include statistical *a priori* knowledge. Uncertainties associated with the forward modelling procedure (e.g. model discretization errors or uncertainties in the data as e.g. ambient noise) can in principle be included in the noise covariance matrix \mathbf{C}_N . In this study, however, we assume that the forward model has no uncertainties and that the ambient noise is uncorrelated. This leads to \mathbf{C}_N being a diagonal matrix with all diagonal elements equal to an identical value σ_N^2 that describes the noise level in the data.

Δs_p denotes the *a priori* mean of the slowness deviation Δs . In this study, we assume that Δs_p is 0 everywhere, i.e. the *a priori* favored solution for the SoS is equal to c_0 .

The covariance matrix \mathbf{C}_M allows to include a statistical *a priori* model about the inter-pixel correlation of SoS. Such *a priori* knowledge can be derived from the B-Mode image that is reconstructed in parallel to CUTE. To generate the covariance matrix \mathbf{C}_M , the B-Mode image is in a first step segmented into N regions within which a correlation of the SoS is expected. In the present study this segmentation is performed by visual inspection. For example, the B-Mode image shown in Fig.

3.2a is segmented into $N = 4$ regions representing the subcutaneous fat layer (SF), the rectus abdominis muscle (M), the post peritoneal fat layer (PF) and the liver (L). For each segment k , a segmentation matrix \mathbf{R}_k is created where the entries are set to a value r within the segments and 0 outside (see Fig. 3.2 b). From these segmentation matrices, a correlation matrix \mathbf{K} is generated:

$$\mathbf{K} = \left[\sum_{k=1}^{N=4} \text{vec}(\mathbf{R}_k) \text{vec}(\mathbf{R}_k)^T \right] \quad (3.12)$$

In \mathbf{K} , the elements $\rho(i, j) = r^2$ denote the expected correlation of SoS between pixels i and j . Since the segments are generated with the purpose to represent different tissue regions, typically a high correlation of SoS is expected within a segment. Therefore, whenever nothing else is mentioned, ρ was set to 0.9 for the intra-segment correlation ($r = \sqrt{0.9}$). Note that the correlation between pixels across different segments is 0 (per the definition of \mathbf{K} via the matrices \mathbf{R}).

Finally, the covariance matrix \mathbf{C}_M is formulated as follows:

$$\mathbf{C}_M(i, j) = \begin{cases} \sigma_S^2 & \text{if } i = j \\ \mathbf{K}(i, j) \sigma_S^2 & \text{else} \end{cases} \quad (3.13)$$

Note that the case $i = j$ in Eq. 3.13 accounts for the fact that the correlation of a pixel with itself is 1. σ_S designates the average variation of the estimated slowness deviation Δs from the *a priori* slowness deviation Δs_p . σ_S is expressed in the units of slowness but can be related to the more intuitive unit of SoS by using Eq. 3.4:

$$\sigma_C \cong \sigma_S c_0^2 \quad (3.14)$$

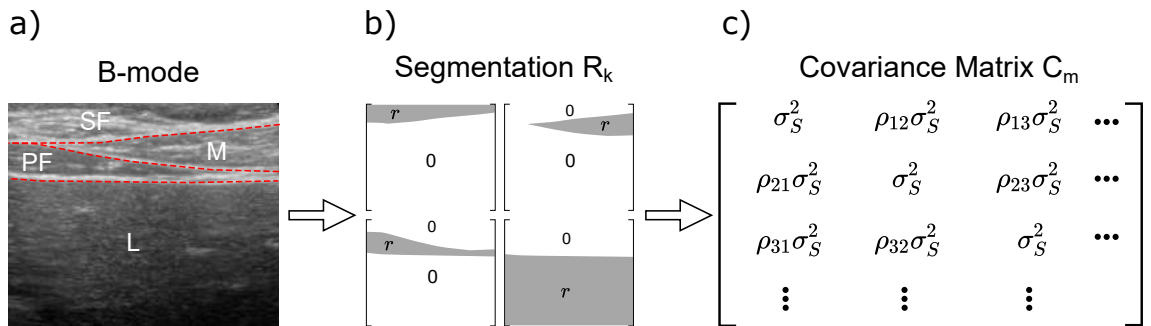


Figure 3.2: Sketch of the segmentation process: (a) The B-Mode image is segmented by hand into the different tissue regions within which a correlated SoS is expected. Here, the segments represent the subcutaneous fat layer (SF), the rectus abdominis muscle (M), the post peritoneal fat layer (PF) and the liver (L). (b) Each k -th segment is represented in a corresponding segmentation matrix \mathbf{R}_k , where the entries are set to a value r within the segments and 0 outside. (c) The \mathbf{R}_k are then used to construct the covariance matrix \mathbf{C}_m , where the expected correlation between pixels is described by the coefficient $\rho = r^2$. In case of no correlation of SoS (not in the same segment), the correlation coefficient ρ is 0. σ_S describes the expected average variation of the slowness deviation from *a priori* slowness deviation Δs_p .

The *a priori* information that is encoded into the parameter estimation is considered "soft" because it does not force the estimated slowness deviation inside a segment to be constant. Rather, SoS variations within the predefined segments are regularized, but not across the boundaries. Thus, in line with e.g. [39–41], we refer to this regularization as "soft-prior regularization", i.e. "SP regularization".

3.2.3 Synthetic dataset

The two regularization methods were compared in a simulation study that contained various digital phantoms (DP) of different geometries (see. Fig. 3.5 top row). DP 1 to DP 4 represent phantoms with inclusions of different shapes (SoS 1570 ms^{-1}) embedded in a homogeneous background (SoS 1540 ms^{-1}). DP 5 to 8 mimic layered structures as one would expect when scanning the liver through the abdomen. In DP 5 and 6, the SoS of the top layer was 1490 ms^{-1} (mimicking fat tissue) and the SoS of the bottom layer 1570 ms^{-1} (mimicking liver tissue). In addition to DP 5 and 6, DP 7 and 8 contained a triangular shaped layer embedded into the top layer with a SoS of 1585 ms^{-1} (mimicking muscle tissue). Further, DP 5 and 8 contained a circular inclusion embedded in the bottom layer with a SoS of 1600 ms^{-1} (mimicking a cancer).

Simulation of the echo shift that would be caused by these phantoms was based on determining the aberration delay using the hybrid angular spectrum approach [42], and on linking the aberration delay to echo shift using the forward model described in [29]. The advantage of the hybrid angular spectrum approach compared to other approaches is that – while being computationally efficient – it accounts for refraction/diffraction. This allows one to observe whether specific artefacts are to be expected due to the deviation of true sound propagation from the straight-ray approximation used in SoS reconstruction. The phase noise that is typically observed in-vivo was mimicked by adding uncorrelated phase shift variations, following a Gaussian distribution with a standard deviation of 0.9 rad and a mean of 0 rad. In-vivo, however, the phase noise that contaminates the phase shift might change during examination (e.g. when changing the transducer position slightly). To mimic this situation, three different realizations of the synthetic phase noise were generated, henceforth termed as noise 1 to 3.

3.2.4 Phantom design

The goal of the phantom study was to investigate the performance of both regularization approaches in a scenario mimicking an actual clinical application, namely imaging the liver through the abdominal wall, but where the actual ground truth of the SoS distribution is known. For this purpose, three phantoms that mimic the

abdominal wall and liver tissue were produced. These phantoms were composed of the following compartments: a subcutaneous fat-mimicking layer (C1), a triangular-shaped muscle-mimicking layer (C2) and a post peritoneal fat-mimicking layer (C3), stacked on top of a liver-mimicking compartment ($C4_{A,B,C}$). These liver-mimicking compartments exhibit various different SoS values (see Fig. 3.3a) that simulate the decrease of SoS due to the increase of the liver fat fraction at different stages of fatty liver disease. The individual phantom compartments were based on porcine gelatin (Geistlich Spezial Gelatine, health and life AG, Switzerland). Three different gelatin base solutions were prepared by dissolving 10, 20 and 30 wt% porcine gelatin in H_2O at a temperature of $75^\circ C$. To provide a diffuse echogenicity, 2 wt% cellulose (Sigmacell Cellulose Type 20, Sigma Aldrich, Switzerland) were mixed into the base solutions. The muscle compartment (C2) was produced from the 30 wt% base solution, providing a SoS of 1585 ms^{-1} after gelling at room temperature ($21^\circ C$). Three different liver compartments ($C4_{A,B,C}$) were produced from the three different base solutions, resulting in a SoS (after gelling at room temperature) of 1525 ms^{-1} , 1555 ms^{-1} and 1585 ms^{-1} , respectively. To mimic the fat compartments in the abdominal wall, medium-chain triglycerides (MCT) oil (Ceres-MCT Oil, Puravita, Switzerland, $\text{SoS} = 1350 \text{ ms}^{-1}$) was slowly blended under the gelatine base solution (20 wt%, not gelled yet, at a temperature of $65^\circ C$). During this process, an oil in gelatin emulsion was formed [43–46]. After gelling, the oil droplets were trapped within the gelatine matrix. The final SoS of such an emulsion is determined by the emulsion’s relative MCT oil weight content, in this study 0.33 wt%, resulting in a SoS of 1490 ms^{-1} (at room temperature). The mentioned reference SoS values were determined with a through-transmission time-of-flight set-up, having an accuracy of $\pm 5 \text{ ms}^{-1}$.

3.2.5 In-vivo data

The two regularization techniques were examined in an exemplary case of imaging the liver of a healthy volunteer (male, age 31, in compliance with the ethical principles of the Declaration of Helsinki 2018). In comparison to the simulation and phantom study where the performance of the regularization approaches was assessed by comparing the SoS images to a ground truth, no such reference exists for the liver in the investigated in-vivo scenario. Instead, the reproducibility of the SoS images was investigated by imaging the liver from various different scanning locations (see Fig. 3.3b).

3.2.6 Ultrasound system

For the experimental study, a Vantage 64 LE (Verasonics Inc., WA, USA) research US system in combination with an L7-4 linear vascular probe (ATL Philips, WA,

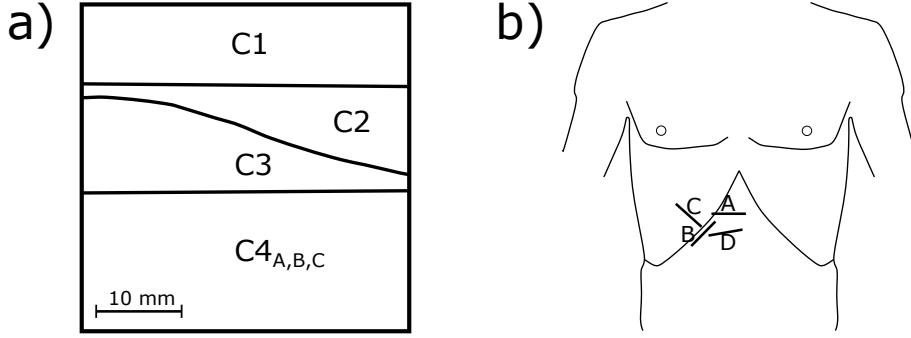


Figure 3.3: (a) Sketch of the phantom geometry mimicking the abdominal wall and liver tissue: subcutaneous fat mimicking layer (C1, $\text{SoS} = 1490 \text{ ms}^{-1}$), triangular shaped muscle (C2, $\text{SoS} = 1585 \text{ ms}^{-1}$), post peritoneal fat layer (C3, $\text{SoS} = 1490 \text{ ms}^{-1}$), liver mimicking compartment ($C4_{A,B,C}$, $\text{SoS} = [1525 \text{ ms}^{-1}, 1555 \text{ ms}^{-1} \text{ and } 1585 \text{ ms}^{-1}]$). (b) Sketch of the different scanning locations from where the liver was accessed.

USA) was used for the pulse-echo signal acquisition. The probe features a bandwidth from 4 to 7 MHz with 5 MHz center frequency, 128 elements at 0.29 mm pitch resulting in an aperture length of 38.4 mm. The system was connected via a PCI Express link to a host computer, facilitating real time data transfer. For the acquisition of plane wave pulse-echo data, a dedicated scan sequence was implemented as described in detail in [29]. In this study, the acquired data were stored on the host computer for an off-line SoS reconstruction that was implemented in MATLAB[®] (MathWorks inc.).

3.3 Results

3.3.1 Simulation study

In both regularization methods, the outcome can be tuned via the choice of the regularization parameters. The choice of the regularization parameters is therefore crucial in view of a comparison between the two methods. For a fair comparison, we have chosen to use for each regularization method the 'optimal' set of parameters that minimizes the root-mean-square error metric.

The optimization analysis was performed as a grid search by reconstructing SoS images for all DP's and noise realizations (see Sec. 3.2.3) with a variety of regularization parameter settings. The averaged RMSE (over all DP's and noise realizations) as a function of regularization parameter values are shown in Fig. 3.4. The smallest RMSE are marked with a yellow cross and the corresponding parameters are summarized in table 3.1.

The SoS images of all DP's and noise realizations reconstructed with these sets of optimal regularization parameters are shown in Fig. 3.5.

The SoS images that were reconstructed with the SG regularization show strong

Table 3.1: Regularization parameters that lead to the smallest mean RMSE among all DP's and noise realizations.

	Optimal regularization parameters	Mean RMSE
Spatial gradient	$\gamma_x = 84.1, \gamma_z = 17.6$	10.89 ms^{-1}
Soft-prior	$\sigma_C = 50 \text{ ms}^{-1}, \sigma_N = 1.5 \text{ rad}$	3.42 ms^{-1}

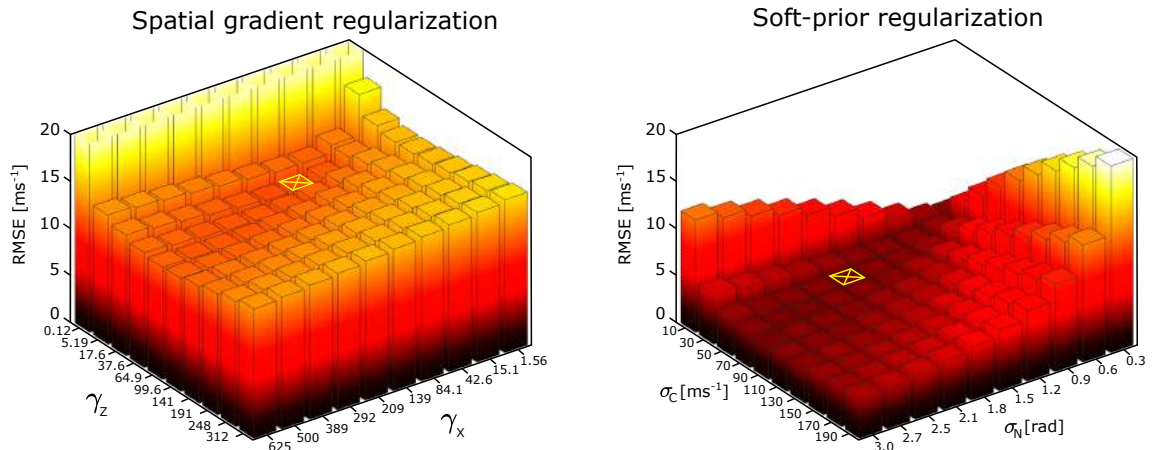


Figure 3.4: Mean RMSE over all DP's and noise realizations as a function of regularization parameters. The sets of parameters that lead to the smallest mean RMSE are marked with yellow crosses.

artifacts in all DP's. These artifacts mimic SoS variations that bias the ground truth and further impede an unambiguous identification of the SoS inclusions. The spatial distribution of these artifactual SoS variations changes among the different noise realizations but is rather constant across the different DP geometries. Further, the mean SoS within the segments are strongly influenced by the phase noise: whereas e.g. the mean SoS of the liver mimicking segment in the DP's 5 to 8 deviate only little from the ground truth with noise 1, they strongly deviate in the case of noise 3. Similarly in DP 1 to 4, the SoS underneath the inclusions deviates most strongly from the ground truth in case of noise 3.

A disadvantage of the spatial gradient regularization is that it results in a trade-off between a smooth SoS distribution inside compartments and a high spatial resolution across compartment boundaries. In situations with strong phase noise, a relatively strong regularization is needed to suppress high frequency artifacts (i.e. to enforce a smooth SoS distribution). Such strong regularization, however, results in a reduced spatial resolution of the reconstructed image. This effect is strongly pronounced in DP's 5 to 8: the strong regularization that was needed to minimize RMSE by enforcing smooth SoS distributions inside the individual compartments lead to blurred transitions across different compartments.

Contrary to the SG regularization, the SP regularization allows to minimize SoS

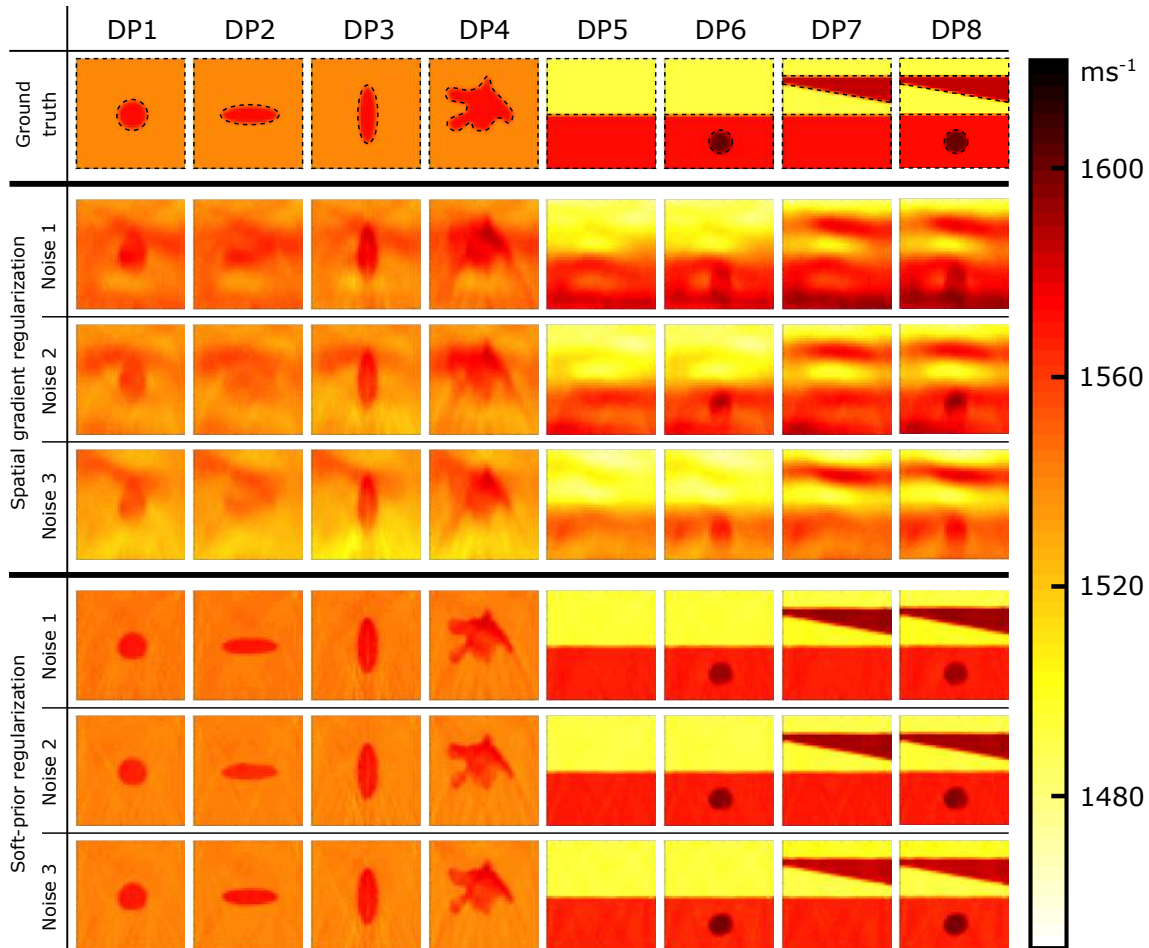


Figure 3.5: Simulation results: SoS images reconstructed with both regularization methods using the optimal set of regularization parameters and three different realizations of the phase noise. The top row shows the ground truth.

variations within the individual compartments without blurring transitions across boundaries. This results in a minimum RMSE that is more than a factor of 3 smaller in comparison to the SG regularization (see table. 3.1). Furthermore, all the SoS images reconstructed with the SP regularization agree well with the ground truth and show hardly any differences across the different synthetic phase noises.

So far, we assumed that the location and shape of the inclusion is *a priori* known so that it can be properly segmented. In an actual clinical scenario, however, a region of SoS contrast might not be clearly visible in the B-Mode image and is therefore potentially missed in the segmentation. To investigate such a case, the SoS images were again reconstructed (including phase noise 3) using the SP regularization but without segmenting the inclusions (see Fig. 3.6 top row). As described in Materials and Methods, the SP regularization includes a coefficient ρ that describes the correlation of SoS between two pixels within the same segment. So far, this coefficient was set to 0.9 to enforce a high correlation and therefore a smooth SoS distribution. In the following situation (see Fig. 3.6), the influence of the correlation parameter ρ on the SoS images is investigated by using various values of ρ between 0.5 and 0.99.

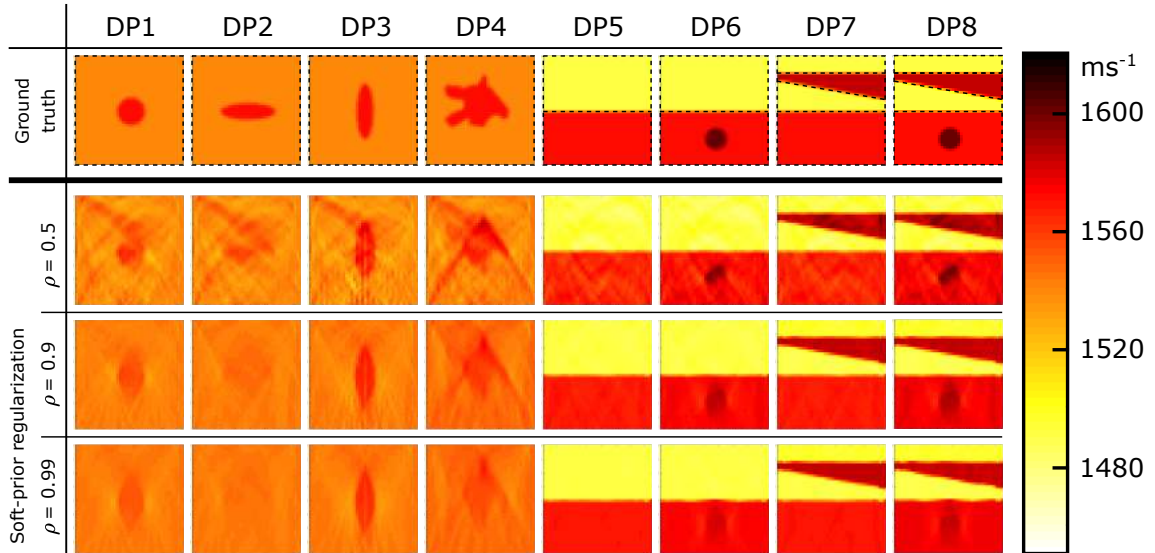


Figure 3.6: Simulation results: SoS images reconstructed with the SP regularization without segmenting the inclusions. The top row shows the ground truth, where the black dashed lines indicate the segmentation. The SoS images were reconstructed with different values for the correlation coefficient ρ , based on the simulated phase shift maps including artificial phase noise 3.

The SoS images (see Fig 3.6) show that – even though the inclusions were not included as part of the *a priori* knowledge – their influence on the SoS image is well visible for most of the DP’s. However, for ρ close to 1, the SoS images show a very bad axial resolution. Consequently, the inclusions in DP2 and DP4 are barely visible because they are bounded mainly by horizontal boundaries. On the contrary, the good visibility of the inclusions in DP 1,3,6 and 8 relies on the good lateral resolution and the low level of artifacts.

A value for ρ of 0.5 results in SoS images with a better axial resolution. This results in a better visibility of the inclusions in DP2 and DP4. On the other hand, an increased level of artifacts is observed in all DP’s for such a value of ρ .

3.3.2 Phantom results

As described in Materials and Methods, three phantoms were investigated that mimic the abdominal wall and the liver tissue with various different liver SoS. The corresponding B-Mode images are shown in Fig. 3.7a (top row). The red lines indicate the segments that were identified for the SP regularization. The phase shift maps of these phantoms are contaminated only by a low level of phase noise (henceforth referred as ‘low noise’) (see Fig. 3.1a). In-vivo, however, a higher level of phase noise is typically observed, potentially due to a higher amount of multiple scattering processes and SoS inhomogeneities in the sub-resolution range (see Fig. 3.1b). To closely mimic the in-vivo scenario, SoS images were not only reconstructed with low noise but also after adding artificially generated phase noise (henceforth referred as ‘strong noise’).

The digital phantoms that were used for the optimization analysis in section 3.3.1

Table 3.2: Regularization parameters that lead to the smallest mean RMSE among all phantoms and phase noises.

	Optimal regularization parameters	Mean RMSE
Spatial gradient	$\gamma_x = 56.3, \gamma_z = 1.43$	19.17 ms^{-1}
Soft-prior	$\sigma_C = 30 \text{ ms}^{-1}, \sigma_N = 1.5 \text{ rad}$	6.17 ms^{-1}

contained not only layered but also inclusion structures. In the following, however, we specifically focus on layered samples, in view of the clinical application of liver imaging. For this reason, the optimal parameters found for the DP's are not necessarily representative for the phantom study. Therefore, a parameter optimization was again performed with the purpose to find the optimal set of regularization parameters for this particular scenario. To do so, a grid search was carried out with the goal to find the set of regularization parameters that lead to SoS images with the smallest mean RMSE over all phantoms and both, the low and high noise situation. Thereby, the RMSE was determined relative to the ground truth given by the known spatial distribution of the compartments seen on the B-mode images, in combination with the reference SoS values of the different compartments. The sets of optimal parameters are summarized in table 3.2. The SoS images that were reconstructed with this set of optimal parameters are shown in Fig 3.7 a). To aid a more quantitative assessment of the reconstructed SoS images, the mean SoS and standard deviation of each segment are shown in Fig. 3.7 b).

In the case of low phase noise, both regularization approaches result in SoS images that represent the true SoS distribution fairly well. The SG regularization, however, leads to a higher variation of SoS inside the different segments, reflected by the larger standard deviation in Fig. 3.7 b). With the SG regularization, the high noise leads to an increase in the level of artifacts, most pronounced in the L compartment. Furthermore, the stronger phase noise also biases the mean SoS of the various compartments, most pronounced in the L compartment of phantom 1 and the M compartment in all phantoms.

On the contrary, in case of the SP regularization, the reconstructed SoS agrees very well with the ground truth, independent of the phase noise.

3.3.3 In-vivo results

Since no ground truth SoS is available in-vivo, an optimization study to find the optimal regularization parameters as it has been done in the simulation and phantom experiments is difficult. Anyhow, since we explicitly designed the phantom experiment (geometry, SoS contrast, mimicked phase noise) similar to what we expect

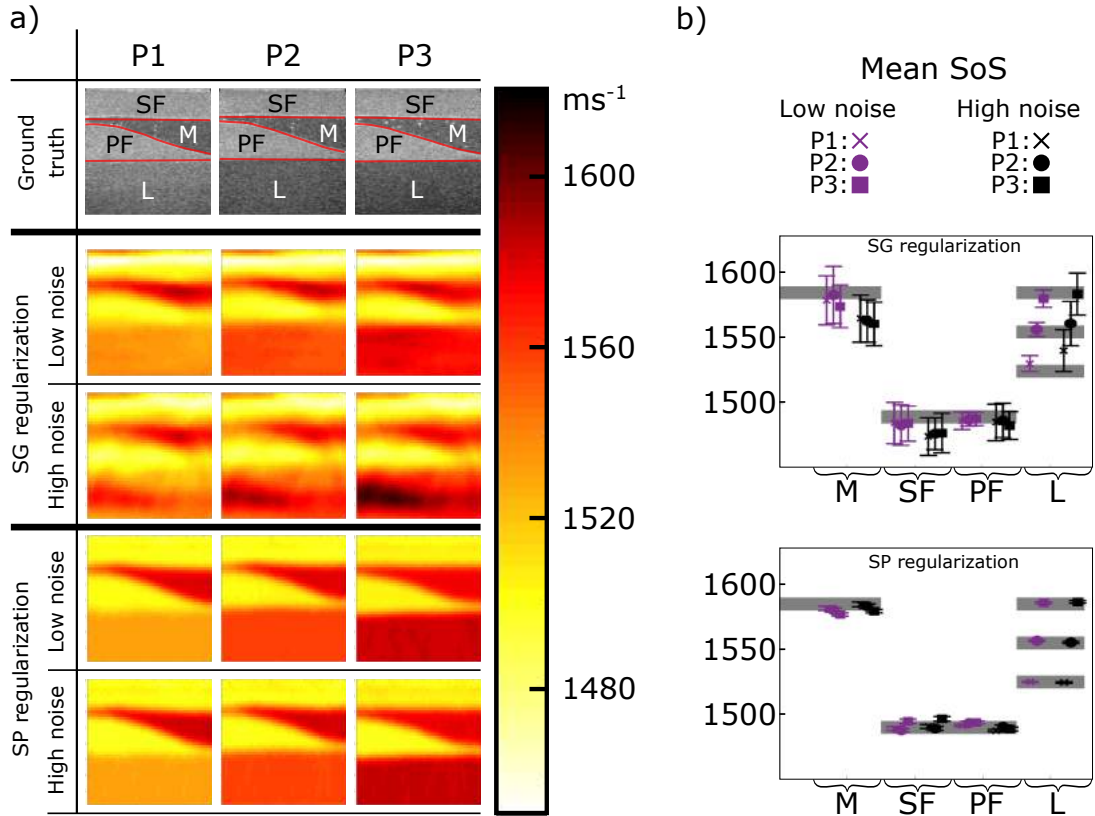


Figure 3.7: Phantom results: a) The top row shows the B-Mode images where the red lines indicate the segmentations that were used for the SP regularization. The SoS images were reconstructed with only the measured phase noise (low noise) and when adding artificially generated phase noise (high noise) to closely mimic the in-vivo scenario. b) Mean and standard deviation evaluated within individual segments.

also in-vivo, the regularization parameters were chosen equal to the parameters that were already used in the phantom study (see table. 3.2).

To investigate whether artifacts in the SoS images are caused by phase noise or by the anatomical structure e.g. via violation of the straight-ray approximation, the liver was imaged three times for each scanning location, but with a slightly changed transducer position. The corresponding B-Mode images are shown in Fig. 3.8a, where the red lines indicate the segmentations that were used for the SP regularization. The SoS images reconstructed with the SG and SP regularization are shown directly below the B-Mode images. To aid a quantitative comparison between the SoS images, the mean SoS values inside the liver were evaluated and summarized in Fig. 3.8b. The standard deviations of the liver SoS of each scanning location are represented by error bars.

In case of the SG regularization, the SoS distribution inside the liver is highly non-uniform. Furthermore, the SoS distribution not only varies between different scanning locations, but also within the same scanning location (but slightly shifted transducer position). Fig. 3.8b reveals that the liver's mean SoS is scattered in a range of about 40 ms^{-1} among the different SoS images.

In contrast, SoS images reconstructed with the SP regularization show uniform

SoS distribution inside the liver, as one would expect in a healthy volunteer. Furthermore, the mean SoS of the liver is more consistent among the different scans, scattered in a smaller range of only about 10 ms^{-1} (see Fig. 3.8b bottom).

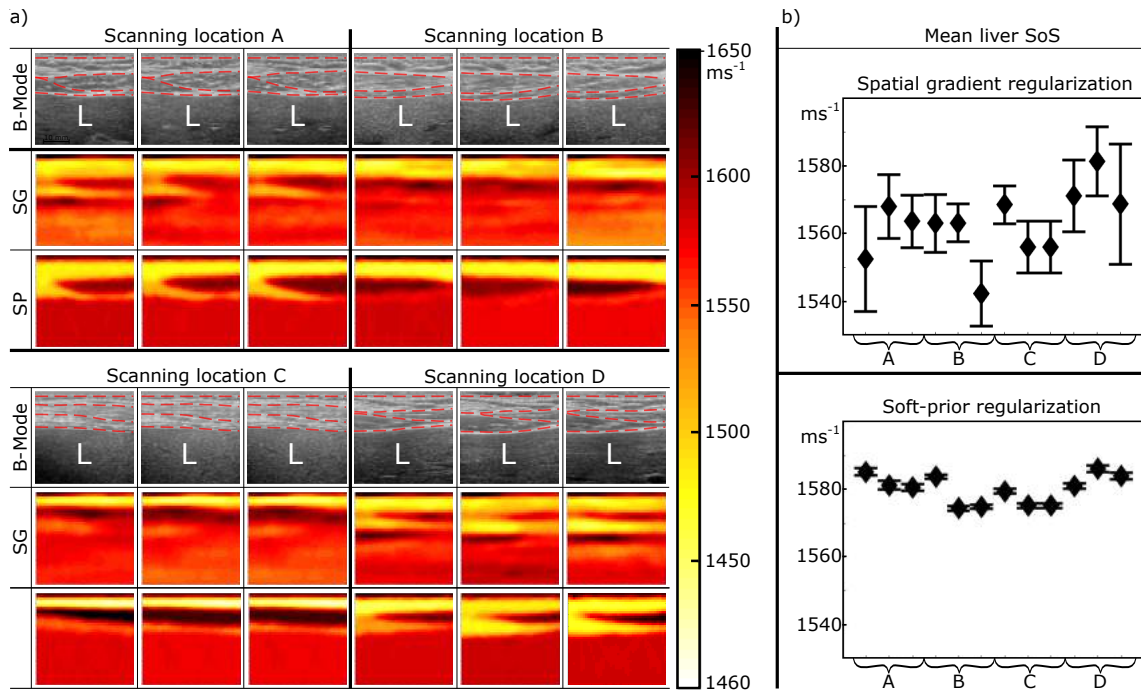


Figure 3.8: a) In-vivo SoS images when accessing the liver from four different scanning locations. At each scanning location, three images were acquired with a slightly changed transducer position. The segmentation that were used for the SP regularization are indicated in the B-Mode images by the red dashed lines. b) Mean SoS and standard deviation of the liver (L) from different scanning location.

3.4 Discussion and Conclusion

In this study, we have shown that the phase noise that is typically observed in-vivo leads to strong artifacts in the SoS images when using a Tikhonov-type regularization of the spatial gradient (SG) for solving the inverse problem. This often leads to SoS images that are not reproducible, when for example repeatedly imaging the same tissue region, and thus makes quantitative interpretation difficult. To overcome this shortcoming, we proposed to use a Bayesian framework for solving the inverse problem. One of the advantages of the Bayesian framework is that it provides a convenient and intuitive way to include an *a priori* statistical model about the distribution of SoS. We have shown in the simulation, phantom experiment and in a first in-vivo study that including geometrical *a priori* information leads to SoS images that are less noise-sensitive and thus is a key step towards quantitative and reproducible SoS imaging in echo-mode.

A further disadvantage of the SG regularization is that it acts across tissue boundaries. This results in a trade-off between a smooth SoS distribution inside tissue

compartments and a high spatial resolution across tissue compartment boundaries. In contrast, the SP regularization acts only within predefined regions and thus allows to minimize SoS variations within predefined regions while retaining good spatial resolution of tissue boundaries in the SoS image.

The *a priori* information that was used for the SP regularization was derived from the B-Mode images, by visually segmenting the different tissue regions. In phantoms, segmentation was not difficult since they consisted of well defined compartments. In-vivo, however, clutter and aberration might result in B-Mode images where a proper identification of certain tissue regions, such as e.g. cancer, turns out to be difficult. The simulations nevertheless revealed that even SoS inhomogeneities that are not included into the *a priori* information can be reconstructed by explicitly allowing pixel-wise SoS variations via the correlation coefficient ρ . On the other hand, a decreased pixel-wise correlation results in SoS images that are more prone to phase noise. This drawback could be circumvented by reducing the phase noise in a first place. Possible approaches might be to use already established techniques that increase the B-Mode image quality such as for example frequency compounding or second harmonic imaging. Recently, an approach has been proposed that focuses at distinct points in emission and reception to build a reflection matrix containing the impulse responses between a set of virtual transducers mapping the entire medium [47]. This allows to apply a local focusing criterion that enables to evaluate the image quality anywhere inside the medium. This approach might be used to identify image regions within which noise is predominant and therefore, no relevant phase information is available. These regions could then be excluded in the formulation of the forward model.

In a clinical situation, the accuracy of the segmentation could be improved if high resolution images obtained from other modalities such as computer tomography or magnetic resonance imaging can be used as *a priori* knowledge.

One important assumption made in this study was the straight ray approximation of US propagation. Although this assumption neglects diffraction and refraction effects, our results demonstrate that the straight ray approximation was reasonable in the sense that correct quantitative results could be obtained. The straight ray approximation has, however, the invaluable advantage that the forward model is linear and can be formulated in matrix notation. Thus, real-time imaging can be obtained when using the SG regularization by pre-calculating the computationally expensive term $(\mathbf{M}^T\mathbf{M} + \gamma\mathbf{D}^T\mathbf{D})^{\text{inv}}$. In the SP approach, a pre-calculation of the posterior covariance matrix is more difficult since it depends on the tissue segmentation which is in principle only available at the time of data acquisition. A possible solution would be the use of a set of posterior covariance matrices, pre-calculated for a set of pre-defined segmentations, with an automated choice based on e.g. a machine learning approach.

Although further clinical evidence is required to draw medically relevant conclusions, the high accuracy of the SoS reconstruction in the phantom results as well as the reproducibility in the in-vivo results are very promising for the diagnosis of fatty liver disease. It has been reported that the mean liver SoS decreases on average by about 40 ms^{-1} in a liver having steatosis of grade 1 (according to the Brunt scale) compared to a healthy liver [24, 25]. This underlines the value of the SP regularization for improving the diagnostic sensitivity of CUTE in fatty liver disease. Apart from liver imaging, a broad range of potential applications for CUTE can be envisaged, as e.g. the diagnosis of cancer or the assessment of plaque inside the carotid artery.

Acknowledgement

This research was funded in part by the Swiss National Science Foundation (project number 205320_178038) and the European Union’s Horizon 2020 research and innovation programme under grant agreement No 732411, Photonics Private Public Partnership, and is supported by the Swiss State Secretariat for Education, Research and Innovation (SERI) under contract number 16.0162. The opinions expressed and arguments employed herein do not necessarily reflect the official view of the Swiss Government.

Data availability

The experimental data used in this study are available on request from the corresponding Author.

References

- [1] J. Baker, P. J. Kornguth, M. S. Soo, R. Walsh, and P. Mengoni, “Sonography of solid breast lesions: observer variability of lesion description and assessment.,” *AJR. American journal of roentgenology*, vol. 172, no. 6, pp. 1621–1625, 1999.
- [2] K. Konno, H. Ishida, M. Sato, T. Komatsuda, J. Ishida, H. Naganuma, Y. Hamashima, and S. Watanabe, “Liver tumors in fatty liver: difficulty in ultrasonographic interpretation,” *Abdominal imaging*, vol. 26, no. 5, pp. 487–491, 2001.
- [3] G. Rahbar, A. C. Sie, G. C. Hansen, J. S. Prince, M. L. Melany, H. E. Reynolds, V. P. Jackson, J. W. Sayre, and L. W. Bassett, “Benign versus malignant solid breast masses: Us differentiation,” *Radiology*, vol. 213, no. 3, pp. 889–894, 1999.

- [4] A. Athanasiou, A. Tardivon, M. Tanter, B. Sigal-Zafrani, J. Bercoff, T. Defieux, J.-L. Gennisson, M. Fink, and S. Neuenschwander, “Breast lesions: quantitative elastography with supersonic shear imaging—preliminary results,” *Radiology*, vol. 256, no. 1, pp. 297–303, 2010.
- [5] J. Bamber, D. Cosgrove, C. Dietrich, J. Fromageau, J. Bojunga, F. Calliada, V. Cantisani, J.-M. Correas, M. D’onofrio, E. Drakonaki, *et al.*, “EfsUMB guidelines and recommendations on the clinical use of ultrasound elastography. part 1: Basic principles and technology,” *Ultraschall in der Medizin-European Journal of Ultrasound*, vol. 34, no. 02, pp. 169–184, 2013.
- [6] R. G. Barr, “Real-time ultrasound elasticity of the breast: initial clinical results,” *Ultrasound quarterly*, vol. 26, no. 2, pp. 61–66, 2010.
- [7] D. Cosgrove, F. Piscaglia, J. Bamber, J. Bojunga, J.-M. Correas, O. Gilja, A. Klauser, I. Sporea, F. Calliada, V. Cantisani, *et al.*, “EfsUMB guidelines and recommendations on the clinical use of ultrasound elastography. part 2: Clinical applications,” *Ultraschall in der Medizin-European Journal of Ultrasound*, vol. 34, no. 03, pp. 238–253, 2013.
- [8] C. F. Dietrich, J. Bamber, A. Berzigotti, S. Bota, V. Cantisani, L. Castera, D. Cosgrove, G. Ferraioli, M. Friedrich-Rust, O. H. Gilja, *et al.*, “EfsUMB guidelines and recommendations on the clinical use of liver ultrasound elastography, update 2017 (long version),” *Ultraschall in der Medizin-European Journal of Ultrasound*, vol. 38, no. 04, pp. e16–e47, 2017.
- [9] R. M. Sigrist, J. Liao, A. El Kaffas, M. C. Chammas, and J. K. Willmann, “Ultrasound elastography: review of techniques and clinical applications,” *Theranostics*, vol. 7, no. 5, p. 1303, 2017.
- [10] S. Hu and L. V. Wang, “Photoacoustic imaging and characterization of the microvasculature,” *Journal of biomedical optics*, vol. 15, no. 1, p. 011101, 2010.
- [11] M. Jaeger, D. C. Harris-Birtill, A. G. Gertsch-Grover, E. O’Flynn, and J. C. Bamber, “Deformation-compensated averaging for clutter reduction in epiphotoacoustic imaging in vivo,” *Journal of biomedical Optics*, vol. 17, no. 6, p. 066007, 2012.
- [12] K. G. Held, M. Jaeger, J. Rička, M. Frenz, and H. G. Akarçay, “Multiple irradiation sensing of the optical effective attenuation coefficient for spectral correction in handheld oa imaging,” *Photoacoustics*, vol. 4, no. 2, pp. 70–80, 2016.
- [13] L. Ulrich, L. Ahnen, H. Akarçay, S. Sanchez, M. Jaeger, G. Held, M. Wolf, and M. Frenz, “Spectral correction for handheld optoacoustic imaging by means of near-infrared optical tomography in reflection mode,” 08 2018.

- [14] J. Wiskin, D. Borup, S. Johnson, and M. Berggren, “Non-linear inverse scattering: High resolution quantitative breast tissue tomography,” *The Journal of the Acoustical Society of America*, vol. 131, no. 5, pp. 3802–3813, 2012.
- [15] G. Sandhu, C. Li, O. Roy, S. Schmidt, and N. Duric, “Frequency domain ultrasound waveform tomography: breast imaging using a ring transducer,” *Physics in Medicine & Biology*, vol. 60, no. 14, p. 5381, 2015.
- [16] J. Wiskin, B. Malik, R. Natesan, and M. Lenox, “Quantitative assessment of breast density using transmission ultrasound tomography,” *Medical physics*, vol. 46, no. 6, pp. 2610–2620, 2019.
- [17] M. Kondo, K. Takamizawa, M. Hiram, K. Okazaki, K. Inuma, and Y. Takehara, “An evaluation of an in vivo local sound speed estimation technique by the crossed beam method,” *Ultrasound in Medicine and Biology*, vol. 16, no. 1, pp. 65–72, 1990.
- [18] I. Céspedes, J. Ophir, and Y. Huang, “On the feasibility of pulse-echo speed of sound estimation in small regions: Simulation studies,” *Ultrasound in Medicine and Biology*, vol. 18, no. 3, pp. 283–291, 1992.
- [19] M. C. Hesse, L. Salehi, and G. Schmitz, “Nonlinear simultaneous reconstruction of inhomogeneous compressibility and mass density distributions in unidirectional pulse-echo ultrasound imaging,” *Physics in Medicine and Biology*, vol. 58, no. 17, p. 6163, 2013.
- [20] M. Jakovljevic, S. Hsieh, R. Ali, G. Chau Loo Kung, D. Hyun, and J. J. Dahl, “Local speed of sound estimation in tissue using pulse-echo ultrasound: Model-based approach,” *The Journal of the Acoustical Society of America*, vol. 144, no. 1, pp. 254–266, 2018.
- [21] S. J. Sanabria, E. Ozkan, M. Rominger, and O. Goksel, “Spatial domain reconstruction for imaging speed-of-sound with pulse-echo ultrasound: simulation and in vivo study,” *Physics in Medicine & Biology*, vol. 63, no. 21, p. 215015, 2018.
- [22] L. Ruby, S. J. Sanabria, K. Martini, K. J. Dedes, D. Vorbürger, E. Oezkan, T. Frauenfelder, O. Goksel, and M. B. Rominger, “Breast cancer assessment with pulse-echo speed of sound ultrasound from intrinsic tissue reflections: Proof-of-concept,” *Investigative radiology*, vol. 54, no. 7, pp. 419–427, 2019.
- [23] A. S. Podkova and M. L. Oelze, “The convolutional interpretation of registration-based plane wave steered pulse-echo local sound speed estimators,” *Physics in Medicine & Biology*, vol. 65, no. 2, p. 025003, 2020.

- [24] M. Imbault, A. Faccinnetto, B.-F. Osmanski, A. Tissier, T. Deffieux, J.-L. Gennisson, V. Vilgrain, and M. Tanter, “Robust sound speed estimation for ultrasound-based hepatic steatosis assessment,” *Physics in Medicine and Biology*, vol. 62, no. 9, p. 3582, 2017.
- [25] M. D. Burgio, M. Imbault, M. Ronot, A. Faccinnetto, B. E. Van Beers, P.-E. Rautou, L. Castera, J.-L. Gennisson, M. Tanter, and V. Vilgrain, “Ultrasonic adaptive sound speed estimation for the diagnosis and quantification of hepatic steatosis: a pilot study,” *Ultraschall in der Medizin-European Journal of Ultrasound*, vol. 40, no. 06, pp. 722–733, 2019.
- [26] M. Jaeger, G. Held, S. Peeters, S. Preisser, M. Grünig, and M. Frenz, “Computed ultrasound tomography in echo mode for imaging speed of sound using pulse-echo sonography: proof of principle,” *Ultrasound in medicine and biology*, vol. 41, no. 1, pp. 235–250, 2015.
- [27] T. Loupas, J. Powers, and R. W. Gill, “An axial velocity estimator for ultrasound blood flow imaging, based on a full evaluation of the doppler equation by means of a two-dimensional autocorrelation approach,” *IEEE transactions on ultrasonics, ferroelectrics, and frequency control*, vol. 42, no. 4, pp. 672–688, 1995.
- [28] C. Kasai, K. Namekawa, A. Koyano, and R. Omoto, “Real-time two-dimensional blood flow imaging using an autocorrelation technique,” *IEEE Transactions on sonics and ultrasonics*, vol. 32, no. 3, pp. 458–464, 1985.
- [29] P. Stähli, M. Kuriakose, M. Frenz, and M. Jaeger, “Improved forward model for quantitative pulse-echo speed-of-sound imaging,” *Ultrasonics*, p. 106168, 2020.
- [30] A. Tarantola and B. Valette, “Generalized nonlinear inverse problems solved using the least squares criterion,” *Reviews of Geophysics*, vol. 20, no. 2, pp. 219–232, 1982.
- [31] M. Jaeger and M. Frenz, “Quantitative imaging of speed of sound in echo ultrasonography.” IEEE International Ultrasound Symposium, Taipei, 2015.
- [32] W. P. Gouveia and J. A. Scales, “Bayesian seismic waveform inversion: Parameter estimation and uncertainty analysis,” *Journal of Geophysical Research: Solid Earth*, vol. 103, no. B2, pp. 2759–2779, 1998.
- [33] A. Malinverno, “A bayesian criterion for simplicity in inverse problem parametrization,” *Geophysical Journal International*, vol. 140, no. 2, pp. 267–285, 2000.

- [34] K. Mosegaard and A. Tarantola, “Monte carlo sampling of solutions to inverse problems,” *Journal of Geophysical Research: Solid Earth*, vol. 100, no. B7, pp. 12431–12447, 1995.
- [35] A. P. Valentine and M. Sambridge, “Optimal regularization for a class of linear inverse problem,” *Geophysical Journal International*, vol. 215, no. 2, pp. 1003–1021, 2018.
- [36] F. M. Hooi and P. L. Carson, “First-arrival traveltime sound speed inversion with a priori information,” *Medical physics*, vol. 41, no. 8Part1, p. 082902, 2014.
- [37] P. Stähli, M. Frenz, and M. Jaeger, “Reflection-mode speed-of-sound imaging using soft-prior limits,” in *2019 IEEE International Ultrasonics Symposium (IUS)*, pp. 948–950, IEEE, 2019.
- [38] A. Tarantola, *Inverse problem theory and methods for model parameter estimation*, vol. 89. siam, 2005.
- [39] A. H. Golnabi, P. M. Meaney, S. D. Geimer, and K. D. Paulsen, “Comparison of no-prior and soft-prior regularization in biomedical microwave imaging,” *Journal of Medical Physics/Association of Medical Physicists of India*, vol. 36, no. 3, p. 159, 2011.
- [40] M. McGarry, C. L. Johnson, B. P. Sutton, E. E. Van Houten, J. G. Georgiadis, J. B. Weaver, and K. D. Paulsen, “Including spatial information in nonlinear inversion mr elastography using soft prior regularization,” *IEEE transactions on medical imaging*, vol. 32, no. 10, pp. 1901–1909, 2013.
- [41] J. Feng, S. Jiang, Y. Zhao, J. Xu, S. C. Davis, B. W. Pogue, and K. D. Paulsen, “Direct soft prior regularization in nir spectral tomography from mri-contrast and distance-constraints, for segmentation-free reconstruction,” in *Cancer Imaging and Therapy*, pp. JM3A–4, Optical Society of America, 2016.
- [42] U. Vyas and D. Christensen, “Ultrasound beam simulations in inhomogeneous tissue geometries using the hybrid angular spectrum method,” *IEEE transactions on ultrasonics, ferroelectrics, and frequency control*, vol. 59, no. 6, pp. 1093–1100, 2012.
- [43] E. L. Madsen, J. A. Zagzebski, and G. R. Frank, “An anthropomorphic ultrasound breast phantom containing intermediate-sized scatterers,” *Ultrasound in Medicine and Biology*, vol. 8, no. 4, pp. 381–392, 1982.
- [44] E. Madsen, G. Frank, T. Krouskop, T. Varghese, F. Kallel, and J. Ophir, “Tissue-mimicking oil-in-gelatin dispersions for use in heterogeneous elastography phantoms,” *Ultrasonic imaging*, vol. 25, no. 1, pp. 17–38, 2003.

- [45] E. L. Madsen, M. A. Hobson, G. R. Frank, H. Shi, J. Jiang, T. J. Hall, T. Varghese, M. M. Doyley, and J. B. Weaver, “Anthropomorphic breast phantoms for testing elastography systems,” *Ultrasound in medicine and biology*, vol. 32, no. 6, pp. 857–874, 2006.
- [46] M. M. Nguyen, S. Zhou, J.-l. Robert, V. Shamdasani, and H. Xie, “Development of oil-in-gelatin phantoms for viscoelasticity measurement in ultrasound shear wave elastography,” *Ultrasound in medicine and biology*, vol. 40, no. 1, pp. 168–176, 2014.
- [47] W. Lambert, L. A. Cobus, M. Couade, M. Fink, and A. Aubry, “Reflection matrix approach for quantitative imaging of scattering media,” *arXiv preprint arXiv:1911.03147*, 2019.

Chapter 4

Receive beam steering and clutter reduction for imaging the speed-of-sound inside the carotid artery

MAJU KURIAKOSE¹, JAN-WILLEM MULLER², PATRICK STÄHLI¹, MARTIN FRENZ¹ AND MICHAEL JAEGER¹

Abstract

Handheld imaging of the tissue's speed-of-sound (SoS) is a promising multimodal addition to diagnostic ultrasonography for the examination of tissue composition. Computed ultrasound tomography in echo mode (CUTE) probes the spatial distribution of SoS, conventionally via scanning the tissue under a varying angle of ultrasound transmission, and quantifying – in a spatially resolved way – phase variations of the beamformed echoes. So far, this technique is not applicable to imaging the lumen of vessels, where blood flow and tissue clutter inhibit phase tracking of the blood echoes. With the goal to enable the assessment of atherosclerotic plaque composition inside the carotid artery, we propose two modifications to CUTE: (a) receive (Rx) beam-steering as opposed to transmit (Tx) beam-steering to increase acquisition speed and to reduce flow-related phase decorrelation, and (b) pairwise subtraction of data obtained from repetitions of the scan sequence, to highlight blood echoes relative to static echo clutter and thus enable phase tracking of blood echoes. These modifications were tested in a phantom study, where the echogenicity of the vessel lumen was chosen similar to the one of the background medium, which allows a direct comparison of SoS images obtained with the different techniques. Our results demonstrate that the combination of Rx-steering with the subtraction technique results in a SoS image of the same quality as obtained with conventional Tx-steering. Together with the improved acquisition speed this makes the proposed technique a key step towards successful imaging of the SoS inside the carotid artery.

The work presented in this chapter has been published in the *Journal of Imaging* in 2018. doi:10.3390/jimaging4120145.

¹Institute of Applied Physics, University of Bern, Sidlerstrasse 5, 3012 Bern, Switzerland

²Department of Biomedical Engineering, Eindhoven University of Technology, PO box 513, 5600 MB Eindhoven, The Netherlands

4.1 Introduction

Reliable imaging techniques for non-invasive tissue characterization are important in clinical practice for the accurate assessment of pathological and physiological abnormalities. For this purpose, multimodal imaging is often preferred over single mode imaging because it provides complementary information on a variety of different tissue parameters. On the downside, multimodal imaging can be expensive, time consuming, tedious for patients, and can suffer from image registration problems that limit the diagnostic accuracy. A promising way to overcome such drawbacks is by using a single imaging device, and extract complementary multimodal information via different ways of data acquisition/processing. Echo ultrasound (US) is already used as quick, simple and cost-effective imaging technique in many areas. To improve the diagnostic accuracy in a multimodal approach, it has recently been combined with US elastography, which allows analyzing the tissue’s elastic properties [1–4]. Optoacoustic imaging, which shows blood oxygen saturation [5–7], lipid pools [8, 9] or exogenous molecular probes [10] has been implemented as an addition to conventional US [11–13] with promise for e.g. cancer diagnosis [14, 15]. In a similar multimodal approach, our goal is to complement the classical B-mode display of echo intensity with an image of the spatial distribution of the tissue’s speed of sound (SoS), both derived from pulse-echo data. The SoS fundamentally depends on the tissue’s compressibility and density and thus a spatially resolved quantification of this parameter will help identifying abnormalities in tissue compositions [16, 17]. The diagnostic potential of imaging SoS has been thoroughly demonstrated in through-transmission ultrasound tomography [18–25]. In addition, various reflection-mode techniques have been investigated [26–28]. We recently developed a reflection-mode technique, named computed ultrasound tomography in echo-mode (CUTE) [29, 30], which allows to determine the SoS with high spatial and contrast resolution in real time. The data acquisition and reconstruction scheme of CUTE involves the following steps: (1) transmit (Tx) US plane waves over a range of angles (by beam steering) to a region of interest, and receive (Rx) the echoes from acoustic scatterers. (2) Assuming an average SoS, reconstruct (beam-form) the echoes back to the hypothetical locations of the ultrasound scatterers, using e.g., delay-and-sum (DAS) beamforming. (3) Detect the local echo phase shift from the beamformed echoes in-between successive Tx angles and (4) finally, reconstruct the SoS image from the phase shift maps. This technique is based on the following rationale: if the actual SoS inside the tissue agrees with the assumed value, the round-trip times in the DAS beamforming are correctly anticipated. Then, the phase of the reconstructed echoes does not depend on the Tx angle, and the phase shift is zero independent of location and angle pair. If, however, the spatial distribution of SoS deviates from the assumed value, it produces a corresponding phase

shift due to the non-anticipated round-trip time delay of the Tx transients. Using the relation between SoS and phase shift, the spatial distribution of SoS can then be reconstructed by solving the corresponding inverse problem either in Fourier [29] or spatial domain [31]. A classic use of US sonography is for diagnosing atherosclerosis [32, 33] in the carotid arteries. Plaques in their advanced stage may contain cellular or acellular fibrous tissues, lymphocytic inflammatory infiltrate, foam cells, pultaceous debris (lipid-rich core), and calcific deposits. US sonography is used for assessing plaque neovascularization, thickening of inner lining of vessel walls and plaque formation. Future cardiovascular events or mortality risks can be predicted by quantifying the total number of plaques [34] and plaque area or volume [35]. In addition, echogenicity is used to categorize plaques into echo-lucent, predominantly echo-lucent, predominantly echogenic and echogenic: Pathomorphologic studies in relation to US echogenicity suggest that low risk “stable” plaques mainly consist of fibrous or calcified tissues, which appear as echogenic, while high risk plaques appear as heterogeneous or translucent [36, 37]. Nevertheless, the accuracy of the B-mode US is still not satisfactory, and thus it is nowadays combined with US elastography to improve the diagnostic accuracy. Continuing this multimodal approach, CUTE is promising to aid the assessment of atherosclerotic plaque rupture risk: Lipids, fibrous and calcified tissue have different SoS, thus quantifying SoS will provide complementary information on plaque composition. The conventional way how CUTE is performed, however, inhibits its application to the carotid artery for two reasons:

1. Blood motion: In conventional CUTE, Tx plane waves are sent forth to scan the full angular aperture that is possible within the limits of the transducer design, e.g., from -25° to 25° . For maintaining low clutter levels, synthetic Tx focusing is used, based on coherent plane wave compounding [38] of acquisitions with finely spaced (e.g. 0.5°) Tx angles. Therefore, conventional CUTE typically requires more than 100 acquisitions. During the time required for this number of acquisitions, arterial blood flow leads to decorrelation of blood echoes, resulting in phase noise and SoS artefacts.
2. Tissue clutter: Higher order echoes from the tissue surrounding the carotid are interpreted as originating from inside the carotid, cluttering the blood echoes. Clutter has a higher intensity level than the blood echoes, leading to wrong echo phase shifts and thus falsified SoS reconstruction

Here, we propose two modifications to the CUTE methodology that solve these problems and will be an important step towards enabling imaging the SoS inside the carotid artery:

	Tx steering	full Rx	fast Rx
Tx angles	$\Phi = -25^\circ : 2.5^\circ : 25^\circ$	$\Phi = 0^\circ$	$\Phi = 0^\circ$
Tx aperture	$\Phi_{\text{rad}} = 2.5^\circ, 0.5^\circ$ steps	$\Phi_{\text{rad}} = 5^\circ, 0.5^\circ$ steps	$\Phi_{\text{rad}} = 2.5^\circ, 2.5^\circ$ steps
Rx angles	$\Psi = 0^\circ$	$\Psi = -25^\circ : 2.5^\circ : 25^\circ$	$\Psi = -25^\circ : 2.5^\circ : 25^\circ$
Rx aperture	$\Psi_{\text{rad}} = 5^\circ$	$\Psi_{\text{rad}} = 2.5^\circ$	$\Psi_{\text{rad}} = 2.5^\circ$
CUTE angles	$\Phi_{\text{cute}} = -25^\circ : 10^\circ : 25^\circ$	$\Psi_{\text{cute}} = -25^\circ : 10^\circ : 25^\circ$	$\Psi_{\text{cute}} = -25^\circ : 10^\circ : 25^\circ$

Table 4.1: Experimental parameters used for Tx and Rx steering

1. Rx instead of Tx beam steering for echo phase tracking, in order to reduce acquisition time and thus avoid/reduce blood flow-related artefacts. This approach is inspired by the commonly accepted principle of the reciprocity of sender and receiver, suggesting the equivalence of Tx- and Rx-steering.
2. Take benefit of blood motion to reduce clutter: Pairwise subtraction of consecutive repetitions of the signal acquisition, spaced by small (on the order of a ms) time intervals, cancels static tissue clutter and thereby highlights the decorrelating weak blood echoes.

The present phantom study demonstrates that the proposed modifications do not substantially alter the phase shift maps nor the final SoS image, compared to the conventional Tx-steering approach, making them a promising step towards SoS imaging inside the carotid artery.

4.2 Materials and Methods

This chapter starts with a description of conventional CUTE and of the proposed novel modifications. Although this description uses the exact acquisition parameters used in this study, it is, however, intended to be interpreted in a more general way, and different parameters may be found suitable for other specific applications (depending on hardware/sample properties). The acquisition parameters employed in this study are summarized in Table 4.1.

4.2.1 Conventional Tx CUTE

For conventional Tx-steering CUTE, US images were acquired for Tx steering angles ranging from -25° to 25° with a 2.5° angle step ($\Phi = -25^\circ:2.5^\circ:25^\circ$). The choice of the angle range corresponds to the desired tracking angle range. The angle limits are defined by the directional response of the transducer elements and by the element pitch. The angle step is chosen small enough to avoid phase aliasing caused by SoS variations. For Rx beamforming, an angular aperture with radius $\Psi_{\text{Rad}} = 5^\circ$ was used, centred on the Rx angle $\Psi = 0^\circ$. To generate images with a clutter level enabling robust phase tracking, focusing is required in Tx. One way to achieve Tx focusing is to scan the sample with an actually focused beam (line-by-line scan),

which however results in an unnecessarily large number of acquisitions especially as multiple focal depths are required. A far more efficient way to achieve Tx focusing is coherent plane-wave compounding. This was done for each tracking angle, from a group of plane-wave acquisitions centred on the respective tracking angle with a Tx aperture radius $\Phi \text{ rad} = 2.5^\circ$ and a 0.5° step size. This resulted in a total plane wave Tx angle range of $[-27.5^\circ:0.5^\circ:27.5^\circ]$, i.e. 111 acquisitions. The coherently compounded images, 11 in total, were then used for phase tracking.

4.2.2 Full-Rx CUTE

Rx tracking can be implemented in a very similar way to the conventional Tx tracking, by interchanging the Tx and Rx parameters. The Rx angular aperture of the conventional approach was thus replaced by an identical Tx angular aperture in the Rx approach. For this purpose, plane wave acquisitions were performed with Tx angles ranging within an aperture radius $\Phi \text{ rad} = 5^\circ$ centred around $\Phi = 0^\circ$ at 0.5° step size, resulting in 21 acquisitions. This already provides a factor 5 reduction in acquisition time, reducing blood-flow and tissue-motion related phase tracking errors. For each Tx angle, a set of 21 Rx-steered images was reconstructed, using steering angles ($\Psi = -25^\circ:2.5^\circ:25^\circ$) with an Rx angular aperture radius $\Psi \text{ rad} = 2.5^\circ$, resulting in 21 times 21 Tx- and Rx-steered plane wave images. Then, synthetic Tx focusing was achieved for each Rx-steering angle separately, by coherently compounding over the 21 different Tx angles, resulting in the desired 21 Rx-steered (and Tx-focused) images for phase tracking. This approach, where the Rx aperture of conventional CUTE is replaced with a quasi-continuous Tx aperture in the Rx-steering approach, is hereafter termed as 'full-Rx CUTE'.

4.2.3 Fast-Rx subtraction technique

Preliminary in-vivo results of carotid imaging indicate that the total time needed for all acquisitions in full-Rx CUTE is still too long, resulting in substantial flow-related echo decorrelation during scanning the Tx angle range and thus to phase noise in the coherently compounded images. Such flow-related decorrelation can be reduced by a further reduction of the number of Tx angles. Reducing the number of Tx angles on the other hand increases phase noise, caused by clutter stemming from tissue surrounding the artery, which obscures the comparably weak blood echoes. To solve this problem, we propose to make use of the blood flow: multiple data sets (each containing the same Tx angle range) are acquired, with a long enough time delay in-between consecutive repetitions allowing the blood echoes to decorrelate while echoes from surrounding tissue remain static. By subtracting successive data sets, stationary tissue clutter is reduced (ideally to zero), whereas the decorrelating blood echoes remain visible. The important point here is that blood echo decor-

relation occurs in-between data sets, but not substantially within each data set. Preliminary in-vivo results indicated that a number of 5 acquisitions per data set is sufficiently small to reduce blood echo decorrelation to an acceptable level. For our phantom study, we therefore used a Tx angle step of 2.5° , resulting in a total of 5 angles distributed over the desired Tx angle range from -5° to 5° .

The subtraction technique can only provide echoes from inside the vessel, not from the surrounding static tissue. To allow phase shift tracking over the whole image area, the segmented echoes from inside the blood vessel, obtained with the fast-Rx subtraction approach, were therefore combined with the echoes from the surrounding tissue, obtained with the full-Rx approach.

4.2.4 Phantom description

The experiments were conducted using an agar-cellulose phantom, where agar formed the gel network and cellulose provided echogenicity for US. This phantom consisted of a background with uniform SoS, into which a movable cylindrical inclusion was inserted having a positive SoS contrast compared to the background. The inclusion had a diameter of 7 mm and was placed at 10 mm depth below the phantom surface (Fig. 4.1) to imitate a carotid artery. Blood flow was simulated by manually moving the inclusion.

The phantom was prepared by slowly adding 2 wt% of agar powder (Sigma–Aldrich, Germany) and 2 wt% of cellulose powder (20-micrometer, Sigma–Aldrich, Germany) into continually stirred deionized water at room temperature to avoid lumps. The solution was heated above 80°C (melting temperature of agar) and degassed by exposing it to a vacuum level of about 0.1 atm for about 5 minutes. After cooling down to about 40°C , ethanol (1 vol%) was added for adjusting the SoS of the background to the desired value of 1490 m/s. This final solution was poured (while still at 40°C) into a pre-cooled mould, which contained a removable steel rod with 7 mm diameter at the location where the cylindrical inclusion was to be inserted later on. The mould was then quickly cooled down below the gelation temperature (30°) to minimise sedimentation of cellulose during gelation. All experiments were performed at ambient temperature (22°C). In a different mould, a cylindrical inclusion with 7 mm diameter was prepared with 2% cellulose following the same procedure and by adding 5 vol.% of ethanol to generate a positive SoS contrast (SoS=1540 m/s). The cylindrical inclusion was inserted into the background sample only for the time of the experiment to avoid diffusion of ethanol between the inclusion and the background, which would else level off the SoS contrast.

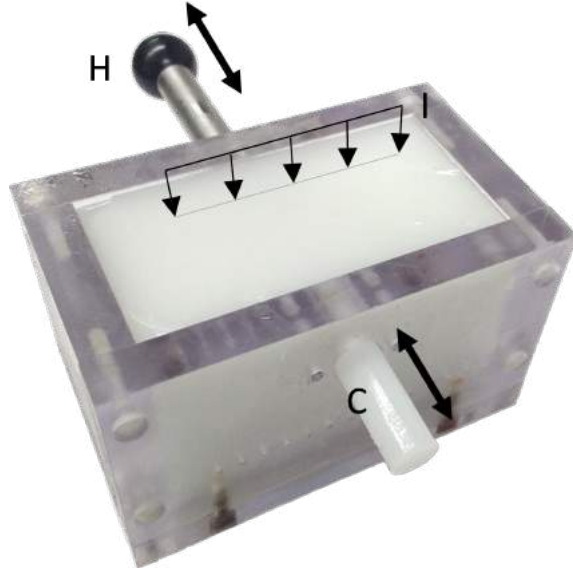


Figure 4.1: Photograph of the phantom, indicating the location of the imaging plane I. The artery-mimicking cylindrical inclusion C could be manually moved by moving the handle H.

4.2.5 Acquisition system

The experiments were performed using a Vantage 64 LE ultrasound system (Verasonics, Redmond, WA, USA). The ultrasound probe was a Philips L12-5 linear array probe (ATL Bothell, WA, USA) having a 0.19 mm element pitch. Matlab (The MathWorks, MA, USA) software was used to program the acquisition and the off-line image reconstruction. The probe was placed on the top surface of the phantom with the imaging plane aligned perpendicular to the cylindrical inclusion (Fig. 4.1). The transducer was driven at 9 MHz transmit centre frequency. Raw radio-frequency (rf) data were collected with a fourfold sampling frequency of 36 MHz.

4.2.6 US image reconstruction and phase tracking

The signal processing starts with the conversion of the rf data into reconstructed complex rf (crf) mode images applying the Hilbert transformation followed by DAS beamforming. An important prerequisite for proving the experimental equivalence between Tx- and Rx-steering is the mathematical equivalence of the implementation of the DAS algorithms. In both the Tx- and the Rx-CUTE approaches, Tx beamforming was achieved via coherent compounding of plane wave transmission data. Conventionally, Rx-beamforming is implemented via summation over subsets of transducer elements. This approach is, however, not mathematically equivalent to plane wave compounding, as the elements have spherical/cylindrical receiving fields as opposed to the plane transmitted fields. To achieve mathematical equivalence, we therefore implemented an adapted way of DAS beamforming, consisting of two stages: In a first stage, the element-wise rf data was converted to receive

angle-wise rf data, using a DAS algorithm with linear delay profiles (as opposed to focused delay profiles) and summation over the full array aperture as done in a classical phased-array sector scan. This was done for delay profiles corresponding to Rx angles ranging from -27.5° to 27.5° in 0.5° steps, resulting in receiving fields that were identical with the transmitting fields used for synthetic Tx beamforming. In a second stage, the angle-wise rf data was coherently compounded over the desired Rx angular apertures. Echo phase shift maps were obtained using Loupas-type phase correlation [39]: The crf image at the n -th tracking angle was point-wise multiplied with the complex conjugate of the crf mode image at the adjacent $(n+1)$ -th angle. The complex product was convolved with a spatial low-pass filter kernel having dimensions of 1 mm by 1 mm. The phase angle of the filtered complex product was regarded as proportional to the spatially-resolved, non-anticipated time-of-flight (ToF) differences along the different tracking angles (phase shift map). Any deviation of the medium's SoS from the assumed value c_0 would result in non-zero phase shift values.

4.2.7 SoS image reconstruction

For SoS reconstruction, groups of two adjacent phase shift maps were summed up, to obtain phase shift maps for a reduced number of final tracking angles, i.e. $[-25^\circ:10^\circ:25^\circ]$. The step size of 10° was a compromise between artefact level and numerical efficiency of SoS reconstruction: In our experience, SoS artefacts typically decrease with increasing number of angles, but converge below a 10° angle step. A linear space domain algorithm was used for SoS image reconstruction, assuming straight ray US propagation: In the forward model, the echo phase shift values were expressed as a function of line integrals of slowness deviation (i.e. the difference between actual slowness and assumed slowness, where the slowness is defined as inverse of SoS) in a system matrix. A Tikhonov pseudo-inverse of the system matrix was calculated, with L2 norm regularization of the slowness gradient, to reconstruct the slowness deviation from the measured phase shift data.

4.3 Results

4.3.1 Tx versus full-Rx CUTE

The first goal of this study was to demonstrate the experimental equivalence between the Tx- and the full Rx-steering approach. Fig. 4.2a and 4.2b show the echo phase shift maps obtained with the two approaches. The images show visually very similar results. A comparison of the rms value of the difference between the phase shifts of the two approaches, with the rms value of the phase shifts of the Tx-steering

approach, yields a ratio of 0.05, quantitatively supporting the close similarity of both results. Fig. 4.2c and 4.2d show the SoS images resulting from the Tx- and the full Rx-steering approach, respectively. Note that the color maps account for an offset of -8 m/s of the full-Rx compared to the Tx result. Apart from this offset, the reconstructed spatial distribution of the SoS looks very similar: Both images reveal the positive SoS contrast at the location of the cylindrical inclusion. Below the inclusion, both techniques show comparable artefacts. These artefacts originate from phase noise due to aberrations (refraction) of US propagating through the inclusion. The disagreement at the upper edge of the image near the transducer aperture can be attributed to phase noise due to element cross-talk, when transmitting on different transducer elements with different time delays. This phase noise plays a different role in the two approaches because of the different Tx angle ranges.

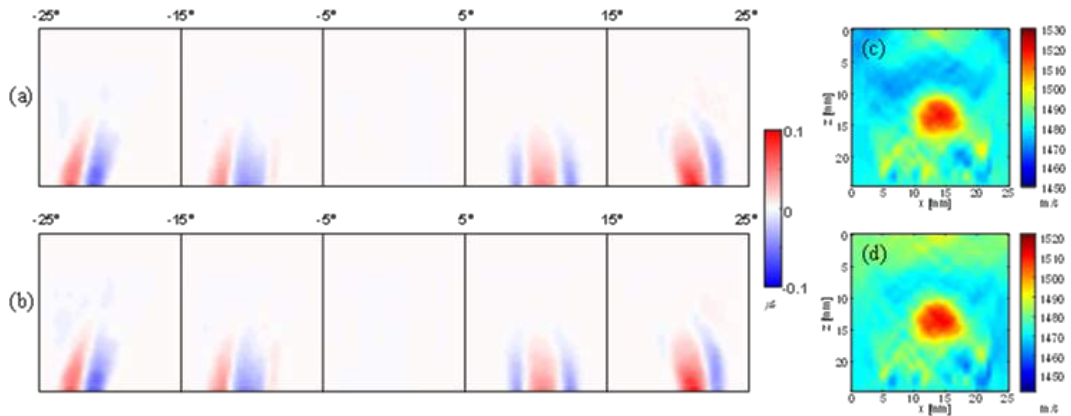


Figure 4.2: Comparison of Conventional Tx and full-Rx steering. (a) Phase shift maps from Tx steering; (b) Phase shift maps from full-Rx steering; (c) SoS image from Tx steering; (e) SoS image from full-Rx steering. Note the 8 m/s difference between the color scales in (c) and (d).

4.3.2 Fast-Rx subtraction technique

Preliminary volunteer results of full-Rx echo phase tracking using 21 Tx angles indicated that even the reduced acquisition time is still long enough that blood echo decorrelation still occurs. To further reduce the acquisition time, the fast-Rx approach reduces the quasi-continuous Tx aperture to only 5 Tx angles. While reducing echo decorrelation, this however results in reduced synthetic Tx focus quality, and thus increased clutter level. This effect is visible in the phantom study, where the angle number reduction led to increased phase noise in the echo phase shift maps (Fig. 4.3a), compared to the full-Rx approach (Fig. 4.3b). As a result, the SoS image shows a high level of artefacts and an inaccurate spatial distribution of SoS inside the inclusion (Fig. 4.3b). Most of the clutter found inside the inclusion area consists of stationary higher-order echoes originating from outside the inclusion. The subtraction technique aims at reducing this stationary clutter via pairwise subtracting consecutively repeated fast-Rx acquisitions. At the same time, blood flow between

the sequence repetitions avoids cancellation of blood echoes, thus highlighting the blood echo intensity compared to stationary echoes. This is illustrated by B-mode US images: Whereas the echogenicity inside the inclusion was slightly lower than in the background in the non-subtracted data (Fig. 4.3c), the subtraction data highlights the echoes from inside the inclusion (Fig. 4.3d). The reduced intensity level of the stationary echoes outside the inclusion results in a reduced relative level of clutter inside the inclusion. The difference data thus allows robust phase tracking inside the inclusion in spite of the reduced number of angles. Outside the inclusion, however, the relative clutter level stays unchanged. To enable echo phase tracking both in- and outside the inclusion, the fast-Rx subtraction data from inside the inclusion is combined with full-Rx data from outside the inclusion. The second goal of this study was to demonstrate that this combination allows reconstructing the SoS in a similar way as when high-quality (full-Rx) echoes would be available also inside the inclusion. The segmentation was achieved by manual selection of centre point and radius of the inclusion area. The fast-Rx subtraction data was scaled with a factor 10 before combination to account for intensity differences. For illustration, Fig. 4.3e shows a B-mode US image resulting from this combination, where an equal echogenicity both in- and outside the lumen area was achieved. Fig. 4.3f shows the SoS image that was reconstructed from the resulting echo phase shift maps. Only minor differences are seen between the spatial distribution of reconstructed SoS in this image, compared to the one obtained with full-Rx CUTE alone (Fig. 4.3d).

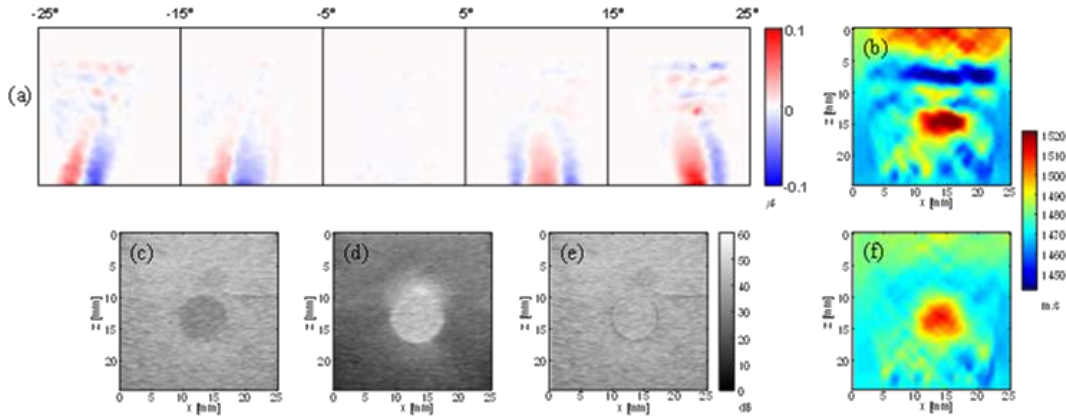


Figure 4.3: (a) Phase shift maps from fast-Rx approach alone; (b) SoS image obtained from the fast-Rx approach without subtraction; (c) B-mode US image from full-Rx data; (d) B-mode US image from subtracted fast-Rx data; (e) Combined B-mode US image; (f) SoS image from combined data. Note that in (c) to (e), the dB scale is normalized to the maximum intensity level in each image.

4.4 Discussion and conclusion

The first part of this study shows that the conventional Tx-steering approach can be substituted by the less time-consuming full-Rx approach (see Fig. 4.2). Due to the ill-posed inverse problem of reconstructing the SoS from echo phase shift, small differences in echo phase shift can in principle be reflected in more notable differences in the SoS images. In spite of that, the spatial distribution of SoS in and around the lumen-mimicking inclusion was similar between the two approaches. The small SoS offset of -8 m/s of the full-Rx compared to the Tx approach can be attributed to remaining experimental differences, e.g. due to the different way how the transducer's piezoelectric elements couple to the acoustic lens on reception than on transmission.

To avoid echo decorrelation due to blood flow, an in-vivo scenario requires a short acquisition time and thus a low number of Tx angles. A low number of Tx angles, however, increases tissue clutter which obscures blood echoes. The second part of the study (see Fig. 4.3) demonstrates that a reduction of acquisition time is possible with simultaneously reduced clutter if using the fast-Rx subtraction approach: Echo phase tracking inside the lumen becomes possible using only 5 Tx angles. The combination of this data with full-Rx data from outside the lumen results in a correct SoS image, in the sense that it agrees with the one obtained with full-Rx CUTE alone.

A clinical situation, however, differs from the presented phantom study in several aspects, which require attention when aiming at an in-vivo implementation of the proposed technique:

1. In the phantom, the simulated flow speed was identical across the lumen cross-section. In an in-vivo scenario, blood in the center of the lumen moves faster than blood near the periphery. So, a simple subtraction would lead to non-uniform echo strength, converging to zero towards the vessel wall. The subtraction corresponds to a linear ramp filter in the frequency domain of the 'slow' time axis (repetitions of acquisitions). To achieve a more uniform echo level, one may make use of wall filters, similar to what is used in Doppler flow imaging.
2. In an in-vivo scenario, the background tissue is not perfectly stationary due to pulsating blood flow, which will lead to residual 'stationary' clutter inside the vessel lumen even after subtraction. One strategy to minimize motion is by choosing an optimum timing of the fast-Rx acquisitions in-between successive heart beats. This can be achieved by synchronizing the acquisition with a motion detection algorithm or an ECG. A different and complementary strategy is motion tracking and motion compensation before subtraction or wall

filtering.

3. The low SNR of blood echoes can produce phase noise and thus artefacts in the SoS reconstruction. SNR can be improved by repeating the fast-Rx acquisition multiple times similar to what is done in Doppler flow imaging, and averaging the phase correlation maps before determining the echo phase shift.
4. In our present study, lumen motion occurred only in-between repetitions, but not during a single acquisition sequence. In an in-vivo situation, blood flow occurs during the few plane wave transmissions of each single fast-Rx acquisition sequence. Even though the number of Tx angles is short enough so that echo decorrelation does not occur, the blood motion will add a phase shift bias. One strategy to reduce this influence is to invert the Tx angle sequence in successive fast-Rx acquisitions, so that the phase shift due to blood flow cancels out in the final average phase shift.

In summary, the developed technique is a key step towards imaging the SoS inside arteries, in spite of blood flow and tissue clutter that obscures the hypoechoic blood echoes. This becomes possible via shortening the length of the acquisition sequence and via reducing stationary clutter using the subtraction approach. Whereas the envisaged goal of this study was to enable imaging the SoS inside the carotid artery, the developed technique may have further importance, e.g. for the assessment of iliac artery stenosis, or in liver imaging for reducing SoS artefacts that occur around the hepatic veins, vena cava, portal vein and the hepatic artery.

Funding

This research has received funding in part from the Swiss National Science Foundation (No. 205320_179038/1), from the European Union's Horizon 2020 research and innovation programme under grant agreement No 731771, Photonics Private Public Partnership, and is supported by the Swiss State Secretariat for Education, Research and Innovation (SERI) under contract number 16.0160.

Acknowledgements

The authors like to thank Prof. Matthew O'Donnel (University of Washington, USA) for fruitful discussions.

References

- [1] K. Kato, H. Sugimoto, N. Kanazumi, S. Nomoto, S. Takeda, and A. Nakao, “Intra-operative application of real-time tissue elastography for the diagnosis of liver tumours,” *Liver International*, vol. 28, no. 9, pp. 1264–1271, 2008.
- [2] J. Bercoff, M. Tanter, and M. Fink, “Supersonic shear imaging: a new technique for soft tissue elasticity mapping,” *IEEE transactions on ultrasonics, ferroelectrics, and frequency control*, vol. 51, no. 4, pp. 396–409, 2004.
- [3] T. J. Hall, Y. Zhu, and C. S. Spalding, “In vivo real-time freehand palpation imaging,” *Ultrasound in medicine & biology*, vol. 29, no. 3, pp. 427–435, 2003.
- [4] T. Shiina, N. Nitta, E. Ueno, and J. C. Bamber, “Real time tissue elasticity imaging using the combined autocorrelation method,” *Journal of Medical Ultrasonics*, vol. 29, no. 3, pp. 119–128, 2002.
- [5] J. Laufer, D. Delpy, C. Elwell, and P. Beard, “Quantitative spatially resolved measurement of tissue chromophore concentrations using photoacoustic spectroscopy: application to the measurement of blood oxygenation and haemoglobin concentration,” *Physics in Medicine & Biology*, vol. 52, no. 1, p. 141, 2006.
- [6] K. G. Held, M. Jaeger, J. Rička, M. Frenz, and H. G. Akarçay, “Multiple irradiation sensing of the optical effective attenuation coefficient for spectral correction in handheld oa imaging,” *Photoacoustics*, vol. 4, no. 2, pp. 70–80, 2016.
- [7] B. T. Cox, J. G. Laufer, P. C. Beard, and S. R. Arridge, “Quantitative spectroscopic photoacoustic imaging: a review,” *Journal of biomedical optics*, vol. 17, no. 6, p. 061202, 2012.
- [8] K. Jansen, G. van Soest, and A. F. van der Steen, “Intravascular photoacoustic imaging: a new tool for vulnerable plaque identification,” *Ultrasound in medicine & biology*, vol. 40, no. 6, pp. 1037–1048, 2014.
- [9] M. Wu, K. Jansen, A. F. van der Steen, and G. van Soest, “Specific imaging of atherosclerotic plaque lipids with two-wavelength intravascular photoacoustics,” *Biomedical optics express*, vol. 6, no. 9, pp. 3276–3286, 2015.
- [10] J. Weber, P. C. Beard, and S. E. Bohndiek, “Contrast agents for molecular photoacoustic imaging,” *Nature methods*, vol. 13, no. 8, pp. 639–650, 2016.
- [11] J. J. Niederhauser, M. Jaeger, R. Lemor, P. Weber, and M. Frenz, “Combined ultrasound and optoacoustic system for real-time high-contrast vascular imag-

- ing in vivo,” *IEEE transactions on medical imaging*, vol. 24, no. 4, pp. 436–440, 2005.
- [12] K. Daoudi, P. Van Den Berg, O. Rabot, A. Kohl, S. Tisserand, P. Brands, and W. Steenbergen, “Handheld probe integrating laser diode and ultrasound transducer array for ultrasound/photoacoustic dual modality imaging,” *Optics express*, vol. 22, no. 21, pp. 26365–26374, 2014.
- [13] M. K. A. Singh, W. Steenbergen, and S. Manohar, “Handheld probe-based dual mode ultrasound/photoacoustics for biomedical imaging,” in *Frontiers in Biophotonics for Translational Medicine*, pp. 209–247, Springer, 2016.
- [14] J. G. Laufer, E. Z. Zhang, B. E. Treeby, B. T. Cox, P. C. Beard, P. Johnson, and B. Pedley, “In vivo preclinical photoacoustic imaging of tumor vasculature development and therapy,” *Journal of biomedical optics*, vol. 17, no. 5, p. 056016, 2012.
- [15] M. Toi, Y. Asao, Y. Matsumoto, H. Sekiguchi, A. Yoshikawa, M. Takada, M. Kataoka, T. Endo, N. Kawaguchi-Sakita, M. Kawashima, *et al.*, “Visualization of tumor-related blood vessels in human breast by photoacoustic imaging system with a hemispherical detector array,” *Scientific reports*, vol. 7, p. 41970, 2017.
- [16] A. P. Sarvazyan, M. W. Urban, and J. F. Greenleaf, “Acoustic waves in medical imaging and diagnostics,” *Ultrasound in medicine & biology*, vol. 39, no. 7, pp. 1133–1146, 2013.
- [17] J. Bamber, C. Hill, and J. King, “Acoustic properties of normal and cancerous human liver—ii dependence on tissue structure,” *Ultrasound in medicine & biology*, vol. 7, no. 2, pp. 135–144, 1981.
- [18] J. F. Greenleaf and R. C. Bahn, “Clinical imaging with transmissive ultrasonic computerized tomography,” *IEEE Transactions on Biomedical Engineering*, no. 2, pp. 177–185, 1981.
- [19] P. L. Carson, C. R. Meyer, A. L. Scherzinger, and T. V. Oughton, “Breast imaging in coronal planes with simultaneous pulse echo and transmission ultrasound,” *Science*, vol. 214, no. 4525, pp. 1141–1143, 1981.
- [20] A. L. Scherzinger, R. A. Belgam, P. L. Carson, C. R. Meyer, J. V. Sutherland, F. L. Bookstein, and T. M. Silver, “Assessment of ultrasonic computed tomography in symptomatic breast patients by discriminant analysis,” *Ultrasound in medicine & biology*, vol. 15, no. 1, pp. 21–28, 1989.

- [21] N. Duric, P. Littrup, L. Poulou, A. Babkin, R. Pevzner, E. Holsapple, O. Rama, and C. Glide, “Detection of breast cancer with ultrasound tomography: First results with the computed ultrasound risk evaluation (cure) prototype,” *Medical physics*, vol. 34, no. 2, pp. 773–785, 2007.
- [22] J. Wiskin, D. Borup, S. Johnson, and M. Berggren, “Non-linear inverse scattering: High resolution quantitative breast tissue tomography,” *The Journal of the Acoustical Society of America*, vol. 131, no. 5, pp. 3802–3813, 2012.
- [23] J. Nebeker and T. R. Nelson, “Imaging of sound speed using reflection ultrasound tomography,” *Journal of Ultrasound in Medicine*, vol. 31, no. 9, pp. 1389–1404, 2012.
- [24] N. Ruiter, M. Zapf, R. Dapp, T. Hopp, W. Kaiser, and H. Gemmeke, “First results of a clinical study with 3d ultrasound computer tomography,” in *2013 IEEE International Ultrasonics Symposium (IUS)*, pp. 651–654, IEEE, 2013.
- [25] G. Zografos, P. Liakou, D. Koulocheri, I. Liovarou, M. Sofras, S. Hadjiagapis, M. Orme, and V. Marmarelis, “Differentiation of birads-4 small breast lesions via multimodal ultrasound tomography,” *European radiology*, vol. 25, no. 2, pp. 410–418, 2015.
- [26] D. Robinson, J. Ophir, L. Wilson, and C. Chen, “Pulse-echo ultrasound speed measurements: progress and prospects,” *Ultrasound in medicine & biology*, vol. 17, no. 6, pp. 633–646, 1991.
- [27] H.-C. Shin, R. Prager, H. Gomersall, N. Kingsbury, G. Treece, and A. Gee, “Estimation of average speed of sound using deconvolution of medical ultrasound data,” *Ultrasound in medicine & biology*, vol. 36, no. 4, pp. 623–636, 2010.
- [28] M. E. Anderson and G. E. Trahey, “The direct estimation of sound speed using pulse-echo ultrasound,” *The Journal of the Acoustical Society of America*, vol. 104, no. 5, pp. 3099–3106, 1998.
- [29] M. Jaeger, G. Held, S. Peeters, S. Preisser, M. Grünig, and M. Frenz, “Computed ultrasound tomography in echo mode for imaging speed of sound using pulse-echo sonography: proof of principle,” *Ultrasound in medicine & biology*, vol. 41, no. 1, pp. 235–250, 2015.
- [30] M. Jaeger, E. Robinson, H. G. Akarçay, and M. Frenz, “Full correction for spatially distributed speed-of-sound in echo ultrasound based on measuring aberration delays via transmit beam steering,” *Physics in medicine & biology*, vol. 60, no. 11, p. 4497, 2015.

- [31] M. Jaeger and M. Frenz, “Quantitative imaging of speed of sound in echo ultrasonography,” in *Proceedings of the IEEE International Ultrasound Symposium*, 2015.
- [32] D. V. Lukanova, N. K. Nikolov, K. Z. Genova, M. D. Stankev, and E. V. Georgieva, “The accuracy of noninvasive imaging techniques in diagnosis of carotid plaque morphology,” *Open access Macedonian journal of medical sciences*, vol. 3, no. 2, p. 224, 2015.
- [33] T. H. Park, “Evaluation of carotid plaque using ultrasound imaging,” *Journal of cardiovascular ultrasound*, vol. 24, no. 2, pp. 91–95, 2016.
- [34] S. Störk, R. A. Feelders, A. W. van den Beld, E. W. Steyerberg, H. F. Savelkoul, S. W. Lamberts, D. E. Grobbee, and M. L. Bots, “Prediction of mortality risk in the elderly,” *The American journal of medicine*, vol. 119, no. 6, pp. 519–525, 2006.
- [35] D. C. Steinl and B. A. Kaufmann, “Ultrasound imaging for risk assessment in atherosclerosis,” *International journal of molecular sciences*, vol. 16, no. 5, pp. 9749–9769, 2015.
- [36] G. Schulte-Altdorneburg, D. Droste, N. Haas, V. Kemeny, D. Nabavi, L. Füzesi, and E. Ringelstein, “Preoperative b-mode ultrasound plaque appearance compared with carotid endarterectomy specimen histology,” *Acta neurologica scandinavica*, vol. 101, no. 3, pp. 188–194, 2000.
- [37] M. Reiter, R. Horvat, S. Puchner, W. Rinner, P. Polterauer, J. Lammer, E. Minnar, and R. Bucek, “Plaque imaging of the internal carotid artery—correlation of b-flow imaging with histopathology,” *American journal of neuroradiology*, vol. 28, no. 1, pp. 122–126, 2007.
- [38] M. Tanter and M. Fink, “Ultrafast imaging in biomedical ultrasound,” *IEEE transactions on ultrasonics, ferroelectrics, and frequency control*, vol. 61, no. 1, pp. 102–119, 2014.
- [39] T. Loupas, J. Powers, and R. W. Gill, “An axial velocity estimator for ultrasound blood flow imaging, based on a full evaluation of the doppler equation by means of a two-dimensional autocorrelation approach,” *IEEE transactions on ultrasonics, ferroelectrics, and frequency control*, vol. 42, no. 4, pp. 672–688, 1995.

Chapter 5

Conclusion and Outlook

The goal of this doctoral dissertation was the continuation of the development of CUTE, a technique that allows to image the SoS based on pulse-echo US. It has been demonstrated in a proof-of-principle study, that CUTE is able to reconstruct the SoS with a very promising contrast and spatial resolution. The possibility to differentiate between different tissue types with CUTE has been proven in an preliminary volunteer study. At the beginning of the work for this doctoral dissertation, CUTE was, however, still suffering from major problems, namely the dependence of the SoS reconstruction on the geometrical situation of the sample under investigation and the *a priori* SoS \hat{c} on the reconstructed SoS. Further, in-vivo, the measurement noise that is typically observed prevented robust and reproducible SoS images.

The work presented in this thesis have solved this problems by the following findings:

- The forward model that relates the phase shift to the SoS must contain two essential features that are a necessary prerequisite for accurate SoS images:
 - The phase shift depends on both, the transmit and receive angle. This was taken into account by simultaneously steering both, the Tx and Rx angle (CMA approach)
 - The deviation between the *a priori* SoS \hat{c} that is used for beamforming and the true SoS c leads to an offset of the reconstructed position of the echoes. This results in an additional phase shift that has to be taken into account in the forward model.
- Due to the ill-posed nature of the forward model, measurement noise can lead to large errors in the reconstructed SoS. By formulating the forward model in a Bayesian framework, a statistical *a priori* model of the distribution of SoS can be included in the inversion calculation. This results in reproducible in-vivo SoS images.

- The SoS inside large blood vessels can be imaged by modifying the CUTE methodology in the following way:
 - Increasing the acquisition speed by introducing a receive beam-steering approach.
 - Highlight the blood echoes by a pairwise subtraction of data obtained from repetitions of the scan sequence.

As mentioned in the Introduction, SoS imaging has the potential to improve the diagnosis of various disease types. The advances of CUTE made during the work of this doctoral dissertation have lead to quantitative and robust in-vivo SoS images. This paved the way for clinical pilot studies to investigate the diagnostic applicability of CUTE, for example for the detection of breast cancer or the diagnosis of fatty liver disease. First, but jet unpublished results of a volunteer study (see Fig. 5.1) using a state-of-the-art clinical US system show that CUTE is able to distinguish the liver’s SoS between different volunteers, a prerequisite for the diagnosis of fatty liver disease. This further promises that CUTE is ready to be tested in patients.

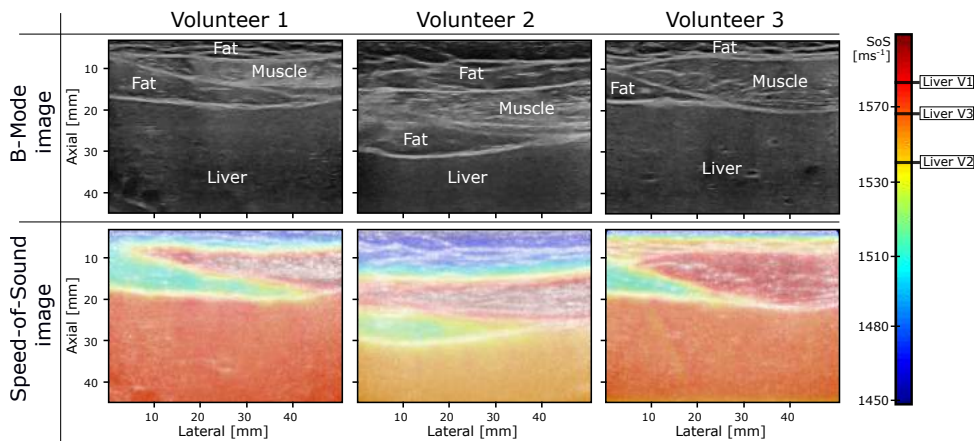


Figure 5.1: Examination of the liver through the abdominal wall of three volunteers. The B-Mode images allow the differentiation between the different tissue compartments within the abdominal cavity. In these images, hardly any difference can be seen in the appearance of the liver between different volunteers. On the contrary, the SoS images allow a clear differentiation between the three livers.

Accurately knowing the local distribution of SoS is, however, not only useful for the direct diagnosis of diseases. It is further also essential for a high contrast and resolution in conventional B-mode US. Typically, an average SoS is assumed for the B-Mode image reconstruction. When the actual SoS differs substantially from the assumed value, this results in defocused images, which in turn leads to a decreased sensitivity in e.g. the detection of small tumors in the breast [1]. Accordingly, various techniques were investigated for aberration correction based on a known SoS distribution [2–4].

Up to this point, CUTE is still limited by the straight-ray approximation of US propagation, neglecting diffraction and refraction. Diffraction will play only a minor role given the lateral resolution of the final SoS image (few mm) limited by regularization, in relation to the wavelength of the US pulse (0.3 mm at 5 MHz). Refraction, on the other hand, can have an important influence given the SoS contrast that one would expect in-vivo (up to $\approx 150 \text{ ms}^{-1}$). This influence, however, strongly depends on the geometry of the samples. Although we have shown in [5] that correct quantitative results were obtained in layered phantoms with small lateral SoS variations and SoS contrasts up to 135 ms^{-1} , refraction can have a major influence when imaging samples with strong lateral SoS variations, such as cylindrical inclusions. Indeed, phantom experiments have already shown that for inclusions with a SoS contrast $> 30 \text{ ms}^{-1}$, an increasing level of artifacts below the inclusion and an underestimation of the SoS inside the inclusion is observed. We envisage that refraction can be compensated by employing a more accurate forward model of sound propagation.

References

- [1] V. P. Jackson, “The role of us in breast imaging,” *Radiology*, vol. 177, no. 2, pp. 305–311, 1990.
- [2] M. Jaeger, E. Robinson, H. G. Akarçay, and M. Frenz, “Full correction for spatially distributed speed-of-sound in echo ultrasound based on measuring aberration delays via transmit beam steering,” *Physics in medicine & biology*, vol. 60, no. 11, p. 4497, 2015.
- [3] R. Ali and J. J. Dahl, “Distributed phase aberration correction techniques based on local sound speed estimates,” in *2018 IEEE International Ultrasonics Symposium (IUS)*, pp. 1–4, IEEE, 2018.
- [4] R. Rau, D. Schweizer, V. Vishnevskiy, and O. Goksel, “Ultrasound aberration correction based on local speed-of-sound map estimation,” in *2019 IEEE International Ultrasonics Symposium (IUS)*, pp. 2003–2006, IEEE, 2019.
- [5] P. Stähli, M. Kuriakose, M. Frenz, and M. Jaeger, “Improved forward model for quantitative pulse-echo speed-of-sound imaging,” *Ultrasonics*, p. 106168, 2020.

Author Contribution Statements

- **Forward Model for Quantitative Pulse-Echo Speed-of-Sound Imaging**

M.J. conceived of the presented idea and developed the theoretical formalism. M.J. and **P.S.** software implementation. **P.S.** designing and performing the experiments. **P.S.**, M.J. and M.F. interpretation of the results. **P.S.** draft preparation and visualizations. **P.S.**, M.J., M.K. and M.F. review and editing.

- **Bayesian Approach for a Robust Speed-of-Sound Reconstruction Using Pulse-Echo Ultrasound**

P.S. and M.J. conceived of the presented idea and developed the theoretical formalism. **P.S.** software implementation. **P.S.** designing and performing the simulations and experiments. **P.S.**, M.J. and M.F. interpretation of the results. **P.S.** draft preparation and visualizations. **P.S.**, M.J., and M.F. review and editing.

- **Receive Beam-Steering and Clutter Reduction for Imaging the Speed-of-Sound Inside the Carotid Artery**

M.J. conceived of the presented idea and developed the theoretical formalism. M.K., **P.S.** and J.-W.M. developed the methodology, M.J. and M.K. software implementation. M.K., **P.S.** and J.-W.M. designing and performing the experiments. M.K., **P.S.**, J.-W.M. and M.J. interpretation of the results. M.K. draft preparation and visualizations. M.J., M.F., **P.S.** and J.-W.M. review and editing.

P.S. - Patrick Stähli, M.J. - Michael Jaeger, M.F. - Martin Frenz, M.K. - Maju Kuriakose, J.-W.M - Jan-Willem Muller

Acknowledgements

First of all, I would like to thank Prof. Dr. Martin Frenz for the support I received during my years at the Biomedical Photonics Group and for giving me the opportunity to do this thesis. I could benefit a lot from your experience in the field of Biomedical Photonics.

I would like to express my sincere thanks to PD Dr. Michael Jaeger for all the support through the whole project. It was an honour for me to work with one of the most respected and experienced researchers in the field of pulse-echo SoS imaging. I enjoyed every scientific and non-scientific conversation, whether in the office or over a beer.

Further, I would like to thank all the group members of the Institute of Biomedical Photonics for the valuable scientific discussions we had as well as for the enjoyable non-scientific activities.

Finally, I thank those closest to me: Elsbeth & Peter, Michael & Roman for their endless support and encouragement in all my endeavours. Martina, I would like to express my deepest and most heartfelt appreciation. I am eternally grateful for your unconditional love, understanding, support and patience. You mean the world to me!

Erklärung

gemäss Art. 18 PromR Phil.-nat. 2019

Name/Vorname: Stähli Patrick

Matrikelnummer: 12-107-231

Studiengang: Physik

Bachelor Master Dissertation

Titel der Arbeit: Towards clinical speed-of-sound imaging based on pulse-echo ultrasound

LeiterIn der Arbeit: Prof. Dr. Martin Frenz
PD. Dr. Michael Jaeger

Ich erkläre hiermit, dass ich diese Arbeit selbständig verfasst und keine anderen als die angegebenen Quellen benutzt habe. Alle Stellen, die wörtlich oder sinn-gemäss aus Quellen entnommen wurden, habe ich als solche gekennzeichnet. Mir ist bekannt, dass andern-falls der Senat gemäss Artikel 36 Absatz 1 Buchstabe r des Gesetzes über die Universität vom 5. September 1996 und Artikel 69 des Universitätssta-tuts vom 7. Juni 2011 zum Entzug des Dokortitels be-rechtigt ist.

Für die Zwecke der Begutachtung und der Überprüfung der Einhaltung der Selbständigkeitserklärung bzw. der Reglemente betreffend Plagiate erteile ich der Univer-sität Bern das Recht, die dazu erforderlichen Perso-nendaten zu bearbeiten und Nutzungshandlungen vor-zunehmen, insbesondere die Doktorarbeit zu vervielfäl-tigen und dauerhaft in einer Datenbank zu speichern sowie diese zur Überprüfung von Arbeiten Dritter zu verwenden oder hierzu zur Verfügung zu stellen.

Bern, 15.6.2020

Ort/Datum

Unterschrift





Patrick Stähli

✉ Stermelstrasse 4B
6252 Dagmersellen

@ patrick.staehli@flydesign.ch

i Swiss citizenship

in www.linkedin.com/in/pstaehli

Education

- 08-2020- **PhD in Physics, University of Bern**
- 05-2017 Towards clinical speed-of-sound imaging based on pulse-echo ultrasound.
- 03-2017- **MSc in Physics, University of Bern**
- 09-2015 Determining the refractive index of highly scattering media by means of imaging with an ellipsometric setup. Awarded with the faculty price 2017 for the best master thesis in physics.
- 07-2016- **BSc in Physics with special qualification in Astronomy, University of Bern**
- 09-2012 **Minor in mathematics, University of Bern**
- 08-2012- **Federal vocational baccalaureate & additional qualifying examination**
- 08-2009
- 07-2007- **Apprenticeship as electrician**
- 07-2003

Professional Experience

- Gersag Krantechnik AG**
- Since 09-2012 ● PLC Software Engineer (15%)
- 08-2012 – ● Team leader of the electric department (30%)
- 08-2011
- 07-2011 – ● Electrician
- 09-2008
- Elektro Nottwil AG**
- 07-2008 – ● Apprenticeship & working as electrician
- 07-2003

Publications

Articles in Journals

P.Stähli, M. Kuriakose, M. Frenz and M. Jaeger, Improved Forward Model for Quantitative Pulse-Echo Speed-of-Sound Imaging, (Ultrasonics)

P.Stähli, M. Frenz and M. Jaeger, Bayesian Approach for a Robust Speed-of-Sound Reconstruction Using Pulse-Echo Ultrasound, (Submitted to IEEE Transaction on Medical Imaging in March 2020)

P.Stähli, J. Rička, M. Frenz, H. G. Akarçay, Mode filtering for extinction measurements on strongly scattering systems (Submitted to the Journal of the Optical Society of America A in October 2019)

M. Kuriakose, J. Muller, P. Stähli, M. Frenz and M. Jaeger, Receive Beam-Steering and Clutter Reduction for Imaging the Speed-of-Sound Inside the Carotid Artery, (Journal of Imaging, 2018)

Articles in Conference Proceedings

P. Stähli, M. Frenz and M. Jaeger, Reflection-Mode Speed-of-Sound Imaging Using Soft-Prior Limits (IEEE International Ultrasonics Symposium, 2019)

M. Jaeger, T. Schweizer, C. Etter, P. Stähli, M. Frenz, Diffraction-limited spatial resolution using synthetic focus time-of-flight ultrasound tomography, (IEEE International Ultrasonics Symposium, 2019)

Talks

P. Stähli, M. Frenz and M. Jaeger, Reflection-Mode Speed-of-Sound Imaging Using Soft-Prior Limits, (IEEE International Ultrasonics Symposium, 2019)

P. Stähli, M. Frenz and M. Jaeger, Soft-prior regularization for improved speed-of-sound imaging in CUTE, (International Congress on Ultrasonics, 2019)

Posters

M. Jaeger, T. Schweizer, C. Etter, P. Stähli, M. Frenz, Diffraction-limited spatial resolution using synthetic focus time-of-flight ultrasound tomography, (IEEE International Ultrasonics Symposium 2019)

M. Kuriakose, J. Muller, P. Stähli, M. Frenz and M. Jaeger, Receive angle steering and clutter reduction for imaging the speed-of-sound inside large blood vessels, (BMPN annual meeting, 2018)

M. Kuriakose, J. Muller, P. Stähli, M. Frenz and M. Jaeger, Receive beam steering for dynamic image reconstruction of speed of sound in biological organs using computed ultrasound tomography in echo mode, (IEEE International Ultrasonics Symposium, 2018)